Design, Construction and Characterisation of a Variable Balance Magnetron Sputtering System

Author : Colm O'Leary B.Sc.

Department of Electronic Engineering,
Dublin City University,
Glasnevin,
Dublin.

Supervisor: Dr. David Cameron

Date : September 1999

Submitted for the award of Master of Engineering

Declaration

I declare that the contents of this thesis, where not referenced, is based upon my own research.

Colm O'Leary

Acknowledgements

To the following people, I am eternally grateful.

To Dr. David Cameron for his advice, enthusiasm and patience.

To my sister Anne, who's never ending determination and encouragement has been an inspiration to me for so long.

To my dear friend Louise. Thanks for putting up with the bad moods. I owe you again.

To Annette Pigott, for the under-estimated peace of mind she provided while I completed my work.

Many thanks to the following people for their technical assistance.

To Jim and Martin in the workshop, for design and manufacturing information they helped with.

To Dr. Partick McNally, who's door has been always open.

Abstract

In many plasma deposition systems it is necessary to monitor and control the flux of species bombarding the substrate in order to control film growth kinetics. The ability of controlling this growth can lead to desirable changes in the films structure and properties. Presented in the following thesis is a report on the design and construction of a variable balance magnetron sputtering system with an energy resolved mass spectrometer. Also reported is the characterisation of the deposition process at various degrees of magnetron unbalance. This unbalance is controlled by varying the current I in a solenoid, which is the central pole of a cylindrical magnetron, place behind the sputtering target. The current I is found to ultimately control the deposition conditions at constant pressures and levels of discharge current. It is also found to directly control the energy and flux of species bombarding the substrate during deposition. This data and the effects on the film properties are reported on.

Table of Contents

Chapter One Introduction 1

1.1 Introduction 1
1.2 Project Outline 2
1.3 Chapter Review 3

Chapter Two Plasma Theory 5

2.1 Introduction 5
2.2 Definition of a Plasma 5
2.3 Formation of a Plasma 6
2.4 Plasma Fundamentals 7
2.4.1 Plasma collisions & current density 9
2.5 Glow Discharge Plasma's 12
2.5.1 The Cathode & Dark space events 15
2.5.2 The Anode 16
2.6 Charged particles subjected to magnetic fields 17

Chapter Three Thin Films 20

3.1 Introduction 20
3.2 Thin Film Applications 20
3.2.1 Semi-Conductors 20
3.2.2 Hard and Protective Coatings 27
3.3 Thin Film Processes 34
3.3.1 Glow Discharge Process Technology 35
3.3.1.1 Plasma Processing 35
3.3.1.2 Sputter Process Fundamentals 40
3.3.1.3 D.C. Diode Sputtering 45
3.3.1.4 R.F. Sputtering 46
3.3.1.5 Bias Sputtering 48
3.3.1.6 Reactive Sputter Deposition 48

3.3.1.7 Ion Beam Sputtering 50
3.3.1.8 Microwave ECR Sputtering 51
3.4 Thin Film Growth 52
3.4.1 Film Bombardment 55
3.4.1.1 Ion and Electron Bombardment 55
3.4.1.2 Neutral bombardment 58
3.5 Thin Film Properties 59
3.5.1 Film Microstructure 59
3.5.2 Adhesion 61
3.5.3 Stress 62

Chapter Four Magnetron Sputter Technology 67

4.1 Introduction & Applications 67
4.2 Magnetron Sputtering Principles 67
4.3 Planar Magnetron Sputtering 71
4.3.1 D.C. Planar Magnetron Sputtering 71
4.3.2 R.F. Magnetron Sputtering 74
4.4 Cylindrical Magnetron Sputtering 74
4.5 Unbalanced Magnetron Sputtering 77
4.6 The Sputter and S-Gun Magnetrons 81

Chapter Five Design and Operation of the Sputtering Chamber 83

5.1 Introduction 83
5.2 Sputtering Chambers 83
5.3 System design & Electronic Rack 83
5.4 Pumping & Vacuum systems 86
5.5 Gas flow, control and pressure measurement 86
5.6 Cathode considerations 87
5.6.1 Target Fabrication 88
5.6.2 Target Cooling 88
5.6.3 Cathode Insulation 89
5.6.4 Power Control 92
5.7 Anode Considerations 92
5.8 Magnetron Design and Construction 95
5.8.1 Solenoid Design 96

5.8.2 Solenoid Construction 98
5.9 Analyzer chamber 100
5.9.1 Energy Analyser 100
5.9.2 Mass Spectrometer 103
5.9.3 Pressure Control 103
5.9.3.1 Aperture Design 105
5.10 Electrical & Thermocouple Wiring 107

Chapter Six Magnetic Field Analysis 109

6.1 Introduction 109
6.2 Field Mapping Technique 109
6.3 Field Vectors 111
6.4 Magnetic Field Shapes 113
6.5 Field Analysis 118

Chapter Seven Results 121

7.1 Introduction 121
7.2 Target Characteristics 121
7.3 Deposition Characteristics 123
7.4 Adhesion 127
7.5 Microstructural Characteristics 128
7.6 Ion and Electron Bombardment 132
7.6.1 Introduction 132
7.6.2 Energy Analyser Set-up 132
7.6.3 Electron and Ion Currents 134
7.6.4 Ion Detection 136
7.6.5 Power Dissipation 141

Chapter Eight Discussion 149

8.1 Discussion of Results 149
8.2 Limitations 151
8.3 Future Research 152

Appendices

Appendix A	Cryogenic Pumps
Appendix B	Magnetron Driver
Appendix C	Baratron® Specifications
Appendix D	Excel Coefficient Finder
Appendix E	Vector Plot Software
Appendix F	Field Mapping Software
Appendix G	Neutral Particle Reflection Calculation
Appendix H	Ion and Electron Current & Power Data

Chapter One

Introduction

1.1 Introduction

Thin films are now widely used in everyday life. During the past 30 years, the science of thin film technology has grown into a multi-billion dollar industry. This growth has occurred due to fundamental understandings of the processes and tools used to deposit thin films, and due to the need for new products in the mechanical, electronics and optical industries. Somewhat ingenious techniques have been conceived, developed and refined to sophisticated levels in order to achieve this. Deposition conditions range from ultrahigh vacuum, where a film can be grown atom by atom so as to design and engineer new materials, to intermediate pressures where deposition rates of microns per second can be achieved, to plasmas which sputter or activate the material to be deposited.

General applications of these films are immense. Today, semiconductor chip sales are estimated at \$130 billion for 1999 with increases of over 10% per annum forecasted over the next three years[1]. Capitol equipment costs, the equipment used to manufacture these semiconductor chips, runs to \$20 billion per year.

Hard surface coatings, usually of carbides, silicides, nitrides and borides, are being increasingly used for the protection of metal surfaces and to increase the wear characteristics of machine parts and tools. The damage caused by wear failure and fatigue is estimated to be over \$100 billion dollars per annum in the U.S.A alone[2].

Magnetic films and optical coatings are used in everyday data storage in the areas of hard drives, magnetic tape heads and cd-roms. Optical coatings are applied for anti-reflection purposes, as interference filters on solar panels, as plate glass infrared solar reflectors, on filament lamps to increase the luminous flux intensity and for laser optics. Fiber optics, which have become increasingly important for the information age, use fabrication techniques which depend on thin films deposited on preforms from which the optical fibers are drawn.

Electronic displays use thin films in their fabrication with conductive, transparent, luminescent, fluorescent, dielectric and insulating layers in order to produce liquid-crystal displays, light emitting diodes, electroluminescent displays and plasma/fluorescent displays.

Deposition techniques, as will be seen, vary immensely due to the large amount of applications in which thin films have become, not only standard but, essential. The main categories of thin film deposition can be broken into the following process technologies:

1. Evaporative methods
2. Glow Discharge processes
3. Gas-phase chemical processes
4. Liquid-phase chemical techniques

The main consideration of this thesis will be the Glow Discharge Process, and in particular Magnetron Sputtering techniques will be examined in detail.

1.2 Project Outline

The overall objective of the project can be stated in two points.

1. The design and construction of a functional and robust variable balance magnetron sputtering system.
2. The collection and interpretation of process data, with respect to the process variables.

A sputtering system has been designed so that it can be used in many different modes of operation with ease. These modes include diode, reactive, bias and magnetron sputtering. In the author's application, a magnetron sputtering configuration has been used, where one of the key project goals is the collection of data on particle flux arriving at the substrate with respect to the degree of unbalance of the magnetron. This unbalance is controlled by varying the current, I_S, in an electromagnet, which is used as the central pole of a cylindrical magnetron, designed and built by the author. The outer pole is constructed with permanent ferrite magnets.

The ion flux bombarding the substrate is measured using a quadrupole mass spectrometer, which receives a sample from the plasma through an effusive source designed into the chamber wall. Using an energy analyzer designed and constructed by the author an energy spectrum of ion species may be recorded for analysis.

1.3 Chapter Review

Chapter two is designed to give the reader an introduction into how a plasma body is formed and sustained between two electrodes. It is also an introduction to the different species and interactions encountered in a plasma body and to what processes are seen at each electrode.

Chapter three is on Thin Films and is written so the reader is able to receive a firm knowledge of the main applications of thin films and methods of plasma deposition used in industry today. Also covered are the growth and formation of films, and the effects on film characteristics when they are grown under different conditions of pressure, temperature and particle bombardment.

Chapter four is on Magnetron Sputtering so that additional detail may be made available to the reader on the process carried out by the author's sputtering system.

Chapter five simply deals with the design and construction of the variable balance magnetron sputtering system built in house by the author.

Chapter six examines the magnetic field produced by the author's magnetron and shows how the magnetic field varies with solenoid current through the employment of a mapping system. The effects to the plasma and target caused by the field changes are also examined.

Chapter seven is a collection of results gathered by the author. Information on target characteristics, deposition rate, deposition temperature, ion and electron bombardment and film characteristics are presented, amongst others. These are examined in relation to the solenoid current which ultimately controls all the process and deposition parameters.

Chapter eight is a discussion of the results obtained. It also lists some limitations and has recommendations for future research with the author's variable balance magnetron sputtering system.

Chapter One References

[1] Reuters News, Global chip sales seen bouncing back in 1999, www.reuters.com. Dec (1998).

[2] V. Doane,'Abrasive wear - the alloy question!' Wear and Fracture Prevention, American Soc. for Metals (1981).

Chapter Two

Plasma Theory

2.1 Introduction

The following chapter will give the reader an insight into the formation of plasma. It will also give details of important plasma properties that help us to understand the fundamental operation and characteristics of plasma. While the descriptions are adequate enough to understand the principles of plasma, it should be noted that a plasma is a highly complex state of matter and an abundance of relevant information exists[3-5] explaining all the issues touched upon in greater dept.
In order to converge more with the main topic of this thesis, the author has reviewed both the reaction of plasma with surfaces and the response of particles due to the presence of applied magnetic fields. This will be useful as the reader reaches chapter four and beyond.

2.2 Definition of a Plasma

The term 'plasma' is applied to a gas in which all of, or a fraction of, the atoms have lost one or several of their electrons and are converted into ions. Plasma can be assumed to be mixture of three main components – free electrons, positive and negative ions and neutral atoms (or molecules). These liberated electrons which have acquired freedom of motion can transport electric current, or in other words a plasma is a conductive gas.

The state of any plasma can be characterized by the density of neutral atoms (n_a), the electron density (n_e), and the electron energy distribution which can be approximated by an average electron temperature (T_e). The kinetic temperature of ions/neutrals will be much less than that of the electron temperature because of the large mass difference. This mass difference allows electrons to experience a relatively large force, in comparison to ions, due to the presence of an external electric field ε.

$$\varepsilon e = m_i a = m_e a \qquad \text{Eqn 2.1}$$

where m is the mass of the particle, a the acceleration due to the electric field and e is the particle charge.

This in turn allows us to view electrons as moving rapidly against a stationary cold ion/atom background due to the large mass difference between the species.

The temperature unit used to describe plasma is the electron volt (eV). It should be noted that this is deceiving as 1eV equals 11,600^{0}C and a plasma is referred to as being 'cold' up into the region of a hundred thousand degrees, or a few electron volts. In hot plasma, the temperature is at least a few hundred electron volts i.e. millions of degrees. These temperatures refer to equivalent energies of particles and not to actual measurable temperature, as we know it.

2.3 Formation of Plasma

As stated above, stripping electrons from atoms in order to create ions is the basis of forming a plasma. This ionization effect can be carried out in many ways, the most important of which are

1. Ionization by heat
2. Ionization by radiation
3. Ionization by electrical discharge

All substances, if heated to sufficiently high temperatures, will become ionized. The process is termed 'thermal ionization'. The thermal requirement is that of the energy required to remove the most loosely bound electron in the outer shell, and is very dependent on the stability of that atom. Typical thermal requirements are in the order of several thousand degrees. Examples of such plasmas are stars.

Ionization by radiation is formed through the bombarding of a gas by a continuous source. Typical sources are ultraviolet, but this type of plasma tends to be very hard to control due to recombination effects. Such plasma exists in the outer atmosphere of the earth (ionosphere) and is formed and sustained by radiation bombardment from the sun.

The most widely used and commonly encountered plasma is created due to ionization by electrical discharge. These are seen naturally in the form of electric sparks and lightening, and in industry in the form of gas discharge devices. The production of this form of plasma is dependent on ionization through an electron avalanche process. For this, the applied electric field must be large enough so that the energy of an electron is more than the required amount to produce an ion-electron pair in its mean free path. These secondary electrons produced in collisions are then accelerated by the electric field and the avalanche begins. Primary ionization reactions are governed by

$$A + e_1^- \text{ (fast)} \longrightarrow A^+ + e_1^- \text{ (slowed)} + e_2^- \text{ (slow)}$$

Electron velocity is changed from v to $v\cos\Theta$ to satisfy the conservation of momentum.

The section on glow discharge plasma will cover this topic in more detail.

2.4 Plasma Fundamentals

The following two sections examine the characteristics of plasma species interacting with substrates and electrodes. It also looks at important screening effects of plasma charge build up.

2.4.1 Plasma Collisions and Current Density

Firstly, all collisions in plasma can be characterized as either elastic or inelastic. The most important interaction, ionization, occurs mainly due to the inelastic collision of electron-atom interactions. This interaction can be regarded as the transfer of energy from the electron to the atom and therefore can be converted to the internal energy (ionization or excitation energy) of the struck gas atom. This is governed[6] by

$$U_m = \left[\frac{M_A m_e}{M_A + m_e} \right] E_o \cos^2 \theta \qquad \text{Eqn 2.2}$$

where m_e and M_A are the masses of the electron and atom respectively, E_o the initial electron kinetic energy and θ the electrons angle of incidence.

Unless the value of U_m is sufficient enough to raise the energy level of the most loosely bound electron to an excited energy state then the collision will remain elastic due to the discrete nature of energy transfer between particles. If the excitation energy is reached then the atom will hold its outer electron in an excited vibrational state. This electron can relax to ground state through the emission of a photon. If the energy packet received is equivalent to the ionization energy then the atom can eject the most loosely bound electron into the plasma body. Common excitation and ionization energies are given in table 2.1 below.

Element	Excitation Energy (eV)	Ionization Energy (eV)
H	10.2	13.6
He	20.91	24.58
N	6.3	14.54
Al	3.13	5.98
Ar	11.5	15.76

Table 2.1 Excitation and Ionization energy levels for various elements

The energy transfer of an elastic collision between an electron and atoms is governed by the equation

$$E = E_o \left[\frac{m_e - M_A}{m_e + M_A} \right]^2 \cos^2 \theta \qquad \text{Eqn 2.3}$$

where E and E_0 are the kinetic energies of the electron after and before the collision respectively, m_e the electron mass and M_A the atomic mass.

Since the atomic mass is massive compared to the electron mass (app. 73,000 time greater for argon), the equation can be well approximated to

$$E \cong E_o \cos^2 \theta \qquad \text{Eqn 2.4}$$

In effect the only measurable change is to the electron direction.

Many other collision processes exist in plasma body such as ion-ion, ion-neutral, electron-electron, electron-ion and electron-neutral attachment. Some reaction mechanisms are given below.

(a)	$A^+ + A^+ \longrightarrow A + A^{++}$	Ion-Ion
(b)	$A^+ + B \longrightarrow B^+ + A$	Ion-Neutral
(c)	$A^+ + A \longrightarrow A_2^+$	Ion-Neutral
(d)	$e^- + e^- \longrightarrow e^- + e^-$	Electron-Electron
(e)	$e^- + A^+ \longrightarrow A^{++} + 2e^-$	Electron-Ion
(f)	$e^- + A \longrightarrow A^-$	Electron-Atom
(g)	$e^- + A^* \longrightarrow A + e^-$	Electron-Atom (excited)
(h)	$e^- + A \longrightarrow A^* + e^-$	Electron-Atom
(i)	$e^- + A \longrightarrow A^- + h\nu$	Electron-Atom
(j)	$h\nu + A^- \longrightarrow A + e^-$	Photon-Ion

The random motion in plasma of ions and electrons brings about an important topic on current density caused by the flow of these charged particles. We start with the number of electrons or ions that reach any surface can be measured in terms of the electron or ion current density. This can be expressed initially, from a derivation of pressure[6], by the number of particles striking unit area per second[6], or the flux per unit area as

$$s_e = \tfrac{1}{4} n_e \bar{v}_e \qquad s_i = \tfrac{1}{4} n_i \bar{v}_i \qquad \text{Eqn 2.5}$$

where $n_{i\,e}$ is the ion or electron density and $\overline{v}_{i\,e}$ the average velocity of the particles.

In a plasma body, the velocities of ions, atoms and electrons can be assumed to obey Maxwell-Boltzmann statistics, provided no magnetic fields are present, and so the average velocity of either can be expressed[7] as a function of temperature and mass

$$\overline{v} = 1.656x10^{-8}\left(\frac{T}{m}\right)^{1/2} \quad \text{(cm/sec)} \qquad \text{Eqn 2.6}$$

where T is the temperature of the particle, and m the mass.
Clearly, velocities well below and above $\overline{v}$ can also be expected due to the Maxwellian curve.

Then, expressing the impinging particle rate as a current density is

$$j_e = \frac{en_e\overline{v}_e}{4} \quad \text{for electrons and}$$

$$j_i = \frac{en_i\overline{v}_i}{4} \quad \text{for ions} \qquad \text{Eqn 2.7}$$

where e is the electron charge and j is in units of amps per unit area (current density). The value of e is of opposite sign for ion current.

Due to the large differences in the velocity between ions and the electrons, large differences between the current densities can be measured on surfaces immersed in a plasma. Electron current is usually a few thousand times that of ion current for a typical plasma.

2.4.2 Plasma Frequency, Floating Voltages and the Debye Length

The plasma frequency arises due to the conductive nature of plasma and its ability to exclude fields from itself. If a local concentration of electron charge momentarily builds up, then these individual charges will begin to repel each other due to coulomb repulsion. As an electron moves back towards its original position, its momentum, due to its kinetic energy, tends to make the electron overshoot its original position in a harmonic type oscillation. The electron oscillates back and fourth around relatively stationary ion charge with a frequency f_p.
For simplification one-dimensional estimations[7] are shown and the frequency is written as

$$\omega_p = \left(\frac{ne^2}{m_e \in_o}\right)^{1/2} = 2\pi f_p \qquad \text{Eqn 2.8}$$

So, substituting in, the frequency is

$$f_p = 8.98x10^3 n_e^{1/2}$$

Eqn 2.9

where n_e is the electron density and is measured in cm^{-3}.

Applications for this plasma frequency come about when determining the frequency of an applied electric field. If the field applied has a frequency less than ω_p then the plasma can react as a conductor due to the faster response of the plasma electrons. On the other hand if the field applied has a frequency higher than ω_p then the plasma can start to act as a dielectric due to the static nature imposed on the electrons. This is due to the field polarity changing faster than the electrons can change direction in an AC discharge.

When measuring current density with probes immersed in plasma or at the anode electrode, the probe charges negatively relative to the plasma due to the greater amount of electron flux over ion flux impinging upon probe. The plasma can be taken to be at a potential V_p relative to ground. The plasma potential, V_p, can be expressed[1] as

$$V_p = kT_i \ln \frac{2}{q_i} \qquad \text{Eqn 2.10}$$

where T_i and q_i are the temperature and charge of the ions.

The floating potential developed on a isolated surface, V_f, is written[7] as

$$V_p - V_f = \frac{kT_e\left(\ln\left(\frac{m_i}{2.3m_e}\right)\right)}{2e} \qquad \text{Eqn 2.11}$$

where V_p is the plasma volatge, T_e the electron temperature, m the particle mass and e the electron charge.

This negative voltage develops due to the higher strike rate per unit time for electrons over ions. The build up of negative charge continues until the charge on the surface is such that it will repel enough low energy electrons to bring to equilibrium the flux of ion and electron charge, or so that

$$eN_i = eN_e \qquad \text{per unit area} \qquad \text{Eqn 2.12}$$

Once the probe obtains this equilibrium at the floating potential a sheath develops adjacent to its surface. The properties of this sheath are similar to the sheath that develops at the cathode dark space, which is mainly a voltage drop, but with a magnitude of $V_p - V_f$.

The fraction of electrons (N'_e) that can penetrate this sheath voltage drop, and so the number of ions hitting the surface is given by the equation

$$N_i = N_e^{'} = N_e \exp\left(\frac{-eV}{kT_e}\right) \qquad \text{Eqn 2.13}$$

where N'_e is the number of electrons with energy greater than V(= V_p-V_f), the sheath voltage drop.

This tells us that the current density of ions and high energy electrons is balanced so that

$$j_e = \frac{en_e^{'}\bar{v}_e}{4} = \frac{en_i\bar{v}_i}{4} \qquad \text{Eqn 2.14}$$

Another important parameter, the Debye length, λ_D, is the ability of plasma to screen off any electric field that is imposed upon it. This screening effect occurs at any sheath region developed in the plasma, which is typically at the cathode, anode, a wall or a grounded probe immersed in the plasma. The screening length is related to the mean kinetic energy of the electrons.

Any small field applied in a plasma will then tend to fall off over this finite dimension known as the Debye length. The voltage distribution at a distance *x*, can be measured according to the formula

$$V(x) = V_o e^{\left(-x/\lambda_D\right)} \qquad \text{Eqn 2.15}$$

where V_o is a small potential at a point, *V(x)* the potential at a distance *x* from that point and λ_D the Debye length.

The Debye length is then, the length over which the potential at a point has fallen off to 0.37 of its initial value.

The Debye length is dependent on numerous parameters and is calculated from

$$\lambda_D = \left(\frac{kT_e \in_o}{n_e e^2}\right)^{1/2} \qquad \text{Eqn 2.16}$$

Substituting into equation 2.16 yields

$$\lambda_D = 6.9x\left(\frac{T_e}{n_e}\right)^{1/2} \qquad \text{Eqn 2.17}$$

This is assuming Maxwellian conditions for velocity of ions and electrons. Typical values range from 1 to 0.1 mm.

Plasma's can be seen then as equipotential regions, except for small potentials that fall off over a dimension of λ_D. The with of plasma sheaths, or regions where charge neutrality is broken and a net space charge exists, can be estimated from the Debye length in the form of

$$S = \lambda_D \left(\frac{eV}{kT_e} \right)^{3/4} \qquad \text{Eqn 2.18}$$

where V is the potential difference between the surface and the plasma. For glow discharges S is typically $5\lambda_D$.

2.5 Glow Discharge Plasma

A glow discharge plasma is a low temperature plasma. This form of plasma is overall said to be neutral, or that the number of electrons is equal to the number of ions in the discharge. Local imbalances may exist at walls but these are negligible.

A glow discharge is a self sustaining plasma, in that, the avalanche effect of electrons continues the production of the ion species. Figure 2.1 shows the avalanche condition from the initial applied voltage in a typical low pressure discharge. The establishment of a glow discharge is uncomplicated and is easily ignited between two electrodes. As can be seen from figure 2.1, the formation of a glow discharge can be broken down into different regions.

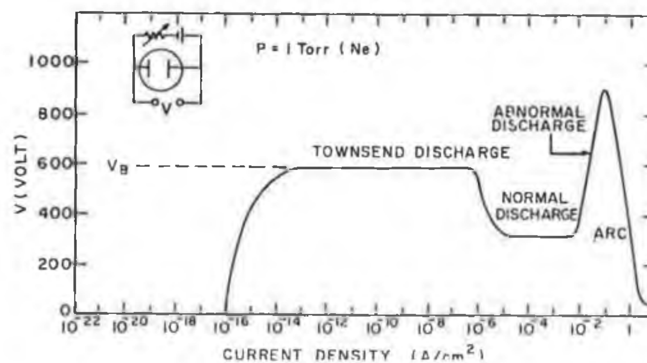

Figure 2.1[1] **The voltage and current characteristics at the formation of a dc glow discharge.**

With the application of the initial voltage little current flows through the system due to there being little ionization effects in the bulk gas. As the voltage is increases towards V_B, the breakdown voltage, more energy is given to the ions, which allows increased collisions with atoms and electrodes. This in turn creates more ions and electrons form the ionization and secondary electron emission effects. These effects allow the current to increase gradually until break down is reached, avalanche occurs and current increases drastically in the region of the Townsend discharge. The breakdown voltage is directly related to the gas pressure and the mean free path of secondary electrons. This relationship between gas pressure and spark voltage is called Paschen's law.

The voltage required to ignite the discharge is governed by the relationship

$$V_s = a\frac{pl}{\log pl + b} \qquad \text{Eqn 2.19}$$

where p is the gas pressure, l the electrode separation, a and b are constants for a particular gas.

The electron mean free path is then related to the pressure by

$$\lambda_o \cong lp_s \qquad \text{Eqn 2.20}$$

where λ_o is the mean free path of the electrons, and p_s the gas pressure.

The discharge is said to be self-sustaining when the number of electrons produced is just sufficient to produce the same number of ions to again generate the same number of electrons. These ions liberate electrons from the electrodes (secondary) and atom-ion, ion-ion collisions. When this condition is reached the voltage reduces and current increases. This is said to be a normal discharge. Due to recombination effects and excited atoms returning to ground state the plasma begins to glow.

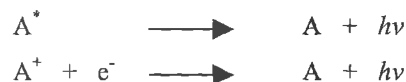

where A^* is an excited atom and e is a high energy electron

The glow exhibited in figure 2.2 below has a non-uniform appearance. As can be seen, the discharge between the two electrodes is broken into numerous columns. In the cathode dark space (or Crookes dark space) it can be seen that there is an abundance of positive charge or ions (d,g). This is due mainly to the negative voltage applied to the cathode, which has driven out the lighter, easily influenced electrons due to the field strength (c) at the electrode.

The result is the screening of the cathode by a cloud of positive ion species (d,g), which ensures that almost all of applied voltage falls off across this dark space. This means that only a small potential drop remains across the remainder of the tube (d).

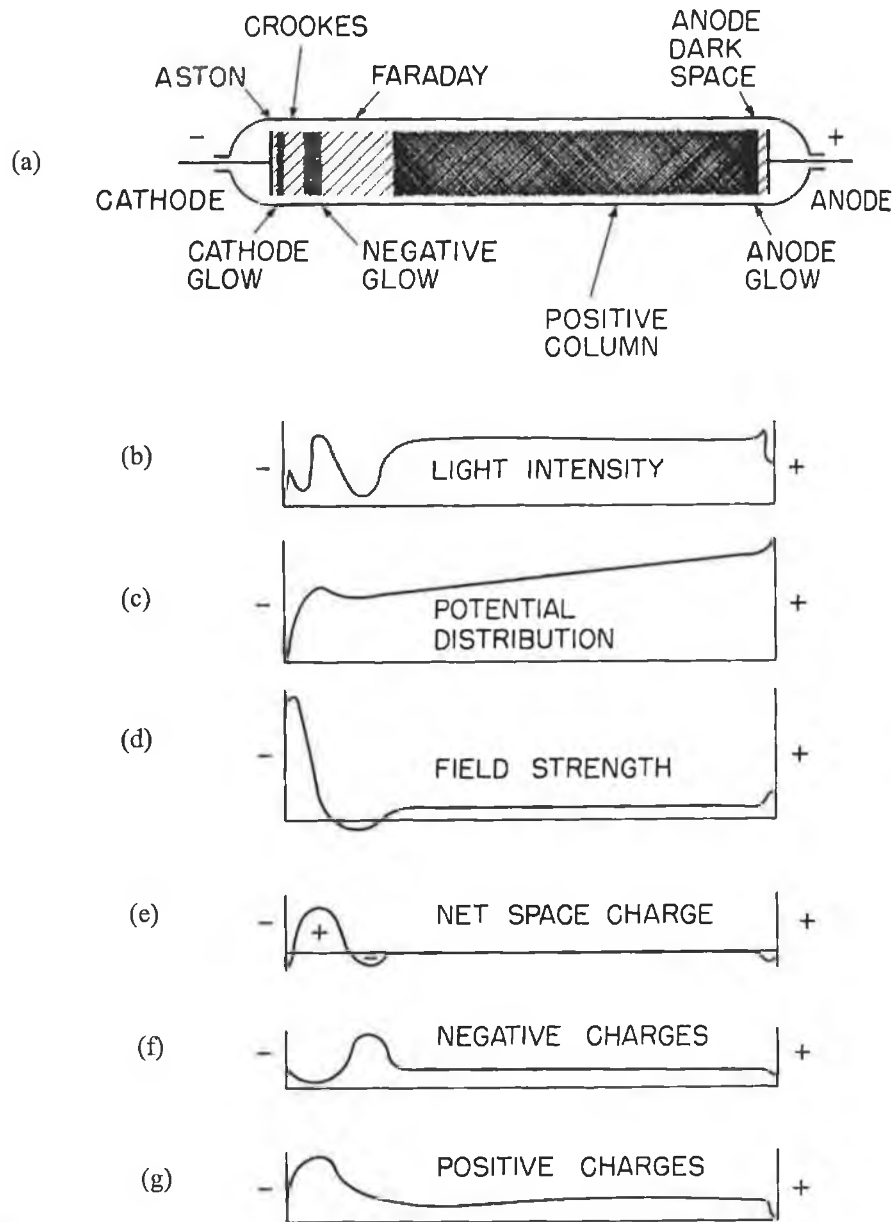

Figure 2.2[2] Representations of the (a) structure of a glow discharge in a dc diode system (b) light intensity, (c) potential distribution, (d) electric field strength, (e) net space charge, (f) negative charge distribution and (g) positive charge distribution.

This large voltage drop is the acceleration mechanism for the ions that enter the dark space by diffusion from the negative glow region. This is the basic process for sputtering and also ensures that the

glow is sustained by the production of secondary electrons emitted from the cathode. These accelerated ions are also neutralized at the cathode. These liberated electrons (typically 0.1 electron per ion) are quickly repelled by the electric field and maybe then involved in ionization processes with neutral gas atoms if their energies are sufficient to cause inelastic collisions. The combined results of these ionization effects are seen as the negative glow. The end of the negative glow corresponds to the range of electrons with sufficient energy to produce excitation, and in the Faraday dark space these electrons once more gain energy. The sustaining feature of the bombarding ion recombining with an electron at the cathode also ensures overall net zero charge as the liberated electron causes ion generation to balance. The cathode glow is the result of this recombination at the cathode surface (figure 2.2)

The positive column is the ionized region that extends from the Faraday dark space almost to the anode. It serves merely as a conduction path between the two and is known as the plasma, as the net charge in this column is near or at zero (e). Electrons that gain enough energy in the last few mean free paths to excite ions being accelerated from the anode form the anode glow region.

2.5.1 Cathode and Dark Space Events

The events that occur at the cathode are important for sputtering. Glow discharge chambers were the first sputtering devices used. The liberation process of cathode atoms from the surface is covered in detail in chapter three under thin film processes. It can be said here however that scattering effects at the cathode determine the cathode atom trajectory upon ejection and transition across the dark space. This is due to collisions with incoming sputter ions. In glow discharges however, the cathode acts primarily as an electron source for sustaining the discharge. Electrons are emitted from the target in mainly two processes, positive ion bombardment and due to photoelectric effects.

Characterized by the intense electric field, two main processes occur at the dark space. These are the acceleration of ions toward the cathode and the acceleration of the liberated electrons away from the cathode into the positive column and eventually onto the anode.

The number of electrons that eventually strike the anode is a direct result of the electron probability of inelastic collision. This probability of having an interaction, which results in ionization or excitation, is related to the initial electron energy. The electron kinetic energy is related to it temperature through the following relationship

$$mv^2 = 3kT \qquad \text{Eqn 2.21}$$

This relationship also determines the average kinetic energy of ions and atoms by using the appropriate mass. Since the ratio of electron to ion/atom mass is of the order of 1:73,000 it can be seen that a large variation in velocity and temperature exists between the species.

From this relationship it is noted that increases in temperature result in increases in average kinetic energy and so velocity. For fast moving electrons, probability of inelastic collisions decrease as the electron energy increases due to the speed of electrons as they pass by 'cold' or near stationary atoms. This is illustrated in figure 2.3 where the ionization probability, P_i, is plotted against electron energy in volts for argon gas. As can be seen there is a distinct energy when the probability is maximized. This energy does not correspond to the maximum velocity or temperature of the electrons. At this energy the electron velocity is such that the short range Coulomb force can attract the attention of the electron, so to speak, when in the vicinity of the atom. Also, from the figure it can be seen that the probability is zero for an ionization to occur for an electron with insufficient energy (below the ionization potential for Ar).

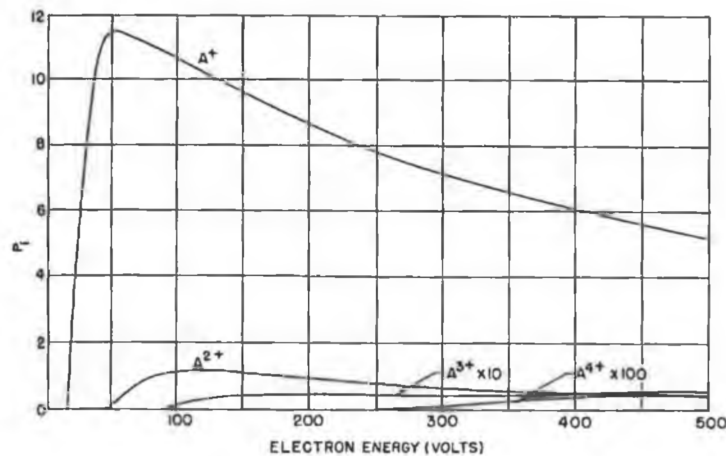

Figure 2.3[3] **Probability of ionization in argon against electron energy**

2.5.2 The Anode

The polarity of the anode sheath is such that ions are typically accelerated to 10-15eV before impacting the anode. The anode is also subject to bombardment form electrons and photons from the glow region. Due to these bombardments secondary electron emission in not uncommon form the anode. These secondary electrons are accelerated away form the anode and then act as fuel for the glow region.

Most of the power input to the anode is due to high-energy electrons that travel from the cathode sheath at high speeds. Ion currents can also be significant but are generally negligible for glow discharge configurations.

2.6 Charged Particles subjected to Magnetic Fields

We have seen the effects of electrical fields applied to plasma and the influencing effects they impose on electrons and ions. Magnetic fields in the same way cause charged particles to behave differently by altering their directional vectors by amount proportional to the magnetic field strength and gradient. Main applications for the use of magnetic field, in conjunction with electrical fields, is to establish closed plasma configurations contained in a limited volume. This is quite untypical for a gas to be altered in this way and it is why its properties distinguish it from all other states of matter. Some of the basic characteristic are described below, while more complex interpretations are left to literature[4,5].

A charged particle will obey the equation of motion

$$\frac{dv}{dt} = \frac{e}{m}(E + vxB) \qquad \text{Eqn 2.22}$$

where e and m are the particles charge and mass, E and B are the electric and magnetic fields respectively and v the particle velocity.

In the presence of magnetic fields a particle tends to travel along uniform magnetic field lines in a helical path around the field line. Alternatively, the particle is said to have a drift velocity induced by the electric and magnetic field. This drift velocity due to mutually perpendicular E and B field is written as

$$V_{ExB} = \frac{ExB}{B^2} \qquad \text{Eqn 2.23}$$

This velocity has both a perpendicular and a parallel component.

The helical path traveled by a particle takes the form of a circle with a radius known as the cyclotron radius at a frequency called the cyclotron frequency. These quantities are expressed as

$$r_c = \frac{mv_{\perp}c}{qB} \qquad \text{Eqn 2.24}$$

for the cyclotron radius and

$$\omega_c = \frac{qB}{mc} = \frac{ZeB}{M} \qquad \text{Eqn 2.25}$$

for the cyclotron frequency.

The gyration period, T, is inversely equal to the velocity v, and can expressed as

$$T = \frac{1}{v} = \frac{2\pi}{\omega_c} \qquad \text{Eqn 2.26}$$

From this, ion and electron cyclotron radius can be written as

$$r_i = \frac{Mv_i}{ZeB} \qquad \text{for ions}$$

$$r_e = \frac{Mv_e}{eH} \qquad \text{for electrons} \qquad \text{Eqn 2.27}$$

The centripetal force experienced by this particle traveling along a curved field line in a helical path causes a motion, which is written[4] as

$$V_{R.B} = \frac{v_{\parallel}^2}{R\omega_c}\frac{RxB}{BR} \qquad \text{Eqn 2.28}$$

where R is the field line radius and $v_{\parallel}$ the parallel component of velocity along the field line

The value of $v_{\parallel}$ is calculated form the total kinetic energy of the particle W, and its magnetic moment μ. It is expressed[4] as

$$v_{\parallel} = \sqrt{(2(W - \mu B)/2)} \qquad \text{Eqn 2.29}$$

and the magnetic moment

$$\mu = \frac{W_{\perp}}{B} = \frac{mv_{\perp}^2}{2B} \qquad \text{Eqn 2.30}$$

W being the constant total kinetic energy of the particle.

More of the important effects of magnetic and electric fields and their influences on plasma during deposition processes are dealt with in chapter four on magnetron sputtering.

Chapter Two References

[1] J. Vossen and W.Kern, Thin Film Processes, Academic Press, New York (1978) Chapter II-1.

[2] A. Sherman, Chemical Vapour Deposition for Microelectronics, Noyes Publications, New Jersey (1987) p48 - 55.

[3] S.C.Brown, Basic Data of Plasma Physics, American Institute of Physics, New York (1994) Chapter 4.

[4] L.A. Artsimovich, A physicist's ABC on plasma, MIR Publications, Moscow (1976).

[5] F. Kamenetskii, Plasma: The Fourth State of Matter, Plenum Press, New York (1972).

[6] B. Chapman, Glow Discharge Processes, Wiley, New York (1980).

[7] Hiden Analytical, Handbook of Plasma Diagnostics, Hiden Analytical, Warrington (1986).

Chapter Three

Thin Films

3.1 Introduction

The following chapter will give the reader a good overall insight into the general applications of thin films in the areas of integrated circuits and hard and protective. Descriptions of some common processes used to manufacture such films will be reviewed briefly and a description of how a film is formed, which is often mis-understood, is given towards the end of the chapter.

3.2 Thin Film Applications

The applications of thin films are of the utmost importance. From everyday devices, such as radios, to future environmental devices, such as efficient solar panels, thin films play an integral part in our lives. The following is a brief review of the widespread use of films deposited by different processes.

3.2.1 Semi-Conductors

As stated in the introduction, the semiconductor industry currently generates[1] over $140 billion through the manufacture and sale of semiconductor devices such as microprocessors, logic chips and RAMs. Advances in the design and performance of these devices, which fuels the demand would not be possible without the processes in place for their fabrication. The quality of these devices depends on the properties of the thin films used in their fabrication. The properties[2], for example, to be considered for electrical characteristics are no less than conductivity, resistivity, dielectric constant, dielectric strength, dielectric loss, stability under bias, polarization, permittivity, electromigration and radiation hardness. Not only do these films have electrical properties but also thermal, chemical, mechanical, morphological, optical and magnetic properties that have to be considered.

Table 3.1 shows a selection of fundamental properties of some materials used in semiconductor manufacturing processes. The three properties chosen here are

- Resistivity (ρ) – Determines the ability to function as an interconnect metallization.
- Coefficient of thermal expansion (CTE)– Determines the level of extrinsic stress.
- Melting point (T_{melt}) – Determines microstructure for a given deposition temperature.

Conductor	ρ (μΩ•cm)	CTE (x10^{-6}/°C)	T_{melt} (°C)
Copper (Cu)	1.70	17.0	1084
Gold (Au)	2.20	14.2	1064
Aluminum (Al)	2.74	23.6	660
Tungsten (W)	5.33	4.5	3407
Titanium (Ti)	43.1	8.5	1660
Titanium Nitride (TiN)	18	6.3	2930
Al Alloys	2.8 – 3.2		
CVD W	8 - 11		
Poly Si (heavily doped)	500 - 1000		
WSi	30 – 70	6.2	2165
$TiSi_2$	13 – 16	10	1540
$TaSi_2$	38 – 50	8	2200
Si (intrinsic)	> 1.5x10^8	2.3	1412
SiO_2	> 10^{18}	0.5	

Table 3.1[3] **Properties of semiconductor fabrication materials.**

One of the main requirements for successful integrated circuit fabrication is the filling of via and contact plugs. These plugs allow multilevel metallization (MLM) to be realized, which is another requirement for advanced IC fabrication and design.

The ability to fill these plugs by a particular process is usually described as the term step coverage, and is represented by the percentage of coverage of these holes.

The step coverage is expressed by the ratio of the minimum thickness of a film as it crosses a step, t_s, to the nominal thickness of the film on the flat regions, t_n. This is illustrated in figure 3.1 and can be written in equation form as

$$Step\ coverage(\%) = \left(\frac{t_s}{t_n}\right) * 100$$

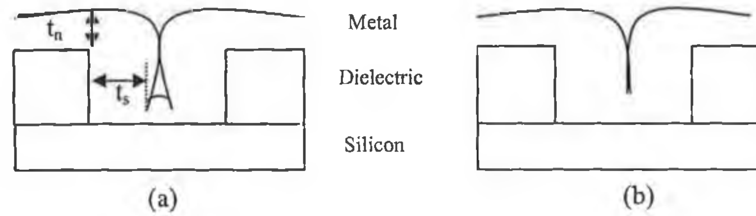

Figure 3.1. Representation of (a) poor step coverage and (b) good step coverage by a deposited film on a contact plug. As can be seen a void exists in plug (a), which can result in poor performance or device failure.

Multilevel metallization is the process of stacking transistor interconnect lines on top of each other, which allows for an increase in the density of transistors contained in today's integrated circuits. All transistors in a circuit, of which there can be millions, lie on the bottom layer of a chip. As device density increases so does the complexity of routing the metal interconnect lines between the transistors.
In general[4] it can be said that

- Greater density results in longer metal lines
- Longer metal lines are more resistive than shorter lines
- Maximum area for the metal is about 50% of the total surface area of the die

The circuit response time[4], τ, which limits the speed, depends on the resistance and capacitance of the interconnect

- Resistance slows current due to collisions
- Capacitance slows current due to charge accumulation

τ is calculated by the product of resistance times capacitance for a given interconnect line

$$\tau = RC = \left(\rho \frac{L}{w t_m}\right) \bullet \left(K_{ox} \varepsilon_0 \frac{L\,w}{t_{ox}}\right) \quad \text{Eqn. 3.2}$$

where w is the width of the metal line, ρ the metal resistivity, L the length of the interconnect, t_m the metal thickness and t_{ox} the thickness of the oxide, $K\varepsilon_0$ is the dielectric constant.

The first expression is for the metal, with the second being for the oxide or dielectric layer.

Multiple levels of metallization relieves the area constraint on interconnect wires for single layer devices. This is accomplished in two ways, firstly by designing interconnects that can bridge over one another and secondly, by using via plugs as vertical connections between levels in the dielectric layers. Figure 3.2 shows the interconnect lines on one layer of an integrated circuit and figure 3.3 shows a cross sectional schematic of an advanced CMOS transistor used in today's most advanced devices.

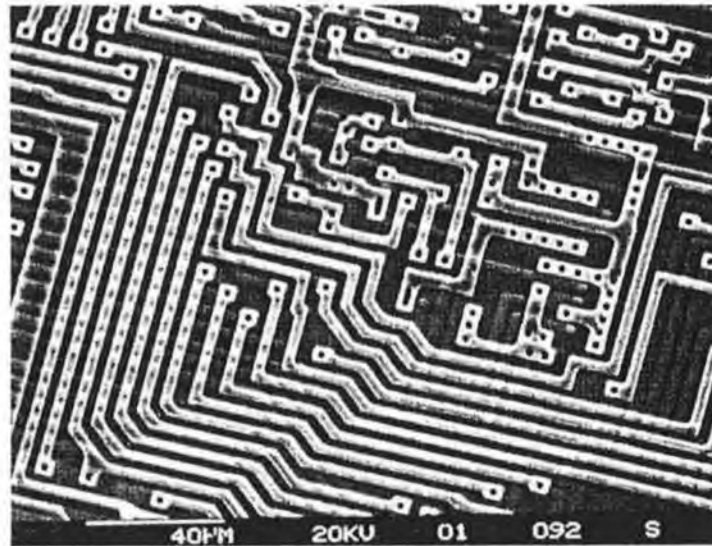

Fig 3.2[5]– SEM micrograph of metal interconnect lines.

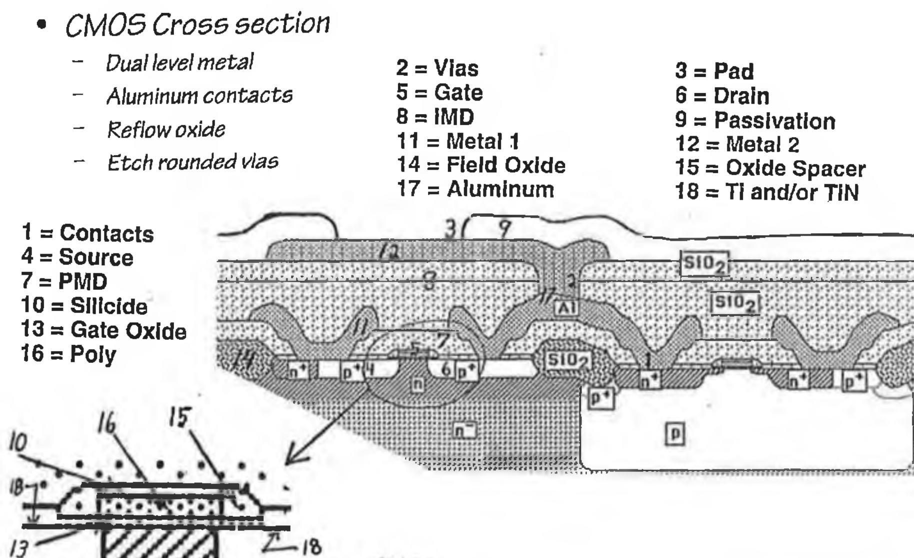

Figure 3.3[5] **Cross section of an advanced CMOS transistor.**

The number of process steps involved in the construction of such advanced transistors on silicon wafers is in the order of hundreds. Briefly, the formation sequences of one plug and interconnect layer will be looked at to illustrate the complexity and variety involved in the deposition of such dimension critical films.

As can be seen from figure 3.3, tungsten can be used as the contact and via metal. This is mainly due to its simple deposition characteristics (reduction of $WF_6(g)$) and its relatively good electrical and thermal characteristics as can be seen from table 3.1. Alternatives to tungsten are aluminum and copper. All three can be deposited by chemical vapour deposition (CVD) techniques but tungsten methods are best known and do not require plasma enhanced deposition, and therefore reduce the exposure of the wafers to ion and electron bombardment. This can avoid device breakdown due to current imbalances caused by the plasma. Aluminum can also be deposited by sputtering, but has step coverage only in the region of 70% for 0.25μm geometries. This step coverage will decrease with reductions in the trench width geometry of the steps, and as the aspect ratio increases. Copper deposited by PECVD is the newest technology available but is expensive and requires additional steps in the process. Some companies are turning to a tungsten diborane (B_2H_6) process, which reduces the resistance at tungsten grain boundaries (bulk resistivity < 8 μΩ-cm) and therefore increases device speed and yet still has the dependency and history of tungsten CVD process. The addition of small amounts of diborane reduces resistivity by promoting large grain growth and reducing fluorine concentrations. The reaction is as follows:

$$WF_6(g) + B_2H_6(g) \xrightarrow{400 - 475\ C} W(s) + 2BF_3(g) + 6HF(g)$$

Figure 3.4 shows the schematic diagrams of the formation of via and contact plugs by three different methods. The most simple is the selective tungsten plug technique, which has a single process step. Aluminum sputtering requires contact and barrier metal layers to prevent junction arcing, e.g. titanium and titanium nitride, respectively, but has step coverage problems and is not used for high speed devices such as microprocessors or memory chips.

The blanket tungsten process also requires high-density underlayers for adhesion (TiN) and a nucleation layer deposited before the main blanket for uniformity and adhesion considerations. Tungsten etchback is then required after the deposition step. Without etchback a blanket tungsten layer, if applicable, can provide a first level interconnect.

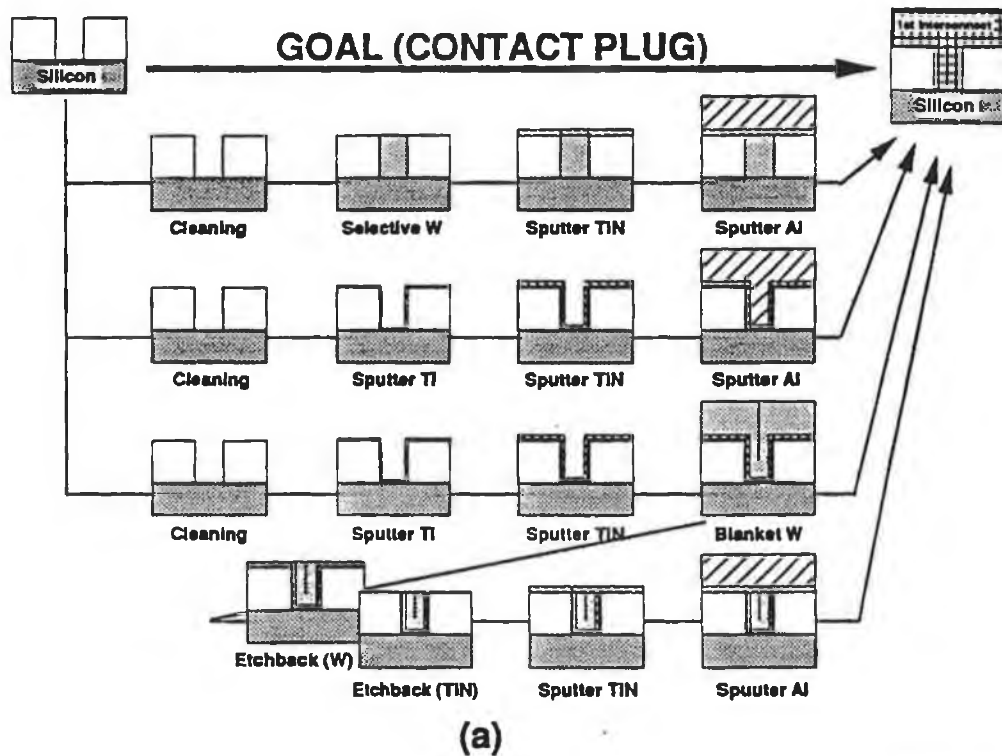

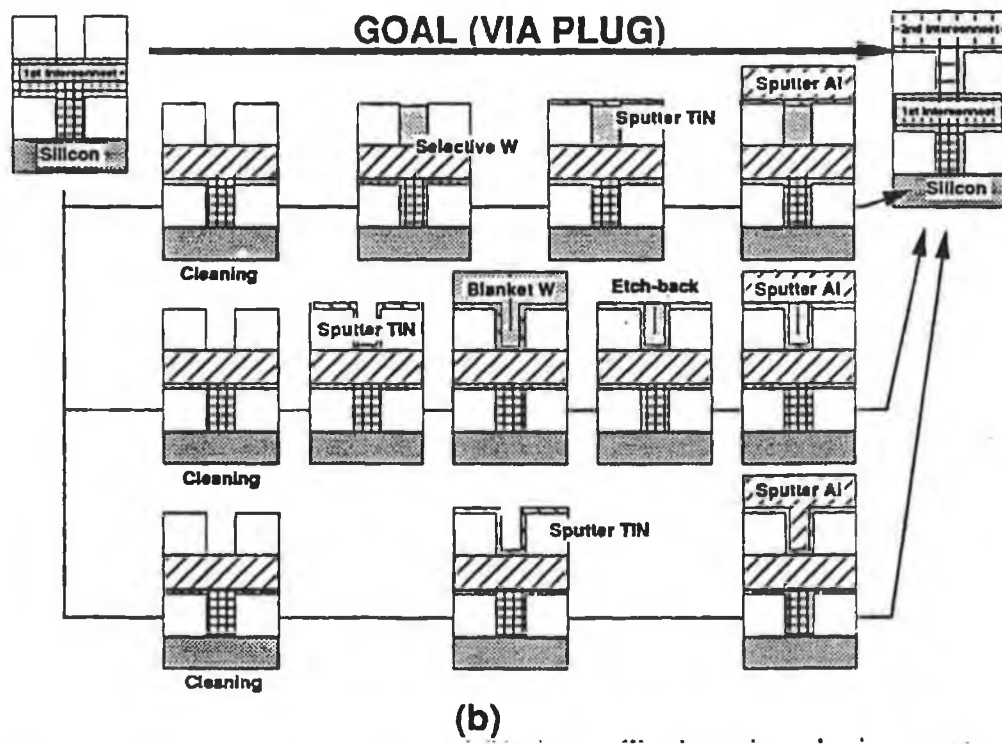

Figure 3.4 Schematic diagrams of (a) contact and (b) via metallization using selective tungsten, blanket tungsten and aluminium sputtering techniques

Table 3.4 shows a technology roadmap for the characteristics of Dynamic Random Access Memory (DRAM), which is the most common silicon based device technology today. This is unlikely to change in the foreseeable future. Cost-effectiveness, steadily increasing performance and consistently high levels of investment in R&D by IC manufacturers will keep CMOS the mainstream technology well into the next century.

Year of first DRAM shipment Minimum feature (μm)	**1998** 0.25	**2001** 0.18	**2004** 0.13	**2007** 0.10	**2010** 0.07
Memory	-	-	-	-	-
• bits/chip	256M	1G	4G	16G	64G
• cost/bit(millicents)	0.017	0.003	0.001	0.0005	0.0002
Logic (Micro-processors)	-	-	-	-	-
• logic transistors/cm^2	7M	13M	25M	50M	90M
Chip Frequency (MHz)	-	-	-	-	-
• on-chip clock, cost performance	200	300	400	500	625
• on-chip clock, high performance	450	600	800	1000	1100
• chip-to-board speed, high perf.	200	250	300	375	475
Maximum number of wiring levels (logic)	-	-	-	-	-
• On-chip	5	5-6	6	6-7	7-8
Minimum Interconnect CD (μm)	0.3	0.22	0.15	0.11	0.08
Contac/Via CD (μm)	0.28	0.2	0.14	0.11	0.08
Electrical Defect Density (d/m^2)	160	140	120	100	25
Contact / Via aspect ratio	-	-	-	-	-
• Logic	3:1	3.5:1	4.2:1	5.2:1	6.2:1
• DRAM	5.5:1	6.3:1	7.5:1	9:1	10.5:1
Chip Size (mm^2)	-	-	-	-	-
• DRAM	280	420	640	960	1400
• microprocessor	300	360	430	520	620

Table 3.4[3] Roadmap Technology Characteristics

Environmental issues associated with the fabrication of these devices have come under more and more scrutiny due to large chloroflourocarbon (CFC) productions. These quantities have been estimated to be equivalent to 1000 miles of a car journey per dielectric layer alone[6], along with other associated chemicals used in etch and implant processes. This attention has brought about increasing demand for high

performance processes with minimal waste and byproducts. From this, more focus has been put into the development of sputtering applications due to the non-toxic nature of the by-products and due to the minimal decontamination required of the process parts.

3.2.2 Hard and Protective Coatings

Hard and protective materials are another multi-billion dollar industry associated with thin film applications. These hard materials are principally carbides, nitrides, silicides and borides of the transition metals in groups III, IV, V, and VI as well as the first periods of the groups VII and VIII, which form interstitial solid solution structures. Belonging to this type is tungsten carbide (WC) which was the first hard material to be fabricated in 1900 by Moissan.

One of the main functions of a coating applied to a substrate is that of protection. The degree of protection and thus lifetime can be measured by examining the hardness of the coating applied.
Since hardness is not a fundamental property of a material, its value varies according to the test method. Hence, the test method needs to be specified. There are three main test methods, the Brinell test (BS 240: 1986), the Vickers test (BS 427: 1982) and the Rockwell test (BS 891: 1989). Exact details and procedures of each test are covered extensively in literature[7]. Table 3.5 outlines the main differences between the three and gives a brief description of each.

Test	Indenture	Load	Typical Application
Brinell (HB)	1-10mm diameter steel or tungsten carbide ball	Up to 3000kg for steel ball, depending on F/D ratio of material	Forged, rolled, cast components in ferrous and non-ferrous alloys
Vickers (HV)	Square based diamond pyramid	1-120kg	All metal alloys and ceramics, needs surface preparation
Rockwell B-Scale (HRB)	1/16 inch diameter steel ball	10kg Minor load 100kg Major load	Low - strength steels and non-ferrous up to HV of 240
Rockwell C-Scale (HRC)	Diamond cone or Brale	10kg Minor load 150kg Major load	All metals with a machined surface finish or equivalent.

Table 3.5 Comparison of standard hardness tests[7].

One of the first applications of thin hard coatings for machine parts were TiC coatings for ball bearings. This application shows nicely the principal goals for the protection of all machine parts:

- reduce the coefficient of friction
- reduce adhesive wear

- reduce abrasive wear
- assure function in non or poorly lubricated conditions

Reduced adhesive wear is desired mainly in the areas of cold working (dies, punches, coining tools etc.). Titanium carbide as a protective coating on high chromium and high carbon steels has proven its suitability in many cases. For high-speed steels the combination of titanium carbide with titanium nitride gives the best results.

CVD coatings for abrasive wear applications will show improvements in cases where the abrasive particles are smaller than approx. 0.1mm. These particle sizes are common in plastics. CVD coatings therefore successfully protect plastic-processing tools, with lifetimes often increased by a factor of 10 to 15 over nitrided tools.
In plastic processing, abrasive wear is often accompanied by corrosion due to outgasing of chlorine and fluorine compounds. In this field, combinations of chromium carbide with titanium nitride coatings have been proven successful.

Diamond like carbon (DLC) is a commonly accepted name for hard carbon coatings, which have mechanical, optical, electrical, and chemical properties similar to natural diamond, but do not have a dominant crystalline lattice structure[8]. Natural diamond exhibits bonding which are indicative of a carbon-to-carbon bond. On the other hand, graphite exhibits bonding indicative of a carbon-to-hydrogen bond. Generally speaking, the higher the carbon-to-carbon bonding percentage the closer the properties are to that of diamond.

DLCs come in two types, hydrogenated DLCs and amorphous diamond coatings (ADLC). These have some similarities, as well as some differences. The primary similarity between the two is that they are deposited at low temperatures, less than 250°C. The principle difference[9] is in the source of the carbon and the percentage of carbon-to-carbon bonding in the coating. Hydrogenated DLCs are formed through a CVD process, where the source of carbon is in the form of a hydrocarbon gas, whereas ADLCs are formed through a physical vapour deposition (PVD) process that uses a carbon (usually graphite) target.

The advantages of such coating properties are obvious. The wear rates and hardness exhibited by these films are second to none. Along with low coefficients of friction (<0.1) and densities (2 - 3.2 g/cm^3) they also exhibit extremely high hardness (~8000 to 10000 HV). One particular application of these films is in piercing of nonferrous materials, such as copper and aluminium, where TiN and TiCN performance has been marginal.

Diamond coatings used on blades exhibit a high degree of edge hardness, which reduces its friction coefficient. These blades last 8 to 14 times longer than uncoated stainless steel blades. They show consistent edge quality and cuts, will not chip, do not require resharpening, and reduce downtime incurred by maintenance due to breakage's and blade replacements.

Typical parameters of hard thin film coatings are:

- Coatings ranging from ½ to 100 microns thick.
- Boron carbide, silicon nitride, diamond and aluminum oxide.
- All applied less than 250^0C. Metallurgy of base metal not affected.
- Coatings with very low coefficients of friction.

Some common applications are injection molds, gears, blades, wear parts, shafts, bushings, and cutting tools. Below are some of the more common CVD reactions[10] used in the formation of films for these applications:

Film	Reaction
Titanium Carbide	$TiCl_4\,(g) + CH_4\,(g) \xrightarrow[950-1000^oC]{H_2} TiC\,(s) + 4\,HCl\,(g)$
Titanium Nitride	$TiCl_4\,(g) + \frac{1}{2}N_2\,(g) \xrightarrow[850-1000^oC]{H_2} TiN\,(s) + 4\,HCl\,(g)$
Titanium Carbonitride	$2\,TiCl_4\,(g) + R\text{-}CN \xrightarrow[700-900^oC]{H_2} 2\,Ti(Cx,Ny)(s) + xHCl(g) + RCl\,(g)$
Chromium Carbide	$7\,(1-x)\,CrCl_2\,(g) + 7\,(1-x)\,H_2\,(g) + 3\,(x\,Fe\text{-}C) \xrightarrow[1000^oC]{} (Crl\text{-}x\,Fex)\,7\,C3\,(s) + 14\,HCl$
Aluminium Oxide	$2\,AlCl_3\,(g) + 3\,H_2O\,(g) \xrightarrow[1000^oC]{H_2} Al_2O_3\,(s) + 6\,HCl\,(g)$

R = org. radical

x = 0 - 0.6

Fe-C = carbon dissolved in the austenite

All the above reactions rend hydrogen chloride as a byproduct. The reducing carrier gas (hydrogen) must be supplied in excess.

The selection of a hard coating material for a given application is governed by two factors[10]:

- Firstly, service conditions such as wear, friction, corrosiveness of the environment, temperature and the nature of any material in contact with the part must be considered.
- Secondly, the compatibility of coating and the base material is of importance. Their relative coefficients of thermal expansion, the possible chemical and metallurgical reactions between the two during coating procedures, which might produce soft or brittle interlayers have to be considered.

Table 3.6 gives some of the fundamental properties associated with hard and protective films and table 3.7 gives an overview of the benefits associated with some of the applications where these films are used. Table 3.8 shows the frequent combination of CVD hard coatings used with base materials.

Coating/ Treatments/ Substrates	Deposition Technique	Deposition Temperature (C)	Micro-hardness at 25C (HV 0.05)	Coating Thichness (um)	Max service temp (C)	Coating Colour
TiN	PVD	300 - 500	2300	1 - 5	600	gold-yellow
TiCN	PVD	300 - 500	3000	1 - 5	400	blue - gray
WC/C or TiC/C	PVD	< 250	1000	1 - 4	300	black - gray
CrN	PVD	<500	1800	1 - 15	700	silver - gray
TiAlN/TiNAlO	PVD	< 500	3300	1 - 5	800	-----
Poly. Diamond	CVD	~ 800	10000	3 - 5	600	gray - clear
TiC / TiN	CVD	~ 1050	3000	5 - 8	600	yellow
VC	Toyota Diff.	~ 1000	2900	-----	-----	grey - brown
Nitrided Steel	Diffusion	< 500	1100	N/A	-----	Sub-surface white layer
Hard Chrome	Electroplate	40 -70	1100	2.5 to 500	400 +	silver - gray
a - Diamond	PVD	< 250	~ 8000	-----	-----	-----
Cold work steel	N/A	N/A	750	N/A	< T.T.	N/A
High Speed steel	N/A	N/A	900	N/A	< T.T.	N/A
Powder Metallurgy steel	N/A	N/A	900	N/A	900 +	N/A
Cemented Carbide	N/A	N/A	1700	N/A	-----	N/A

Table 3.6[11] Properties of Various Hard Coating / Diffusion Treatments and Substrates

Applications	Benefits
Cutting	Increased tool life Larger chip volume Reduce cutting forces Reduce downtime More regrinds possible Smother workpiece surfaces
Punching	Increased tool life Smoother cuts without burrs so less finishing Reduced cold welding More regrinds possible Perforation distances may be shorter that material thickness
Forming	Increased tool life Improved behaviour of the material being formed Easier workpiece ejection Smoother workpiece surface
Plastics Processing	Increased tool life Easier mould release Low tendency towards deposits in the mould so less cost Improved flowability of the plastic material Less machine downtime Shorter cycle times
Precision Contacting Components	Increased life Reduced friction gives smoother contact Can run for short periods without lubrcant
Aluminium and Zinc Die Casting	Less adhesive wear

Table 3.7[11] Benefits associated with PVD film coating (Information form Balzers)

It is important to have the understanding that hard and protective films should not be viewed as an add-on to a tool. They must be regarded as a single variable in a process that has many other interdependent factors such as substrate material, substrate hardness, substrate geometry, surface finish, the application of the tool and the materials with which it will come into contact with.

Material	Constituents	Titanium Carbide	Titanium Nitride	Titanium Carbonitride by MT-CVD	Chromium Carbide	Aluminium Oxide	Heat Treat ment after coating
High carbon, high chromium cold work steels(AISI D grades)	1.5-2.3%C 12%Cr+Mo,V,Co	x					no
Air hardening tool steels (AISI A grades)	0.7-2.2%C/ 1-5%Cr+V.Mn. W,Ni, 1-1.5%,Mo	x		x	x		no
Oil hardening tool steels (AISI O grades)	0.9-1.5% C,W, Mo or Cr	x		x	x		yes
High speed steels (AISI M and T grades)	0.7-1.6%C, 4% Cr Mo, W, Co, V	x	x	x			yes
Hot work steels (AISI H grades)	0.35-0.5%C, 3-13% Cr, W, Mo, V		x		x		no
Martensitic stainless steels (AISI 400 series)	0.15-1.05% C, 12-17% Cr	x			x		no
Cemented carbides ISO P and M grades	WC, TiC, TaC, NbC, Co	x	x	x		x	no
Cemented carbides ISO K and G grades	WC, Co			x		x	no
Alloy steels	up to a total of 4% of the following Mn, Si, Ni, Cr, Mo			x	x		yes
Austenitic, Ferritic, Stainless Steels	11-27%C, 3-15%Ni, 1-10 Mn+Mo, Nb, Ta		x	x			no
Heat resisting alloys	Fe-, Ni-, Co- base		x			x	depend on typ
Refractory metals and alloys	W, Mo, etc.		x			x	

Table 3.8[10] Frequent combinations of CVD hard coatings and base materials

Figure 3.5 shows the wear rate relationship of bare alloys and of hard coatings using an abrasive test method. The improvements seen are immense. Figure 3.6 shows the relative lifetimes of bearings tested with different hard coatings applied.

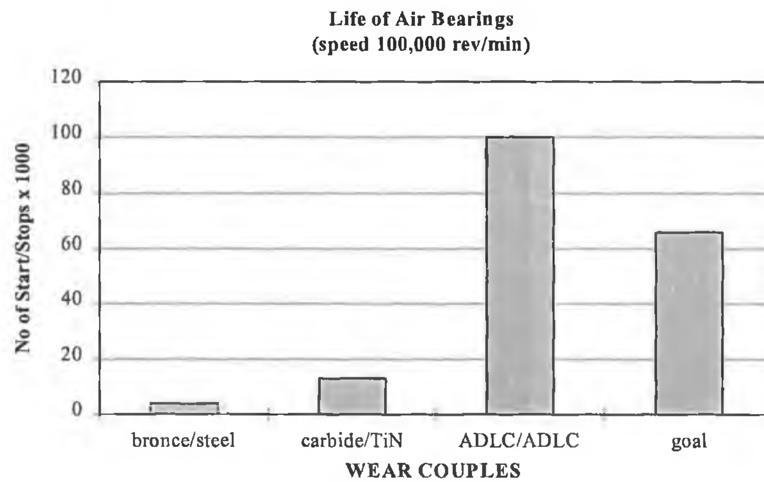

Figure 3.5[12] Comparison of film-coated air bearing lifetimes.

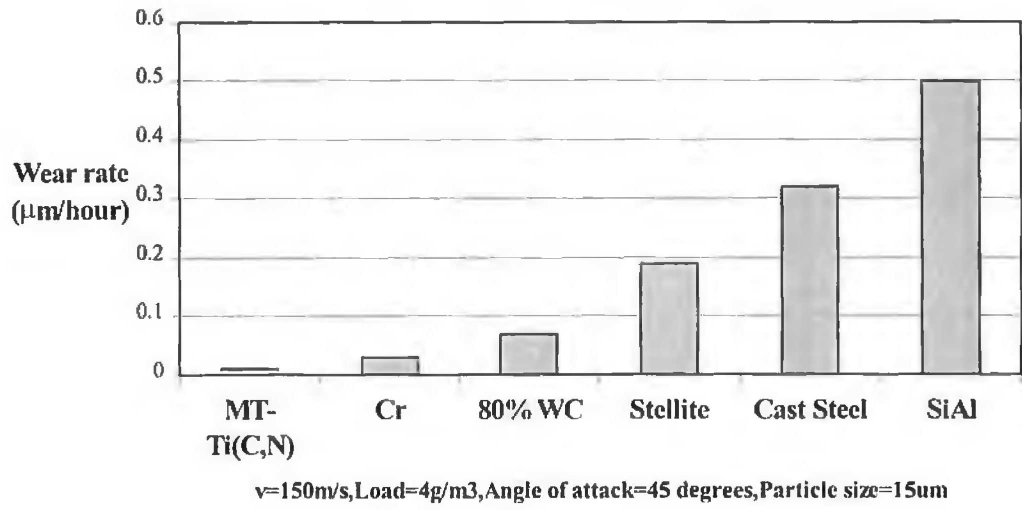

Figure 3.6[12] Comparison of wear rates on different films for abrasive testing.

3.3 Thin Film Processes

There are dozens of deposition technologies available to grow thin films. Since we are concerned with the thin film deposition range of a few nano-metres to about ten microns, the task is somewhat reduced.

A classification scheme[2] is shown in table 3.10 that gives a good idea of the categorization of the different deposition technologies. Attention will be paid to the glow discharge section, as this process is the main subject of this thesis. Information on the other technologies, evaporative methods,[2,15] gas phase chemical processes[2,15] and liquid phase chemical techniques[2] is vast and covered substantially by literature.

1. Evaporative Methods	
• Vacuum Evaporation	
Conventional vacuum evaporation	Molecular-beam epitaxy (MBE)
Electron-beam evaporation	Reactive evaporation
Resistance evaporation	Electron beam evaporation
2. Glow-Discharge Processes	
• Sputtering	• Plasma Processing
Diode sputtering	Plasma-enhanced CVD
Reactive sputtering	Plasma oxidation
Bias sputtering (ion plating)	Plasma anodization
Magnetron sputtering	Plasma polymerization
Ion beam deposition	Plasma nitridation
Ion beam sputter deposition	Plasma reduction
Reactive ion plating	Microwave ECR plasma CVD
ECR sputtering	Cluster beam deposition (CBD)
3. Gas-Phase Chemical Processes	
• Chemical vapor deposition	• Thermal forming processes
CVD epitaxy	Thermal oxidation
Atmospheric-pressure CVD (APCVD)	Thermal nitridation
Low-pressure CVD (LPCVD)	Thermal polymerization
Metalorganic CVD (MOCVD)	
Photo-enhanced CVD (PHCVD)	
Laser-induced CVD (PCVD)	
Electron-enhanced CVD	Ion implantation

4. Liquid-Phase Chemical Techniques	
• Electro processes	• Mechanical techniques
Electroplating	Spray pyrolysis
Electroless plating	Spray-on techniques
Electrolytic anodization	Spin-on techniques
Chemical reduction plating	
Chemical displacement plating	
Electrophoretic deposition	Liquid phase epitaxy

Table 3.10[2] Classification of Thin Film Deposition Technologies

3.3.1 Glow-Discharge Process Technologies

The glow-discharge process is by far the most important and widespread process technology in use today. Most of integrated circuit fabrication uses technology based on the glow discharge process, from magnetron sputtering to plasma enhanced CVD processes. Hard and protective material coatings, over the past ten years, have come to rely heavily on the deposition processes that are born from the glow discharge process, as a majority are applied using PVD or PECVD techniques.

The two categories of film deposition that come under glow discharge are sputtering and plasma processing (table 3.10). In the following sections plasma processing and sputtering technology will be dealt with, leaving a detailed description of magnetron sputter technology until chapter four.
A detailed description on the formation of a glow discharge has been given in chapter two.

3.3.1.1 Plasma Processing

Plasma processing is the general term used to describe gas/gas and gas/surface reactions accelerated at a particular temperature due to the presence of plasma. This plasma can be generated thermally (>5000 ^{0}C) or by introducing radio frequency or microwave energy into the system. The process is carried out mainly at pressures between 1 Pa and atmosphere, but can and is also carried out at pressures up to 4 E4Pa (Sub-Atmospheric CVD).

As all CVD reactions require high temperatures (1000°C typically), this limits their applications for coating temperature sensitive materials. By introducing a radio frequency or microwave plasma source, the thermal energy requirements are reduced so that the chemical reactions take place at equivalently 'high' temperatures due to high ion and electron energies generated within the plasma body. Characteristics of electrically generated plasmas are given below in table 3.11.

Frequency	50 KHz to 13.45 MHz 2.45 GHz (microwave)
Power	kWs
Flow rate	mg/s
Electron density	$10^9 - 10^{12}/cm^3$
Pressure	< 10 Torr (typically)
Electron temperauture (K)	10^4
Atom temperature (K)	2×10^2

Table 3.11 Characteristics of plasma processing glow discharge.

Hard and protective coatings up to 2mm thick can be deposited using surface treatments such as plasma oxidation (O_2), plasma nitriding ($N_2 + H_2$) and plasma carburizing (CH_4). This is usually carried out by making the workpiece a cathode and introducing rf power in order to establish a glow discharge. The plasma dissociates the carrier gas(es) and film growth take place on a metal substrate[2].

Plasma-enhanced CVD (PECVD) or plasma-assisted CVD (PACVD) is a common method used for the deposition of inorganic and organic films. The basic reaction mechanisms are due to ion-molecule and radical-molecule dissociation of the organic and inorganic molecules. These interactions also cause the formation of polymerized species in the plasma body.

PECVD is a gas phase reaction that takes the form of :

$$A(g) + B(g) \xrightarrow{plasma} C(s) + D(g)$$

The difference in thermal energy requirements between PECVD and the same thermal CVD reaction can be seen on silicon nitride films[16] that are deposited on integrated circuits as passivation layers.

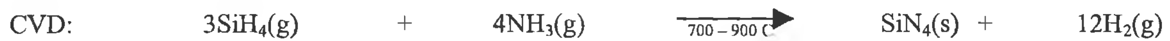

CVD: $$3SiH_4(g) + 4NH_3(g) \xrightarrow{700-900\ C} SiN_4(s) + 12H_2(g)$$

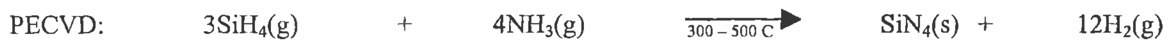

PECVD: $$3SiH_4(g) + 4NH_3(g) \xrightarrow{300-500\ C} SiN_4(s) + 12H_2(g)$$

Clearly, the difference in reaction temperature points to large advantages such as reactor design for lower temperatures, less hazardous environment and faster processing time. The trade-off is that the substrate is exposed to ion, neutral and electron bombardment from the plasma during film deposition. This

in turn can have positive and negative effects, depending on the substrate and application, as will be discussed in the section on thin film growth. More reaction comparisons are given in table 3.12 below.

Compounds	Reactants	Atm CVD (°C)	PECVD (°C)
Si_3H_4	SiH_4 $NH_3(N_2)$	700 – 900	300-500
SiO_2	SiH_4 N_2O	900 – 1200	200 - 300
Al_2O_3	$AlCl_3$ O_2	700 – 1000	100 – 500

Table 3.12[16] **Deposition temperature comparison between Atmosphere (Atm) CVD and plasma (PECVD) CVD reactions.**

In plasma the electron energy is much higher than that of the ion or neutral energy[17], these electrons are also in state of thermal non-equilibrium[17]. Even though the energy of ions and neutrals is relatively low, these particles become exited due to collisions with fast moving energetic electrons. This exited state is equivalent to a state of high temperature due to mobility increases. The reaction is then able to take place at a lower overall reactor temperature.

Figure 3.7 shows a example of a typical plasma processing chamber. All gases are feed into the chamber via mass flow controllers and dispersed uniformly through a showerhead which is usually a aluminium plate with numerous evenly spaced small diameter (< 1mm) holes. The plasma is ignited at the required process pressure by inducing an rf (13.56MHz typical) voltage, usually at a few kilovolts, onto one electrode. This voltage generates a plasma between the substrate (anode) and the showerhead (cathode).

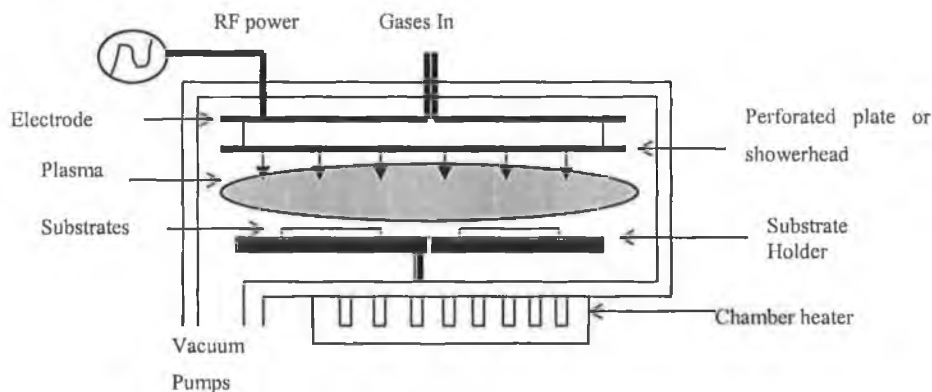

Figure 3.7 **Basic schematic of a PECVD reactor chamber with all main components.**

Deposition variables which must be controlled for a plasma reaction include power, total pressure, reactant partial pressure, flow rates, flow direction, pumping speed, substrate temperature, discharge

frequency, chamber resistance, reactor geometry, electrode spacing and configuration. These variables determine the film parameters and characteristics such as stress, thickness, microhardness and microstructure.

A plasma enhanced CVD reaction[17,18] can be broken into four steps from primary reaction to deposition. These steps can be listed as follows:

(1) The initial reactions between the limited amount of electrons and reactant gas form a mixture of ions and free radical species between the two electrodes (table 3.13). This occurs at the start of the plasma formation.

(2) The reactive species are transported towards the substrate while undergoing numerous collisions on the way (ion-ion, ion-molecule, molecule-electron, ion-neutral, etc..) and thus reducing the impact energy to a few electron volts while also creating new active species in the plasma.

(3) The reactive species are nucleated onto the substrate surface and promote film growth.

(4) The rearrangement processes where the reactive species or their reaction products grow into the film are ejected from the surface back into the plasma.

Table 3.13 shows a selection of possible electron interaction with the process gases after the generation of plasma.

Excitation:
$e^- + A_2 \longrightarrow A_2^* + e^-$
Dissociative Attachment:
$e^- + A_2 \longrightarrow A^- + A^+ + e^-$
Dissociation:
$e^- + A_2 \longrightarrow 2A + e^-$
Ionization:
$e^- + A_2 \longrightarrow A_2^+ + 2e^-$
Dissociative Ionization:
$e^- + A_2 \longrightarrow A + A^+ 2e^-$

Table 3.13[2] Initial electron-molecule impact reaction and the formation of reactive species (* indicates an atom in an energized state).

The advantages of PECVD include high deposition rates, better uniformity due to the lower reaction pressure and less substrate heating. Effects such as particle bombardment during deposition have been shown to improve packing density and film microstructure[19].

The limitations are that it is difficult to form a pure film due to the low deposition temperature. Hydrogen and water vapour remain as inclusions in the film. This can have adverse effects when depositing

films such as nitrides and oxides as stoichiometry is rarely achieved. Ion, neutral and electron bombardment of delicate devices due to plasma interaction can also have adverse effects such as over heating.

Cluster beam deposition (CBD) *or Ion beam deposition* (IBD) is classified as an ion assisted deposition technology. In this complex method of film deposition, highly pure films can be grown with excellent growth control capabilities[15]. Heating a source in a crucible, which is separated from the main chamber by a nozzle, forms a vapour. This vapour is at a pressure several orders of magnitude higher than the deposition chamber and so is drawn into the chamber through the nozzle and expands as it cools. The vapour then rains down on the substrate and nucleation begins. The energy of the vapour can be controlled with well-designed bias voltages or an electron beam device that then is used to effect the deposition kinetics of the film.

Microwave electron cyclotron resonance (ECR) plasma CVD is a deposition process that operates at a pressure of 0.1 to 0.001 Pa. A schematic of an ECR deposition chamber is illustrated in figure 3.8. The advantage of this process is that no substrate heating is required. Highly activated plasma is magnetically confined in the plasma chamber, which is excited by a 2.45GHz supply through a waveguide. Ions are extracted from the plasma chamber in the form of a plasma stream, which is guided to the substrate with a divergent magnetic field.

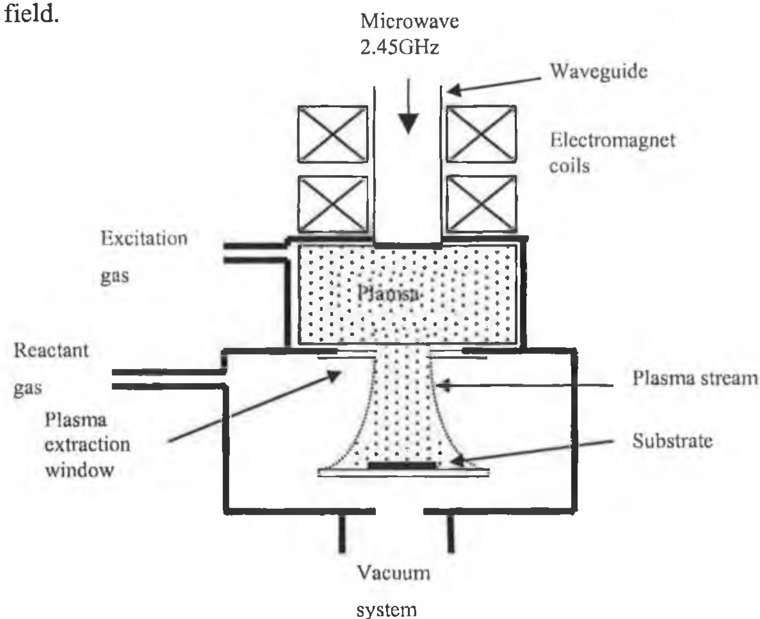

Figure 3.8[17] Schematic of a ECR plasma deposition apparatus

Ions are guided to the substrate by a gradually weakening magnetic field from the main plasma chamber. This is made possible by high-energy electrons accelerated toward the substrate due to the magnetic field guide. These electrons bring about a negative or floating potential on the substrate, which is

electrically isolated from the main plasma chamber. This, in turn, generates a static electric field along the stream that attracts plasma ions and guides them toward the substrate.

3.3.1.2 Sputtering Process

Sputtering is the most basic and well known of the glow discharge processes. This is the ejection of atoms from a target or electrode due to momentum transfer from impinging gas ions accelerated by a large potential difference between the two electrodes. Figure 3.9 shows the basic idea of ion bombardment of a target while figure 3.10 illustrates the surface interaction between ions and the target during sputtering. An inert sputter gas is generally used because it will not react with the target surface. There are five such inert gases, He, Ne, Ar, Kr, Xe. Argon is usually chosen as it is cheap, has a large atomic diameter to give acceptable sputter rates and is easy to source.

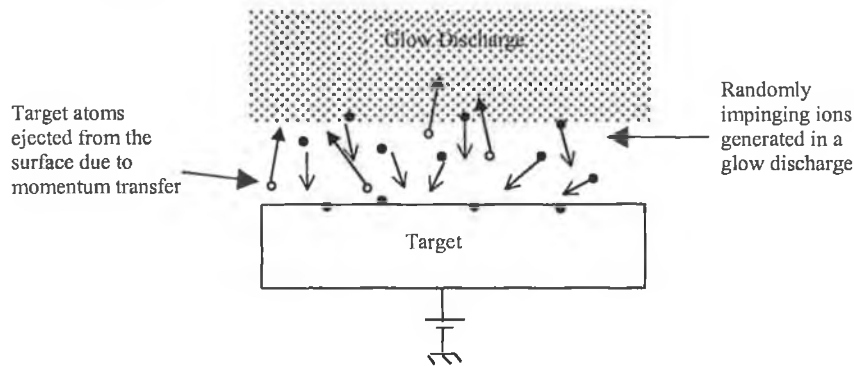

Figure 3.9 A simplified diagram of sputtering from a target.

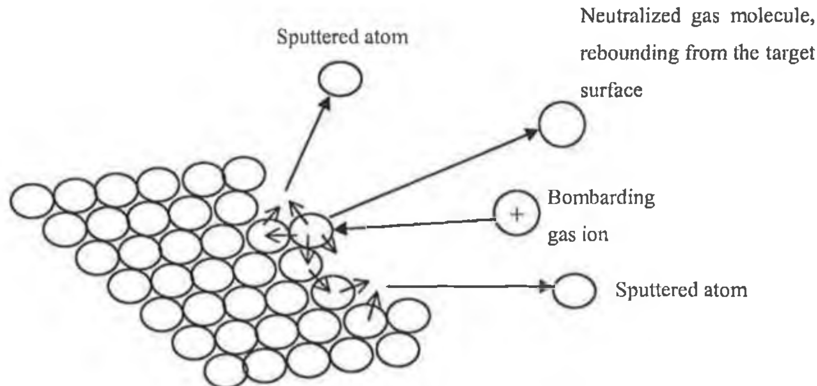

Figure 3.10[20] Gas atom / surface interaction at a sputtering target.

The gas ion / target interaction can be compared to breaking a rack of billiard balls with a cue ball. Even normal incidence ions can result in the ejection of material in the opposite direction due to the contribution of lattice elastic energy in the target material.

The maximum transfer of energy possible (T_{max}) according to elastic collision theory is given by[21]

$$T_{max} = \frac{4M_1M_2}{(M_1 + M_2)^2} E \qquad \text{Eqn 3.3}$$

where M_1 and M_2 are the incident ion and target atom masses respectively and E the incident ion energy.

Kinetic Effects

Kinetic effects transferred to the surface material due to the collisions of argon ions with surface atoms can cause

(1) Heating of the surface
(2) Creation of defects due to atomic rearrangement
(3) Implantation of ions in the surface
(4) Dissociation of surface molecules
(5) Ejection of material from the surface
(6) Scattering of incident ions from the surface
(7) Emission of x-radiation from the target (if ions energies are high enough, >1keV)

Events (2), (3), (4) and (5) are important in reactive ion etching, while event (5) is important in sputtering. Events (1), (6) and (7) are important in sputtering under some conditions if devices being coated are exposed to the resultant radiation or bombardment by reflected incident ions.

Secondary Electron Emission Coefficient

The current through the discharge can be expressed as the sum of the ion current, I_i, and the cathode current, I_e.[21]

$$I = I_i + I_e \qquad \text{Eqn 3.4}$$

At the cathode, the current is a direct function of the ion current, expressed as

$$I_e = \gamma I_i \qquad \text{Eqn 3.5}$$

$$I = I_i + \gamma I_i = (1 + \gamma) I_i \qquad \text{Eqn 3.6}$$

where γ is the secondary electron emission coefficient for ion bombardment at the cathode surface. Thus,

the secondary electron emission coefficient is low for metals, which means that most of the current in the plasma is due to ions and that the efficiency of the sputtering is high. The greater γ is for a given current, *I*, the smaller I_i becomes. This is expressed as

$$I_i = \frac{1}{1+\gamma} \qquad \text{Eqn 3.7}$$

This is the reason that oxide targets sputter at a lower rate for a given current than metallic targets (since they have a higher γ).

Sputtering Yield

Sputtering yield refers to the amount of material (atoms) removed from the target by one incident ion. Sputter yield depends on mass, energy and incident angle of the bombarding ion. Some values for different sputter gases are illustrated in figure 3.11 for a copper target.

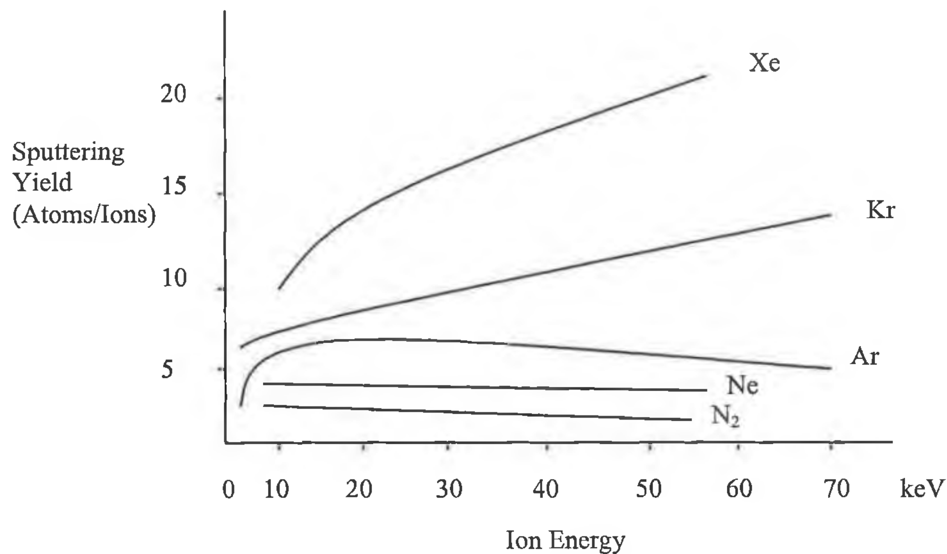

Figure 3.11[22] **Ion sputter yield dependence on ion energy and mass.**

Substantial information has been gathered on sputter yield for all possible target materials and is covered extensively by literature[22]. Some typical values for argon bombardment at 500eV are C = 0.12, Ti = 0.051, Al = 1.05 and Cu = 2.35 target atoms/ion.

Only a fraction of the incident ion energy is transferred to the ejected atom. This fraction is given by[21]

$$\varepsilon = \frac{4M_i M_t}{(M_i + M_t)^2} \qquad \text{Eqn 3.8}$$

where ε is the energy transfer function, M_i the incident ion mass and M_t the ejected target atom mass.

From this expression, assuming that normal incidence to a polycrystalline material, the sputter yield can be written as[21]

$$S = k\varepsilon \frac{E}{U} \alpha \left(\frac{M_t}{M_i} \right) \qquad \text{Eqn 3.9}$$

where k is a constant for a particular material.

The yield is directly dependent upon the energy transfer function ε. The term $\alpha(M_t/M_i)$ is a near linear function of M_t/M_i, E is the kinetic energy of the incident ion and U is the heat of sublimation of the target material. The term εα does not vary greatly from material to material. The primary sensitive factor is the heat of sublimation, which is first order dependent. The outcome of this dependence is that most materials have sputter yields within an order of magnitude of one another.

The sputter yield is also dependent on the ion angle of incidence. This is uncontrollable in most processes and random, but to processes such as ion beam deposition the angle of the target, with respect to the incident beam, can be altered. This is important for increasing deposition rates at constant power levels and for reducing unnecessary heating.
The following figure shows the effect of impinging ion angle.

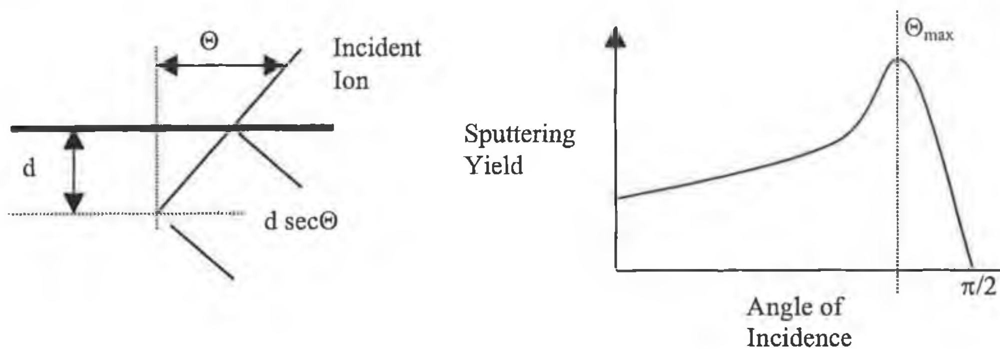

Figure 3.12 Graphical representation[15] on the dependency of sputter yield on angle of incidence of the impinging ion.

The first reliable sputter yield data was collected experimentally by Laegreid and Wehner in 1959[24]. The results for argon ions at 400eV are shown in figure 3.2.11. These values are still widely in use today.

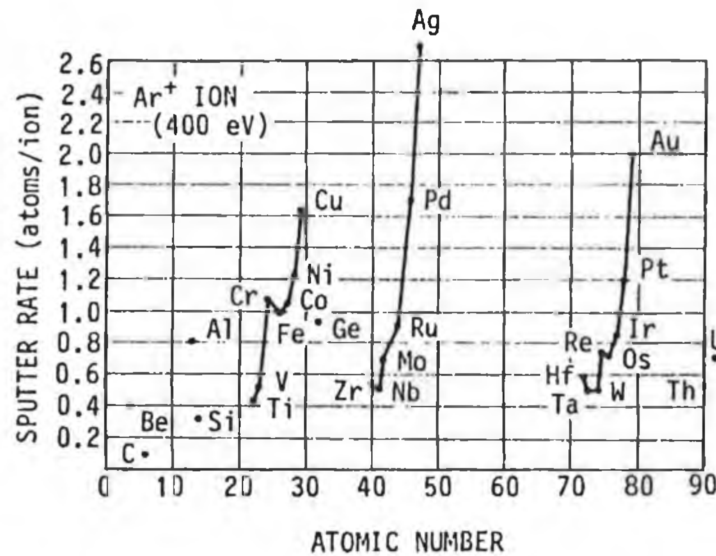

Figure 3.13[24] Sputter yield against atomic number for Ar^+ at 400eV.

Some of the common techniques for determining the sputter yield of a target are

1. weight loss of target
2. decrease of target thickness
3. collection of sputter material
4. detection of sputter particles in flight

The following can be said in summary of the general characteristics of sputter yield

(1) S increases with ion energy from a threshold of a few tens of electron volts to a maximum of around 10-20KeV[24]. S then decreases due to ion implantation[15] processes.

(2) S generally increases with the mass of the bombarding ion (figure 3.13).

(3) S increases with angle of incidence away from the normal incidence, to a maximum at an angle, which is dependent on energy, target and ion species, and then decreases to zero at the grazing incidence (Figure 3.12).

(4) S depends on target material, but is generally within an order of magnitude for all materials (Figure 3.13).

(5) The energy[24] of sputtered particles is in the range of tens of electron volts, with a small fraction at higher energies.

Mean Free Path

The mean free path is the average distance traveled by a molecule between collisions with other gas molecules. This value decreases with increasing process pressure and temperature.

The mean free path of a target atom determines the impact energy that atom will have on the substrate. It controls this energy through the number of collisions an atom will undergo over a certain distance before it impacts upon the substrate surface. The majority of the target atoms traverse the discharge as neutral atoms. The mean free path is calculated in the form of

$$\lambda_1 \cong \frac{c_1}{\nu_1} \qquad \text{Eqn 3.10}$$

where c_1 is the mean velocity of sputtered atoms and ν_1 is the mean collision frequency which is calculated from[24]

$$\nu_1 \approx \pi(r_1 + r_2)^2 c_1 n \qquad \text{Eqn 3.11}$$

where r_1 and r_2 are the atomic radius of the sputtered atoms and discharge gas molecules respectively, n is the density of the discharge gas, which is a function of the pressure.

The mean free path is then a combination of these two equations[24]

$$\lambda_1 \cong \frac{1}{\pi(r_1 + r_2)^2 n} \qquad \text{Eqn 3.12}$$

where

$$n = \frac{p}{kT}$$

(p - pressure,k – boltzmann constant and T - temperture (K))

The mean free path is also important when talking about gas ions, as the impact energy of gas ions on the target surface is effected in the same way.

3.3.1.3 DC Diode Sputtering

In this, the simplest of the sputtering technologies, a target is located in vacuum and biased negatively. The chamber is evacuated to a low base pressure (10^{-5} Pa) and back-filled with the sputter gas. An anode is placed several centimeters from the cathode and a glow discharge is ignited between them. The

nature of the glow discharge, as described in chapter two, is typified by a large potential drop within the first few centimetres of the target, referred to as the cathode sheath. Ions generated in the plasma are accelerated across this potential and bombard the target. The ejected atoms condense on the substrate and form a film.

This type of sputter deposition is slow (50nm /min typical) and requires large voltages in order to drive the cathode (1-5kV). Current densities measured at the substrate is typically 1mA cm^{-2}. The deposition is usually carried out between 3 and 15 Pa.

This technique is not adequate for non-conducting targets, as electron replenishment is not possible from the surface of an insulator target, or for reactive sputtering due to target poisoning issues.

A DC diode sputtering system schematic is given in figure 3.14 below.

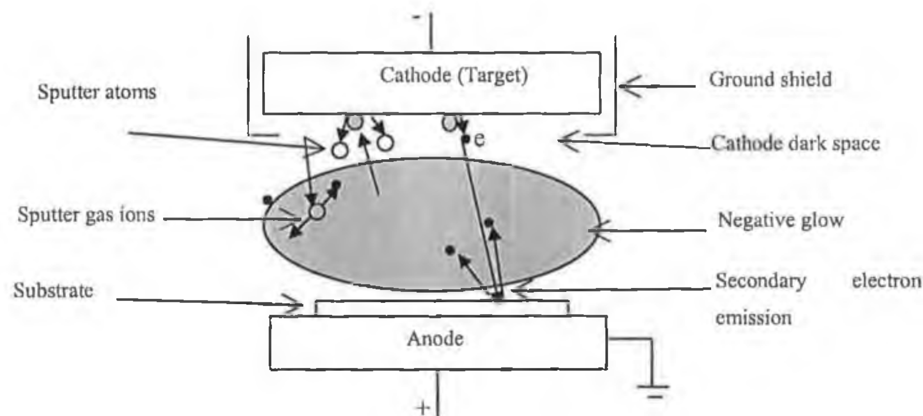

Figure 3.14 Schematic representation of a DC diode sputter system

3.3.1.4 RF Sputtering

Radio frequency power is commonly used to overcome the problems with the DC diode configuration to sputter insulator targets. The only difference between the set up of a DC diode and RF sputter system is the power supply and a matching network, which is required for impedance matching between the RF supply and the chamber. The power supply impedance is typically 50Ω. The frequency of RF energy used is fixed at 13.56MHz by the Federal Communication Commission (FCC) for industrial, research and medical uses.

The implications of applying radio frequency energy to an electrode are, at these high frequencies, the difference between atom/ion and electron mobilities are significant[21]. This mobility difference leads to the formation of a negative potential on the target in the following way:
Initially, at (t=0), the electrode surfaces contain no charge. The applied negative bias causes positive ions from the discharge to be accelerated towards the insulator electrode, and strike it, to leave behind a positive charge on the surface as electrons are removed. During the positive half of the cycle electrons are attracted and collected by the target. Mobility imbalances dictate that the positive cycle attracts more electron charge than ion charge collected by the negative cycle. At the completion of one cycle the net effect is the build-up of negative charge on the target. This build-up effect only takes place over the first few cycles as a stage is reached where the negative bias will repel electrons and attract ions to a degree. The negative bias can build up to a value almost as high as the applied voltage. If the potential difference between the discharge and the self-biased electrode is sufficiently large, ions will be accelerated strongly towards the target and initiate sputtering.

Unfortunately, this negative bias effect can build up on both electrodes. Precautions can be taken in order to make sure that the target is the sputtered electrode. Namely, to ground the non-sputtering electrode and restrict the sheath voltage V_B (anode electrode) to be as small as possible and to make V_A (target) to be as large as possible. The effects of electrode sheaths can be explained as follows:
We assume that electrodes A and B have areas A_A and B_B. Sheath voltages are established due to ion fluxes J, which can be equated[25] from

$$J = \frac{KV^{\frac{3}{2}}}{\sqrt{m}D^2} \qquad \text{Eqn 3.13}$$

where V is the voltage drop across the sheath, D is the dark space thickness, m is the ion mass and K is a constant.
Since positive ion current density must be equal at both electrodes, then we can write

$$\frac{V_A^{\frac{3}{2}}}{D_A^2} = \frac{V_B^{\frac{3}{2}}}{D_B^2} \qquad \text{Eqn 3.14}$$

The large voltage drop across the dark space implies a region of limited conductivity. This can be modeled as a capacitance proportional to electrode area and inversely proportional to D:

$$C \propto A / D \qquad \text{Eqn 3.15}$$

For a RF voltage that is divided between two capacitors in series, we can write

$$\frac{V_A}{V_B} = (A_B / D_B)(D_A / A_A) \qquad \text{Eqn 3.16}$$

And substituting in to equation 3.14 we get

$$\frac{V_A}{V_B} = \left(\frac{A_B}{A_B} \right)^4 \qquad \text{Eqn 3.17}$$

This implies that the larger dark-space voltage will develop at the electrode with the smallest surface area. To ensure the non-sputtered electrode is larger, and so develops a small self-bias, the chamber is usually connected to the same ground potential as the electrode and the power supply. This will ensure a larger voltage developed across the target.

RF sputtering is operated at pressures much less than the DC diode configuration, usually between 0.1 and 3 Pa. This is for two reasons. Firstly, secondary electrons are not lost to the same extent as in DC sputtering as they are reflected between the two electrodes, and secondly, the high frequency process causes enhanced ionization due to increases in particle mobility and so collisions.

3.3.1.5 Bias Sputtering

This technique simply involves the application of a negative bias to the substrate. This bias encourages film bombardment during deposition. Care must be taken in choosing a suitable bias voltage as too high a value can cause the entire film to be bombarded or eroded from the surface, or not to be deposited at all. Typical ion energies[19] will be a few eV to a few tens of eV. Typical bias voltages are set at –100V.

The application of a bias voltage has implications for the nucleation stage of the film. Ion bombardment of the substrate induces large grain nucleation, which leads to a stronger, more adhesive film. In mid-deposition, this bombardment helps[19] increase packing density and reduces the number of voids due to the knocking off of overhanging atoms. The ejection of impurities in the growing film is also a reality due to their poor bonding properties. A full description of ion and electron bombardment of films is given later in the section on thin film growth.

3.3.1.6 Reactive Sputter Deposition

This sputtering technique is difficult due to large possible variations in the process from one deposition to another. The technique may be used in DC or RF modes. The idea is that of sputtering a

material to form a compound with a reactive gas present in the chamber along with the sputter gas. Compounds such as TiN, AlN and TaN are formed from sputtering the metal target in argon and nitrogen environments. Oxygen can also be incorporated to form oxides of metals (TiO_2). Ideally, one would like for the reaction to take place at the substrate, but this is not always the case. More often, the compound forms at the target due to reactions with the ionized reactant species in the plasma. Argon is then used to sputter the compound from the target. If the compound is an insulator on the target surface, then RF or magnetron configurations must be used. Reaction in the gas phase can lead to a powder type film, which is brittle due to very large nucleation and growth molecules.

The concentration of reactant gas is an important factor and can be determined by[26]

$$k\frac{N_g}{N_c} > 1$$ reaction at the cathode Eqn 3.18

and

$$k\frac{N_g}{N_s} > 1$$ reaction at the substrate Eqn 3.19

N_g denotes the number of reactive gas molecules that strike unit area of the cathode surface or the substrate per unit time. N_c, is the number of sputtered atoms from unit area of the cathode per unit time and N_s, is the number of deposited atoms per unit area of the substrate per unit time.

Compound Targets

An alternative way of depositing a compound alloy film is by using a compound target. The composition of the sputtered film is controlled by the surface area representation of the constituents. The sputter yield of each element should be taken into account when fabricating the target. The target must also be sufficiently cooled in order to prevent the diffusion of constituents. Possible compound target configurations are shown in figure 3.15 below.

Substrate holders are usually rotated to ensure a uniform deposition.

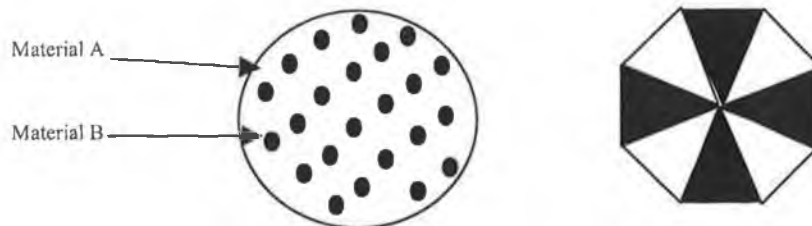

Figure 3.15[26] Representations of different types of compound targets.

3.3.1.7 Ion Beam Sputtering

Ion beam sputtering developed by Chopra and Randlett[15], is a technique that uses a cathode filament to generate an ion beam. This ion beam is generated in a differentially pumped chamber from the target and substrate. The main advantage is that the growing film and substrate are not subjected to plasma bombardment. Additionally, the incident ion beam energy reaching the target can be controlled by adjusting the current flowing to the filament or by employing energy retardation grids before the beam enters the main chamber. The incident angle of the beam upon the target material can also be varied in order to maximize sputter yield for different target materials.

Ion beam currents can range from 10mA to several Amps and the ion energy can be from 500eV to 2.5keV[15]. The chamber pressure is typically operated in the low 0.1 Pa range.

The properties of ion beam sputtered films include superior adhesion and denser film structure which both can be attributed to the higher energy of the sputtered particles. Optical film properties have also been found[15] to be superior to the more conventional electron beam evaporated films of the same materials.

Ion sources used for the generation of the ion beams are vast, including the establishment of a glow discharge, referred to as a Penning source. More recently, the use of Kaufmann type ion sources is preferred due to the high and controllable current densities possible. Figure 3.16 shows a typical configuration of an ion beam sputtering system.

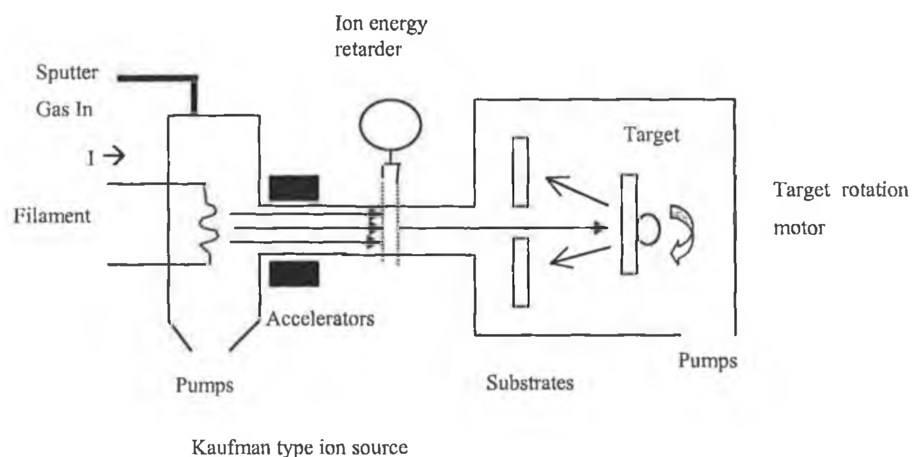

Figure 3.16 Illustration of an ion beam sputtering system with a Kaufmann type ion source.

Reactive ion beam deposition is also possible by using a reactant gas to form a compound target, such as TiN. The ion beam will then sputter TiN from the target and deposit onto a substrate.

3.3.1.8 Microwave ECR Sputtering

As with plasma chemical vapour deposition, sputtering can also be carried out at microwave frequencies with an ECR microwave based plasma. This process is also suitable for reactive sputtering and for etching of substrates. The design is the same i.e a 2.45GHz source is used to generate a confined plasma. The plasma is magnetically guided to the substrate and bombards a target in transit. The ejected film is then deposited on the substrate. Figure 3.17 illustrates the idea.
The ECR condition is given by the formula[26]

$$f = \frac{1}{2\pi}\frac{eB}{m} \qquad \text{Eqn 3.20}$$

where f denotes the frequency of the electric field, B the magnetic field strength and, e and m are the electrons charge and mass respectively.

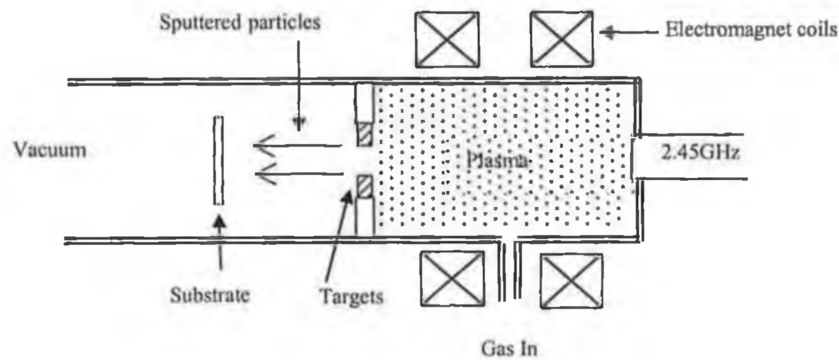

Figure 3.17[26] **Illustration of ECR plasma sputtering system.**

3.4 Thin Film Growth

This section of the chapter will be purposely aimed at an explanation of sputter film growth, but can be generalized to all film deposition processes.

One important aspect of thin films not yet addressed is the film growth process on a substrate. In order to understand the properties and characteristics of thin films it is important to understand the growth sequence of films, and to then understand the parameters that effect growth. Any of the thin film deposition processes in table 3.13 involves three main steps to form a film on a substrate. These steps can be listed as

1. production of the appropriate species.
2. transportation of these species to the substrate via a medium.
3. condensation on the substrate, either directly or through a chemical reaction to form a solid deposit.

The formation of a film takes place via an initial nucleation step and then a growth process. The following step-by-step approach[27] gives an overall view into the stages of growth:

1. The species lose their velocity component normal to the substrate upon impact and are physically adsorbed by the substrate surface.
2. Initially, the adsorbed species are not in thermal equilibrium with the substrate and diffuse about the substrate surface until they find a nucleation site. Bigger clusters or nuclei will form due to this thermal imbalance.
3. These nuclei are thermodynamically unstable and may tend to break up in time depending on deposition parameters. A nucleus may become thermodynamically stable if it overcomes the nucleation size barrier by colliding with other nuclei (coalescence), thus growing in size. This step involving the formation of stable, chemisorbed, critical-sized nuclei is called the nucleation stage.
4. The critical nuclei grow in number as well as in size until a saturation density is reached. The nucleation density and the average nucleus size depend on a number of parameters such as the energy of the impinging species, the rate of impingement, the activation energies of adsorption, desorption, thermal diffusion, temperature, topography, and chemical nature of the substrate. Nuclei growth can occur either parallel to the substrate by surface diffusion or can grow perpendicular to the substrate by direct impingement of the species. In general, however, the rate of lateral growth at this stage is much higher than that of perpendicular growth. The grown nuclei are called islands.
5. The next stage in the process of film formation is the coalescence stage, in which small islands start coalescing with each other. The tendency to form bigger islands is termed agglomeration and can be enhanced by increasing the surface mobility of the species. These mobility increases can be brought about by sufficiently increasing the temperature of the substrate.

6. Larger islands grow together, leaving channels and holes of uncovered substrate. The film structure changes from discontinuous island type to a porous network type as the large islands meet. The filling of these channels and holes forms a completely continuous film.

These steps are schematically represented by figure 3.18. This shows the basic elements of film growth in four stages. Figure 3.19 is a representation of the substrate during nucleation and grain growth.

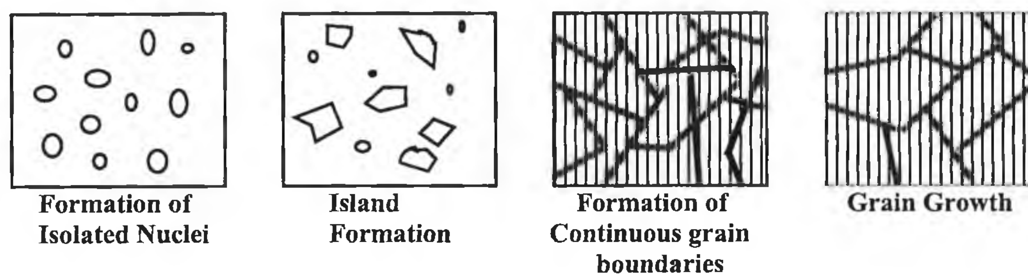

Figure 3.18 Four stages of film growth

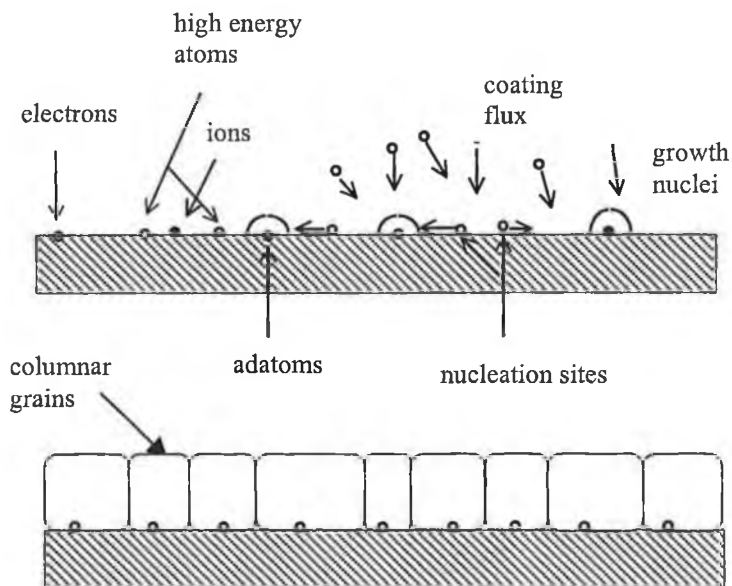

Figure 3.19 Substrate during site generation, nucleation and grain growth

Initial growth of the film is primarily dependent upon the relative values of the adatom-adatom and adatom-substrate (cohesive and adhesive) interaction energies. Three classifiable growth modes exist. Island (or Volmer-Weber) growth is characterized by nucleation and growth of adatom islands on the substrate surface. This occurs when the cohesive energy exceeds the adhesive energy. Islands become stable only after reaching a critical size. Layer (or Frank-van der Merve) growth occurs when the adhesive energy is greater than the cohesive energy so that the initial atoms form a complete monolayer before

forming a second layer and so on. Intermediate layer-plus-island (or Stransky-Krastanov) growth is when island growth dominates after a few mono-layers. The growth mode depends upon the thermodynamic parameters of the deposition and the substrate surface parameters. The nucleation site density is dependent on the kinetic energy and surface mobility of the adatoms[32].

Sometimes in order to promote nucleation, impurity particles are introduced[37]. This process is called grain refinement or inoculation. For example, a combination of 0.03% titanium and 0.01% boron is often added to aluminum alloys. Tiny particles of Al_3Ti or TiB_2 form and serve as sites for nucleation. Grain refining produces a large number of grains, each beginning to grow from one nucleus. The greater the grain boundary surface area the larger the grain size strengthening in metals.

It is important to realize that the film microstructure is determined by the variables that control the film nucleation and growth, such as

- Substrate-film interaction
- Deposition temperature
- Deposition rate
- Temperature of the subsequent processes
- Base pressure

In turn it is the film structure, and so these variables, that determine many of the characteristics and properties of the film such as:

- Resistivity
- Reactivity
- Electromigration resistance
- Stress

The different characteristics of thin films will be examined in the next section with respect to the variables involved in determining their eventual outcome.

3.4.1 Film Bombardment

Particle bombardment of substrates has both preferable and undesirable effects. To the extent of which are good and bad depends upon two things, firstly the application of the film being deposited and secondly, on the substrate to which the film is being deposited. Here, a review of energetic particle bombardment of substrates during deposition and its consequences to the film characteristics will be reviewed.

3.4.1.1 Ion and Electron bombardment of substrates

Energetic particles collide with the growing film and thus give up momentum, energy and charge in the case of ions. The flux of ions and electrons that are incident on the surface depends on whether it is biased as a cathode, anode or is electrically neutral and also is directly dependent on the deposition process used. The impact of these species can cause numerous affects, most notable of which are

- Increase in adatom mobility
- Improving stable nucleation site density[32]
- Enhanced adhesion[32,33]
- Modification of the crystal structure[32,34]
- Sputtering from and possibly redeposition back onto the growing film
- Preferential erosion of roughness peaks[35]
- Substrate heating
- Surface ejection in the process of sputter cleaning
- Promotion of chemical reactions and diffusion[32]

As a direct result of these influences changes in grain size[11,27,32], film stress[32,36], film density[32,35], number of voids[35], surface and bulk morphology[32] and the degree or direction of crystal orientation[32] can be observed depending on the extent of ion energy and momentum transferred to the growing film.

Ion bombardment during the initial stages of growth[27] can directly effect the nucleation process due to the break up upon impact of nuclei smaller than the thermodynamically stable critical size. This same bombardment energy also promotes large island generation through adatom mobility increases. The effect of ion energy on nucleation size and density can be graphically represented by figure 3.20. The relationships are represented as linear functions for illustrative purposes only.

As is illustrated in the graph, the greater the energy of the bombarding ions the less probable unstable nuclei will exist due to energetic breakup upon collision. In turn, larger more stable nuclei grow

faster due to increased adatom mobility and due to reduced density of nucleation sites. The packing density of films during growth also increases with ion energy due to the ejection of loosely bound surface and overhanging atoms.

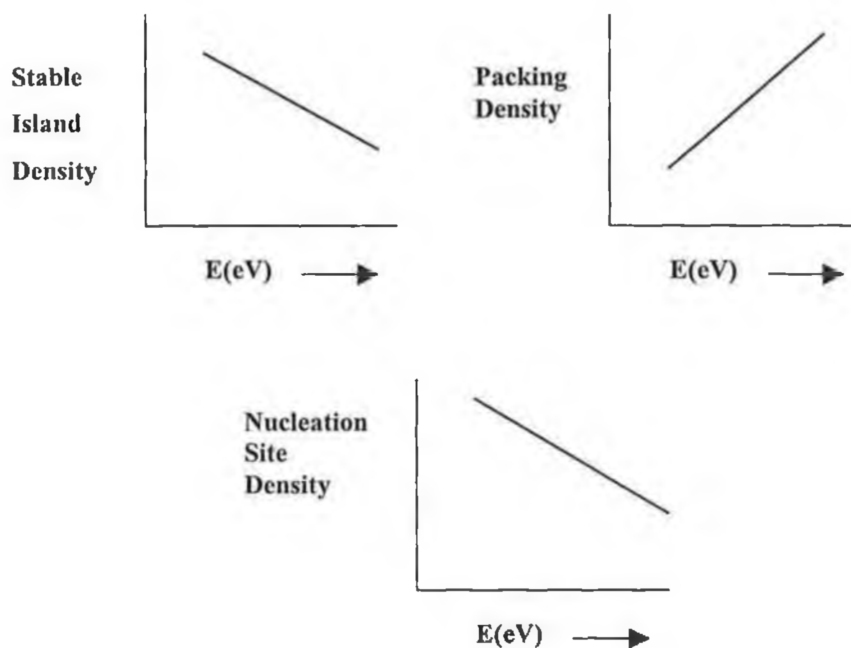

Figure 3.20 Graphical representation of the relationship between bombarding ion energy, nucleation site density, stable island density and packing density.

While examining the effects of ion bombardment on vapour phase growth, Muller[35] found that for film growth during sputtering applications:

1. Ion bombardment during film growth removed overhanging atoms and thus reduced the probability of void generation and increased packing density.
2. Increased vapour to incident ion flux ratios result in increased packing density.
3. Sputtered atoms are mainly deposited in voids.
4. Ions induce surface diffusion, local heating, collapsing of voids and re-crystallization.

These effects can be illustrated as in figure 3.21 below.

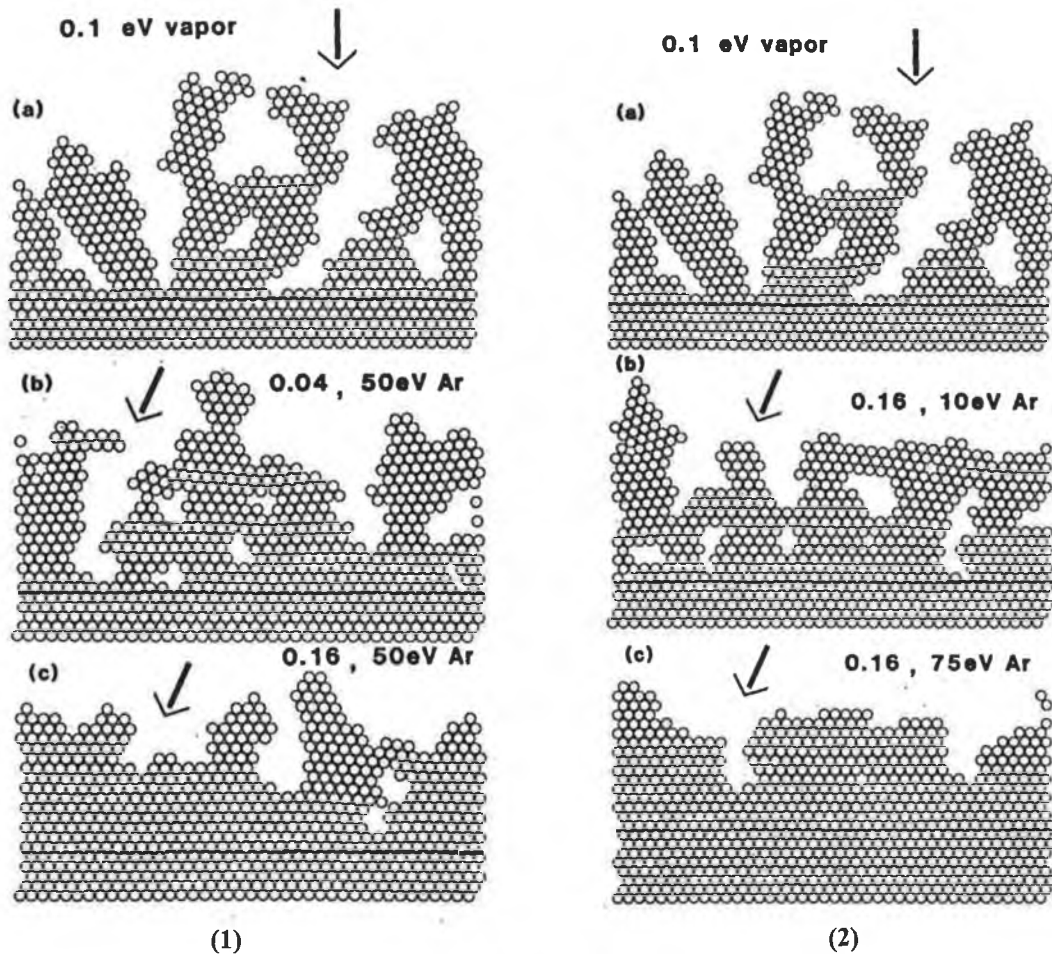

Figure 3.21[35] (1) Typical microstructure for condensing vapour arriving under normal incidence (a) without ion bombardment, (b) with Ar ion bombardment of 50 eV and an ion to vapour flux ratio of 0.04, (c) ratio of ion to vapour flux increased to 0.16.
And (2) a typical microstructure for condensing vapour arriving under normal incidence (a) without ion bombardment (b) with Ar ion bombardment of 10 eV and (c) Ar energy at 75 eV. Ratio of ion to vapour flux is constant at 0.16.

The momentum exchange associated with this ion bombardment can cause the rearrangement and ejection of surface atoms. This rearrangement can have dramatic effects on the properties and characteristics of these films, as highlighted by Mattox[32] and is of importance in the processes of ion plating, bias sputtering and unbalanced magnetron sputtering[38]. The ejection of species due to momentum exchanges is an important factor in the process of sputter cleaning of substrates prior to deposition.

The effects of electron bombardment are usually seen as induced floating voltage or uncontrolled heating of substrates. In PECVD applications the substrates are usually raised to a floating potential V_f, this potential arises due to higher electron mobility than ion mobility as discussed in chapter two. It can be shown that the floating potential is related to the electron temperature through the expression[29]

$$V_f = -\left(\frac{1}{2e}\right) kT_e \ln\left(\frac{\pi m}{2M}\right) \qquad \text{Eqn 3.21}$$

where T_e is the electron temperature, m the mass of the electron, M the ion mass, e is the electron charge and k is Boltzmann's constant

Electron bombardment of atoms and molecules deposited on substrates also produces excitation and ionization to a similar, but much lesser extent than in the gas phase. Electron bombardment can cause dissociation or bond rearrangement due to atoms on the substrate being elevated to excited states. This can lead to desorption from the substrate or emission of energy in the form of photons.

3.4.1.2 Neutral bombardment of the substrate

In PVD applications high-energy or fast neutral sputter gas atoms, can retain significant energy after having struck the cathode as ions. These ions become neutralized, then recoil with significant energy and impinge upon the substrate causing material to be sputtered from the growing film. The process is termed Intrinsic Sputtering and their numbers are typically 8% of the discharge current for a 1 KeV discharge[43], but are dependent upon cathode material and gas atomic number. Some neutrals may embed themselves in the growing film or substrate in a process termed implantation[32]. The momentum transferred in collisions can also improve the packing density by collapsing voids and inducing surface diffusion[35].

Sputtered target atoms can also retain significant energies upon arrival at the growing film (up to 40eV for a 400mA discharge at a 6cm source-substrate distance[39]) though most are partially thermalized by collisions in the gas phase. The effects of these high energy sputtered[35,40] atoms are again to modify film properties as described above.

3.5 Thin Film Properties

The following section will look at the fundamental properties and characteristics of thin films such as microstructure, adhesion and stress. It will also review the parameters that effect and determine the relative values of these properties.

3.5.1 Microstructure

The formation of the microstructure is heavily dependent on the deposition temperature and, as a consequence, the surface mobility of the absorbed species. An increase in temperature will promote increased surface mobility, which leads to a larger more well-defined grain size. Any variable that results in an increase of bombarding ion kinetic energy, such as voltage, will have a similar effect. However, at sufficiently high kinetic energies the surface mobility is reduced due to implantation of the species in substrate. This results in a reduced grain size[27]. This can be easily illustrated by figure 3.22 along with the relationship between grain size and substrate temperature. Both these graphs are related, as kinetic energy is a function of temperature. There is a maximum kinetic energy (k_{max}) or substrate temperature (T_s) to which the growth can be exposed before the advantages and size of large grains are reduced. Grain growth does not continue indefinitely. Under a given set of deposition conditions the grain size increases with thickness until a certain thickness is reached, at which point, grain size remains constant. Fresh grains are nucleated on top of the old ones above this thickness.

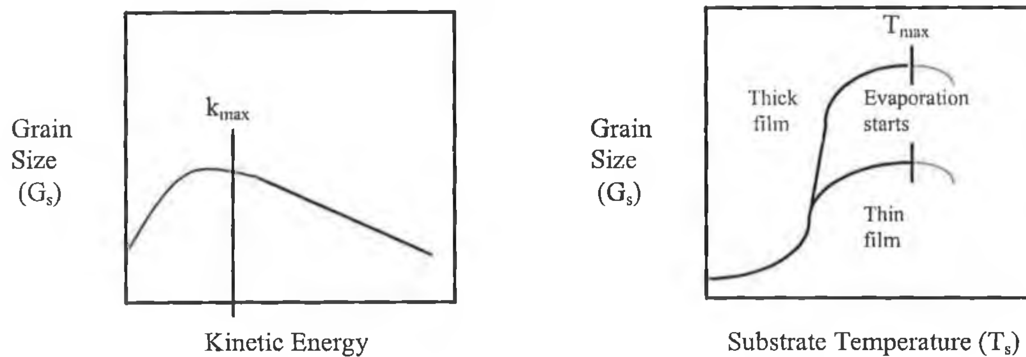

Figure 3.22[27] Influences of (a) kinetic energy and (b) substrate temperature on grain size for a growing film.

Movchan and Demchischin[28] first examined the influences of temperature on film growth in 1969. This was based on results obtained from thick film coatings of Ti, Ni, W, ZrO_2, and Al_2O_3. Their results produced a zone model that provided a qualitative understanding of the coating structure. Their model highlights the importance of adatom mobility in determining film structure. It uses the temperature of the

film during deposition normalized to its bulk melting point (T/T_m) as the parameter describing thermally induced mobility. The diagram is illustrated in figure 3.23 and shows three structural zones.

In zone 1 where T/Tm <0.3 the grains are tapered with dome like ends. These grains have voided boundaries and so electrical resistivity is increased due to oxidation in the voids. The film is mechanically strong but laterally weak. Zone 2 (0.3 < T/Tm <0.5) has columnar grains with well defined grain boundaries. Grain diameter increases with temperature as it does through the three zones. Zone 3 (T/Tm < 1) has an equiaxed grain structure due to bulk diffusion.

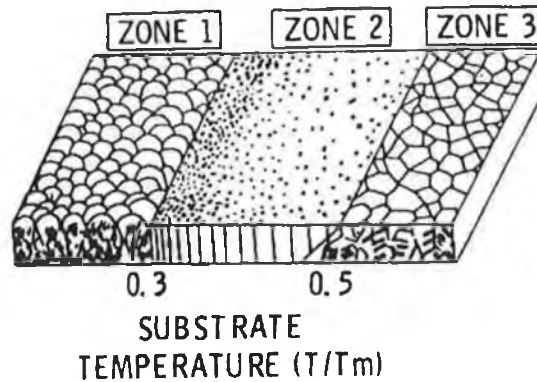

Figure 3.23[28] Structural Zone Model for coating growth proposed by Movchan and Demchischin

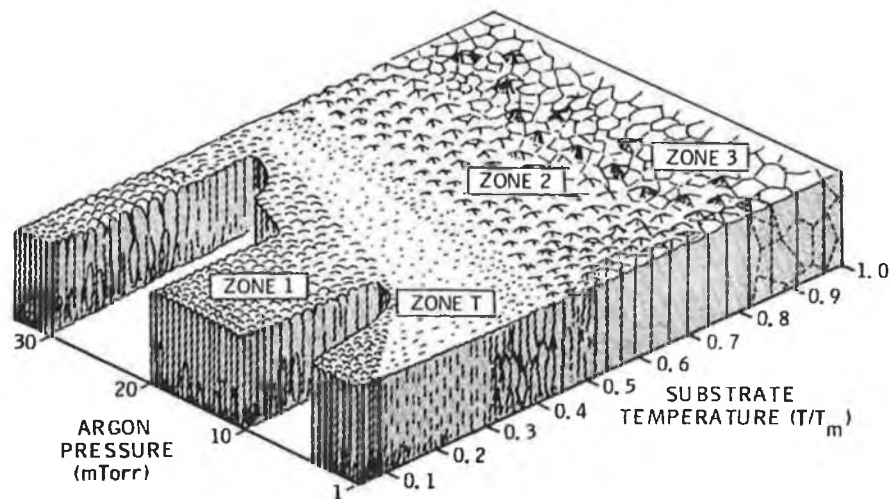

Figure 3.24[29,31] Influence of substrate temperature and argon pressure on the microstructure of a thin film.

The combined influences of pressure, temperature and substrate surface roughness on film microstructure

were considered by Thornton[31] in 1974 as an extension to the zone model proposed by Movchan and Demchischin. This article claimed that higher inert gas pressures are thought to limit the mobility of adatoms upon the substrate surface. Inert gas atoms are themselves absorbed and hence limit the diffusion of the arriving species. As we have seen increased temperature, on the other hand, promotes surface mobility and also conventional bulk diffusion. Thornton's model is schematically represented in figure 3.24. The zone formation process is summarized below:

Zone 1 : Protuberances on the absorbing surface preferentially collect incident atoms which, due to low substrate temperature, do not have sufficient thermal energy to diffuse away from a continuous structure. Film growth tends to be porous or have open grain boundaries.

Zone T : The temperature is still too low to permit diffusion at significant rates, but the surface smoothness has improved greatly as enough diffusion has occurred to overcome the main surface irregularities. The grain structure is fine and densely packed. It can be seen from the model that at low temperatures, an increase in the inert gas pressure induces the growth of a more porous grain structure due to effects on surface mobility caused by this increase in pressure.

Zone 2 : This zone is dominated by surface diffusion processes. The grain structures are columnar with fully dense boundaries.

Zone 3 : The high temperature here produces substantial bulk diffusion, therefore re-crystallization and grain growth may occur in this regime.

Defects called hillocks may be formed in the film due to changes in the substrate temperature during deposition. These features result from differences in the coefficients of thermal expansion between the substrate and the deposited film. They consist of small projections normal to the film surface, or in the case of 'negative' hillocks, holes.

3.5.2 Adhesion

The adhesion of a film to a substrate is of the utmost importance, as it will impact many electrical and mechanical characteristics. It is dependent on many factors such as chemical nature, cleanliness and the microscopic topography of the substrate surface. It can be defined as the sum of all the inter-molecular interactions between two different materials. These inter-molecular interactions[11] may be metallic ionic, covalent or Van der Waals and are a direct function of the separation of the adhering surfaces.

Generally, it can be said that the adhesion of a film to a substrate increases for higher values of

- Kinetic energy of the incident species[32,33] (higher deposition temperature, discharge voltage, etc..)
- Adsorption energy of the deposit
- Initial nucleation density (function of surface quality).

Adhesion is generally promoted by energetic particle bombardment of the substrate prior to and during the initial stages of film formation[32].

Substrate roughness is an important factor for adhesion. The rougher the surface the larger the total surface area of the substrate. This increase in surface area promotes good adhesion. However, excessive roughness can result in coating defects that can cause adhesion failure or cracking.

Hillocks, as described in the last section, can be formed due to residual stresses within the deposited film. These hillocks are clear results of poor adhesion and can manifest themselves as severe cracking of the deposited film.

In applications where the substrate and thin film are not fully adhesive, such as tungsten on silicon oxide in VLSI manufacturing, a thin (350 Å) adhesion layer of TiN can be used. This adhesion layer acts as a glue layer for the tungsten and has no problems adhering to the silicon oxide. The layer also prevents junction arcing due to its insulation characteristics.

3.5.3 Stress

The total stress of a film can be attributed to two main causes, intrinsic and extrinsic stress. The basic differences between these two can be viewed as follows:

- Intrinsic stress is due to the deposition conditions and resulting microstructure,
  - temperature
  - pressure
- Intrinsic stress is also dependent on target material.

- Extrinsic stress is imposed upon the film by an underlying or overlying film or substrate.
  - this stress is due to differences in the coefficients of thermal expansion between the various materials.

Thermal or extrinsic stress origins are easily understood as differences in the thermal properties between film and substrate. The strain introduced in the film can be mathematically defined[30] as

$$\varepsilon_{film} = \int_{T_0}^{T_1} \left(\alpha_{film} - \alpha_{sub}\right) dt \qquad \text{Eqn 3.21}$$

where α_{film} and α_{sub} are the linear-expansion coefficients of the film and substrate. T_1 and T_0 illustrate the change in temperature of the film on the substrate.

At high temperatures this can be approximated to equation 3.22 over limited temperature ranges.

$$\varepsilon_{film} = \left(\alpha_{film} - \alpha_{sub}\right)\Delta T \qquad \text{Eqn 3.22}$$

Alternatively, the stress of a deposited film on a disc can be measured directly by measuring the change in wafer curvature and using the following expression[30]:

$$\sigma_{film} = -\frac{E_{sub}}{6\left(1 - \nu_{sub}\right)} \frac{t_{sub}^2}{t_{film}} \left(\frac{1}{R} - \frac{1}{R_o}\right) \qquad \text{Eqn 3.23}$$

where σ_{film} is the stress in the thin film, E_{sub} and ν_{sub} are the modulus of elasticity and Poisson's ratio for the substrate respectively, t_{sub} and t_{film} are the substrate and film thickness, R_0 is the initial radius of curvature before film deposition, and R is the measured radius of curvature.

The stress formed during the deposition process can lead to the formation of hillocks in the film. By using adhesion promotion techniques prior to and during deposition stress levels in films may be reduced.[32]

Intrinsic or initial stress on the other hand is more difficult to understand due to the number of possible causes, which include:

- Lattice mismatch[32] between the film and the substrate during coalescing of islands at the initial stage of nucleation.
- Deposition rate[32].
- Thickness[32].
- Impurities.
- Gas pressure[41]
- Target atoms having a penning effect on the film[41], in that, after the initial monolayer is deposited incident atoms act like wedges and hammer the film producing compressive stress.
- Ratio of bombarding species to deposition species[42].

Highly stressed films are generally more likely to corrode and exhibit poor adhesion to the substrate. Film stress can be compressive, so that it attempts to expand in parallel with the substrate, and in extreme cases can cause the film to buckle. Tensile stress is where the film applies a force upwards or away from the substrate and in extreme cases can cause the film to break up. Tensile stress will cause the film to be convex whereas compressive stress will cause the film to be concave.

Chapter Three References:

[1] D. Martell, Palo Alto, California. Reuters News, www.reuters.com, Jan (1999).

[2] K.K.Schuegraf, Handbook of Thin Film Deposition Processes and Techniques, Noyes Publications, New Jersey (1988) p4.

[3] Semiconductor International, Jan (1995) p47.

[4] Basic PVD Process, Applied Materials Technical Training (1997).

[5] S. Wilson, C Tracy, and J. Freeman, Handbook of Multilevel Metallization for Integrated Circiuts, Noyes Publications, New Jersey (1993) Chapter 1.

[6] Confidential correspondence, Applied Materials (1998).

[7] D. Askeland, The Science and Engineering of Materials, Chapman & Hall, London (1989) Chapter 6.

[8] B.J. Janoss, Forming and Fabrication, Oct (1997).

[9] D. Monaghan, D. Teer, K Laing, P. Teer, and P. A. Logan, Surface Technology International, June (1994).

[10] R.S. Bonetti and O.F. Happel, 'Protective coatings by CVD in an industrial scale', Switz (1996).

[11] M. Murphy, Planar Magnetron Sputtering Technology, PhD Thesis , DCU (1996).

[12] M. Meyer and R. Bonetti, 'CVD and plasma protective coatings for machine parts', Switz (1995).

[13] K. Zweibel, Progress in Photovoltaics, Vol 3. No. 5 Sept/Oct (1995).

[15] D.A.Glocker and S.I.Shah, Handbook of Thin Film Process Technology, Institute of Physics Publishing, Bristol (1995).

[16] A. Sherman, Chemical Vapour Deposition for Microelectronics,Noyes Publications, New Jersey (1987) Chapter 2.

[17] B. Chapman, Glow Discharge Processes, Wiley, New York (1980) Chapter 3.

[18] K.K.Schuegraf, Handbook of Thin Film Deposition Processes and Techniques, Noyes Publications, New Jersey (1988) p112 - 150

[19] K.H. Muller, Physical Review B, Vol. 35, no. 15 (1987) 7906.

[20] D. Hinson and H Seigerman, The Thin Film Book of Basics, Materials Research Corporation NewYork (1983).

[21] B. Chapman, Glow Discharge Processes, Wiley, New York (1980) Chapter 2.

[22] B. Chapman, Glow Discharge Processes, Wiley, New York (1980) Appendix 6.

[23] J. Vossen and W. Kern, Thin Film Processes, Academic Press, New York (1978) p15-18.

[24] K. Wasa and S.Hayakawa, Handbook of Sputter Deposition Technology, Noyes Publications, New Jersey (1992) p50 to 60.

[25] K. Wasa and S.Hayakawa, Handbook of Sputter Deposition Technology, Noyes Publications, New Jersey (1992) p97 to 110.

[26] K. Wasa and S.Hayakawa, Handbook of Sputter Deposition Technology, Noyes Publications, New Jersey (1992) p107 - 150.

[27] K. Wasa and S.Hayakawa, Handbook of Sputter Deposition Technology, Noyes Publications, New Jersey (1992) Chapter 2.

[28] B. Movchan and A. Demchischin, Phys. Metal. Metallog. 28 (1969) 83.

[29] J. Vossen and W. Kern, Thin Film Processes, Academic press, New York (1978) Chapter II-2.

[30] D. Gardner and P. Flinn, Mechanical Stress as a Function of Temperature in Al Films, IEEE Transactions on Electron Devices, vol.35 (12) (1988).

[31] J.A. Thorntan, J. Vac. Sci. Technol. 11 (1974) 666.

[32] D.M. Mattox, J. Vac. Sci. Technol. A7(3) (1989) 1105.

[33] J.Griffith, Y. Oiu, and T. Tombrello, Nucl. Instrum. Methods 198, (1982) 607.

[34] D. Dobrev, Thin Solid Films, 92 (1982) 41.

[35] K.H. Muller, Physical Review B, Vol. 35, no. 15 (1987) 7906.

[36] J. Cuomo, J.M.Harper, C.R. Guarnieri, D.S. Yee, L.J. Attanasio, J.Angilello, C.T. Wu, and R.H. Hammond, J. Vac. Sci. Technol. 20 (1982) 349.

[37] D.A. Askeland, The Science and Engineering of Materials, Chapman & Hall, London (1996).

[38] W.D. Sproul, Materials Science and Engineering, vol. A163, no.2 (1993) 187.

[39] S. Kadlec, C. Quaeyhaegens, G. Knuyt, and L. Stals, Surf. Coat. Technol. 89 (1997) p177 – 184.

[40] J.A.Thorntan and D. W. Hoffman, J. Vac. Sci. Technol. A 3 (1985) 576.

[41] R. Cuthrell, D. Mattox, C. Reeples, P. Dreike, and K. Lamppa, J. Vac. Sci. Technol. A6 (1988) 2914.

[42] D.W. Hoffmann and M. Gaerttner, J. Vac. Sci. Technol. 17 (1980) 425.

[43] D.W. Hoffman, J. Vac. Sci. Technol. A 8 (5) (1990).

Chapter Four

Magnetron Sputtering Technology

4.1 Introduction & Applications

Magnetron sputtering has evolved as one of the most intensively researched areas of thin film deposition. First studied by Penning in 1935, magnetron sputtering has become increasingly important in the fields of semi-conductor, opto-electronics, decorative and wear resistive coatings.

The idea that Penning had studied was that of a low-pressure discharge subjected to a transverse magnetic field. He found that the induced magnetic field lowered the sputter gas pressure by a factor of ten, and increased the deposition rate of the deposited films. Initially the device was used for the sputtering of copper, nickel and silver targets.

From Penning's designs, others recognized the attraction of the magnetron process but it failed to be developed significantly during the 1940s and 1950s. In the 1960s more advanced and efficient methods were developed for inducing magnetic fields on sputter processes. Hayakawa and Wasa invented the original planar magnetron system[1] by using a solenoid coil, however, areas of application were not yet developed for their technique. By the start of the 1970s, three distinct types of magnetrons had been developed[2], conical magnetrons, cylindrical magnetrons and planar magnetrons.

During the birth of large scale manufacturing of silicon based integrated circuits, magnetron sputtering had been recognized as a critical process, and was put into large scale manufacturing use in the 1970s, along with other thin film deposition processes.

Today magnetron sputtering, in all its variants, plays a large role in the manufacturing of a many products. Increasingly, the role of unbalanced magnetron sputtering has been developed[9,12-16] by workers in many countries as the distinct advantages of films deposited using this method have been realized.

4.2 Magnetron Sputtering

One of the downfalls of conventional sputtering is that deposition rates are low, typically 50nm/min. The main contributor to this low deposition rate is the loss of secondary electrons emitted from the target to the anode or surrounding walls. Since most electrons pass through the discharge without creating ions, the ion bombardment and sputter rate of the target is much lower than if these secondary electrons were involved in ionization processes.

These electrons can be harnessed in a processed called 'magnetron sputtering'. The idea behind this technique is the capture of secondary electrons emitted form the target by means of a magnetic field running parallel with the target surface. This field capture can be illustrated in figure 4.1.

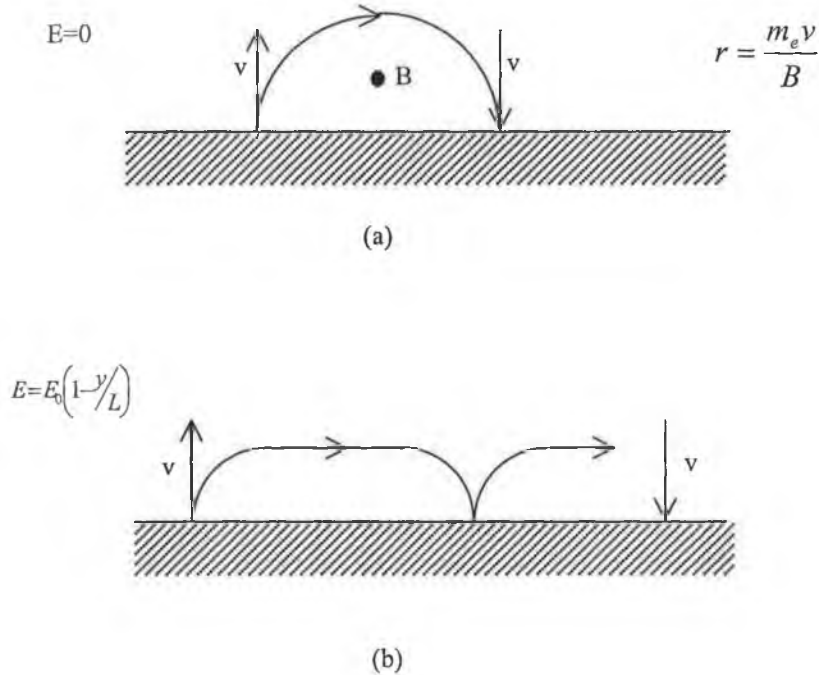

Figure 4.1 Illustration[3,4] of (a) the motion of an electron captured by a B field (with E=0) running parallel to the surface (out of the page) and (b) motion on an electron ejected from the surface with velocity, *v*, into a region of magnetic field, B, with electric field E. (E_0 is the field at the tart surface, *y* is the distance from the target surface, *L* the thickness of the dark space, *r* the radius of the electron motion, *v* the velocity and m_e the electron mass).

If the motion of the charged particle is considered in figure 4.1 (a), where q is charge, m is mass, and v_0 the initial velocity, and E=0, then the charge experiences a force due to the magnetic field given by

$$F_m = qvB \qquad \text{Eqn 4.1}$$

If no other forces are exerted on that particle, then the magnetic force, F_m, will induce a circular motion with a radius

$$r_g = \frac{(mv)}{qB} \qquad \text{Eqn 4.2}$$

This r_g, the gyration radius, is applied to both ions and electrons. It can be expressed in both terms of energy, E, of the particles and in magnetic field, B. This becomes

$$r_{g,e} = 3.37x\left[\frac{E^{1/2}}{B}\right]$$ for an electron

$$r_{g,i} = 9.11x10^{12}\left[\frac{E^{1/2}}{B}\right]$$ for an ion (Ar^+)

where E is measured in electron volts and B in Gauss

If B is uniform, which is assumed, and E=0, the electrons drift along the field lines with a speed, $v_{||}$, which is unaffected by the magnetic field, and orbit the field lines with gyro frequency[4]

$$\omega_e = \frac{eB}{m_e} = 1.76x10B\, rad/\sec$$ Eqn 4.3

The difference between the gyration radius equations shows that ions have a radius movement about 300 times greater than that of electrons. Due to the size of this radius, it can be approximated that ions travel in straight lines relative to electron motions near the cathode. It can also be said that the movement of electrons is heavily influenced by the presence of a magnetic field

If the motion of an ejected electron (figure4.1 (b)) is now considered, then the electric field perpendicular to the target surface and the magnetic field parallel to the surface must be taken in to account. It is assumed that the initial velocity is zero for the emitted electron and that the magnitude of the electric field is given by

$$E = E_0\left(1 - \frac{y}{L}\right)$$ Eqn 4.4

where E_o is the magnitude at the target surface, L , the length of the cathode dark space, and y, a vertical distance above the target.

The electron is emitted from the target and is accelerated by the electric field, E. It is also subjected to a simultaneous magnetic force, F_m. Assuming that the force induced by the magnetic field is strong enough, the perpendicular direction of the electrons velocity is altered and the trajectory becomes cycloidal (figure 4.2b). Once the electron is on its return path to the target it is decelerated by the electric field and again reaches zero velocity until the process repeats and the electron is again ejected from the surface by the electric field. The distance that the electron is emitted from the target is given by

$$y_{\max} = \frac{1}{B}\left[\frac{2m}{e}(V - V_T)\right]^{1/2} \qquad \text{Eqn 4.5}$$

where V_T is the negative target voltage and V is the potential in the dark space at y_{max}. B is measured in Gauss and m and e are the mass and charge of the electron respectively.

The net result of this electron hopping due to magnetic and electrical fields is that ionization increases near the target surface due to enhanced electron-atom collisions with the sputter gas. Experimental modeling results[5] have shown that for a transversal magnetic field of 250G, at a pressure of 1 Pa, trapped electrons of average energy produce about 14 ions before escaping from the magnetic trap.
This increased electron ionization probability allows for operation at lower process pressures that in turn increases the probability of an atom reaching the substrate. The magnitude of the electron velocity parallel to the target surface is called the magnetron drift velocity, or the ExB drift velocity and is expressed[4] in cm/sec as

$$V_D = \frac{10^8 E_{\perp}\left(\frac{volts}{cm}\right)}{|B|(gauss)} \qquad \text{Eqn 4.6}$$

where E is the perpendicular component of the electrical field and B the magnetic field strength.

Figure 4.2 shows hopping motion of drift electrons and the spiraling motion of discharge electrons.

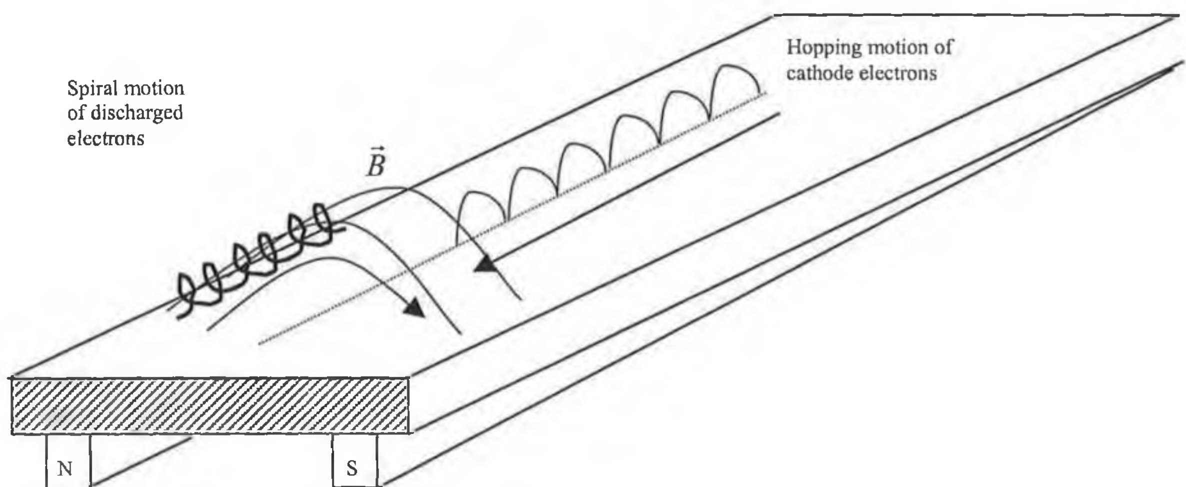

Figure 4.2 Electron motions influenced by a magnetic field at the target surface

Plasmas that are enhanced by secondary electron capture, or magnetron plasmas, are very efficient but are non-uniform plasmas as the enhancement is confined to the electron drift path. This results in enhanced sputtering, but only along a racetrack area of the target. This racetrack shape is governed by the magnetic field shape and results in inefficient use of the target surface area.

4.3 Planar Magnetron Sputtering

There are two types of planar magnetron sputtering processes, DC planar magnetron and RF planar magnetron sputtering. Both of these processes are configured the same as their non-magnetron namesakes, the main difference being the introduction of electron traps usually in the form of magnetrons placed behind the cathode or target. The main reasons for the development of these processes were to (1) increase the deposition rate of the non magnetron processes, (2) to reduce the exposure of the device being coated to ion and electron bombardment, and (3) to reduce unnecessary substrate heating as the plasma is concentrated and confined mostly to the cathode. The attraction of being able to scale up the process to coat large objects was also an advantage and has supplemented electron beam evaporation techniques for many modern applications.

4.3.1 DC Planar Magnetron Sputtering

The system configuration is uncomplicated. A target is held at a negative potential with the anode placed parallel to it and is can be biased or grounded. A magnetron in the form of (a) or (b) in figure 4.3 can be used depending on the target and chamber geometry.

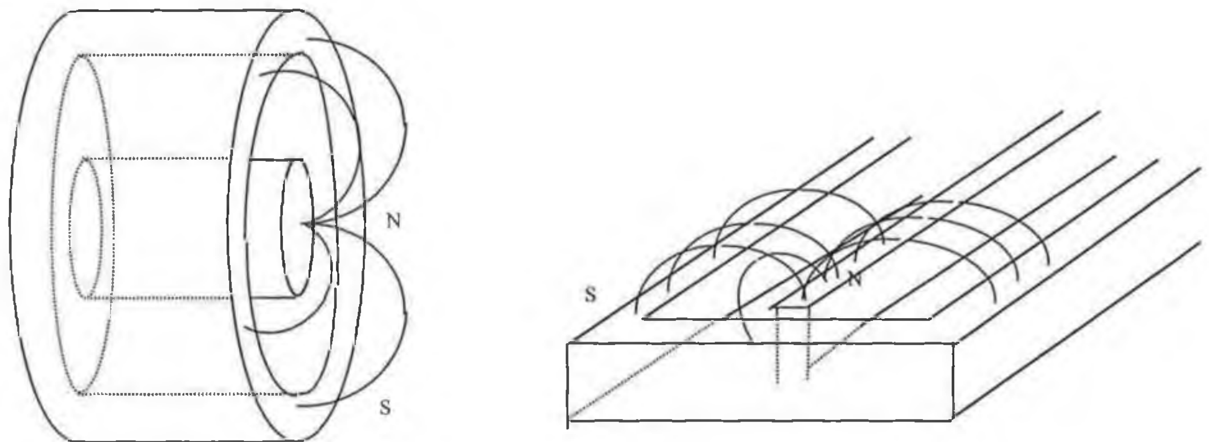

Figure 4.3 Illustrations of typical (a) planar circular magnetron and (b) planar rectangular magnetron designs.

The magnetron is placed behind the cathode to ensure that the magnetic field lines encompass the target area. The magnets should be placed close to the target so the field lines intersect normal to the target surface. This feature helps ensure an efficient electron trap. The parallel component of the magnetic field above the target should be in the range of 150 to 500 Gauss to increase the plasma density sufficiently. The potential of the target is typically in the region of 300 to 700 Volts with respect to ground and the operating pressure of the chamber is usually between 0.1 and 3 Pascals. The power running from the target at these conditions is in the range of 1 to 40 W/cm^2 with current densities that can vary from 2 to 80mA/cm^2. Film growth is in the range of 1μm per minute for metal coatings but is geometry dependent. The main factors limiting deposition rate are the thermal conductance of the target, the efficiency of the cathode cooling, the melting point of the target and the sputter yield.

An interesting relationship[6] exists between the operating voltage, the current at the target surface and the magnetic field design. It is expressed as

$$I = kV^n \qquad \text{Eqn 4.6}$$

where I is the cathode current, or current density, and V the cathode voltage. The electron trap efficiency can be measured by finding the exponent n. The more efficient the trap, the higher the exponent n. This exponent is typically around 5 for a good electron trap design.

The spark voltage of a planar magnetron discharge is related to the electrode spacing and the magnetic field at the target surface. There is a minimum field strength required, B_c, called the cut-off field. This is expressed[4] as

$$B_c = \left(\frac{2mV_c}{e}\right)^{\frac{1}{2}} \frac{1}{L} \qquad \text{Eqn 4.7}$$

where L is the separation of the electrodes and V_c the voltage at the cathode, m and e are the electron mass and charge respectively.

A design for a DC planar magnetron sputtering system is shown below in figure 4.4. Although there have been numerous advantages mentioned there are also careful design consideration to be taken into account when assembling a system. Cathode cooling, for one, must be more efficient than that for DC diode sputtering due to the higher current densities at the target. Some of the basic concerns still under discussion since initial development are poor target utilization due to the racetrack erosion pattern and arcing on the target surface.

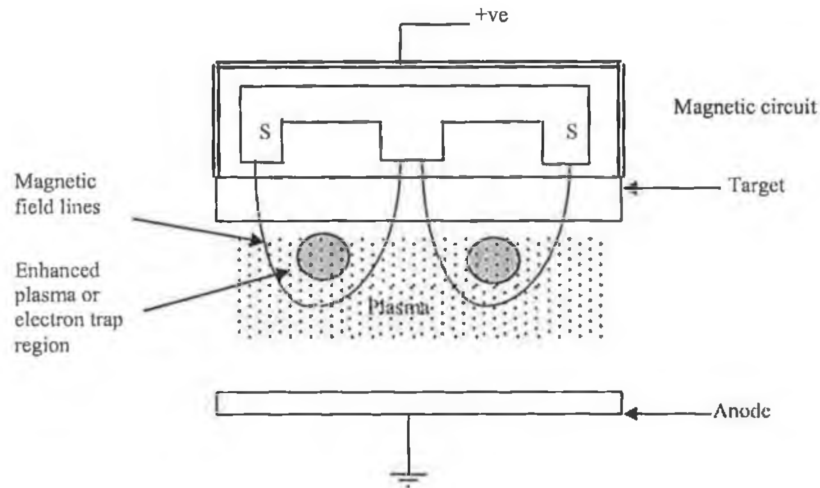

Figure 4.4 **Schematic of a DC Planar Magnetron Sputtering Chamber**

The racetrack profile occurs due to the enhanced plasma in the electron trap region. The dimensions and shape of the racetrack profile are dependent upon the magnet geometry used. An example of erosion profile on a target is shown schematically in figure 4.5 below. Also shown is one of the escape paths which electrons use to exit from the racetrack, usually after numerous interactions with other plasma particles. One method put to use for enhancing target utilization is the use of multiple poles behind the target surface. In effect this creates multiple racetracks on the target surface.

Applications of reactive DC planar magnetron sputtering are few. Reactive RF magnetron sputtering is usually preferred due to the possibilities of insulator film build up on the target surface in the DC mode.

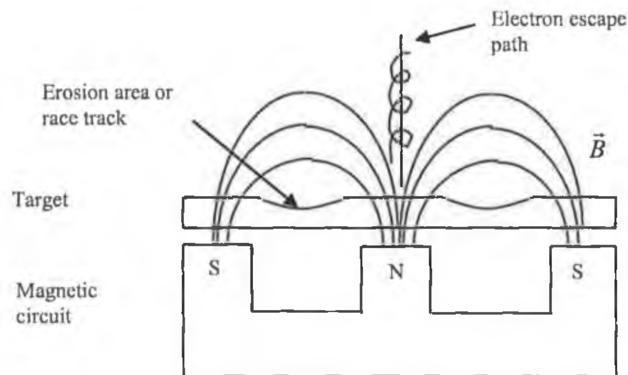

Figure 4.5[6] **Schematic of a target cross section with a magnetron, a racetrack and an electron escape path.**

4.3.2 RF Planar Magnetron Sputtering

The RF mode of magnetron sputtering has the same advantage as RF sputtering over DC diode sputtering, in that a high rate sputtering of insulator materials can be carried out with ease. Using RF excitation frequencies of 13.56MHz, films such as SiO_2 [7] and Al_2O_3 [8] can easily deposited by using reactive gas (reactive RF magnetron sputtering) with a metallic target or by using a insulator target.

One of the main advantages over the conventional method is the low impedance of the plasma; the dc self bias can be as much as ten times smaller.

Table 4.1 shows a comparison between conventional RF and planar magnetron RF sputtering for similar targets.

Target	Sputtering Method	Power density range (W/cm^2)	Rate/power density A/min cm^2/ W	Target – substrate spacing (cm)
Al_2O_3	conventional	1.2 – 2.4	50	3
Al_2O_3	RF PM	3 – 8	51	7
SiO_2	High rate	<20	100	3.3
SiO_2	RF PM	26	93	4.8

Table 4.1 Comparison[9] between conventional RF and RF magnetron sputtering

4.4 Cylindrical Magnetron Sputtering

This process has the same operational characteristics as planar magnetron sputtering, the main difference being the design and arrangement of the chamber and magnets. The classification of these magnetron sources is broken into cylindrical-post and cylindrical-hallow magnetrons. Figure 4.6 shows the basic design of these magnetrons to be mainly tubular in nature, with one electrode located within the second.

Cylindrical post magnetrons are formed in a dumb-bell style design as represented in figures 4.6 and 4.7 below. The magnetic field can be formed through a solenoid internal to the cathode that aligns the field from one wing to the other. This allows for the condition that the field is normal to secondary electrons emitted from the target. Stacking permanent magnets within the cathode may also be used to form the desired magnetic field.

The magnetic field geometry is preferred to be straight, with respect to the cathode surface. The installation of wings help form efficient electron traps once they are kept at the cathode potential. The wing size, W, should be at least three times larger than the gyro radius of the electrons emitted from the cathode. This dimension, W, also controls the region of intense plasma near the cathode, where it is then terminated by the anode intervention. With this criterion the relationship between the field strength, wing size and operating voltage can be expressed[6] as

$$BW = 10V^{1/2} \qquad \text{G-cm} \qquad \text{Eqn 4.8}$$

The field strength[6] is typically B 30 to 200G, *W* is the size of the wing in cm and *V* in volts.
Figure 4.7 illustrates this wing geometry in detail.

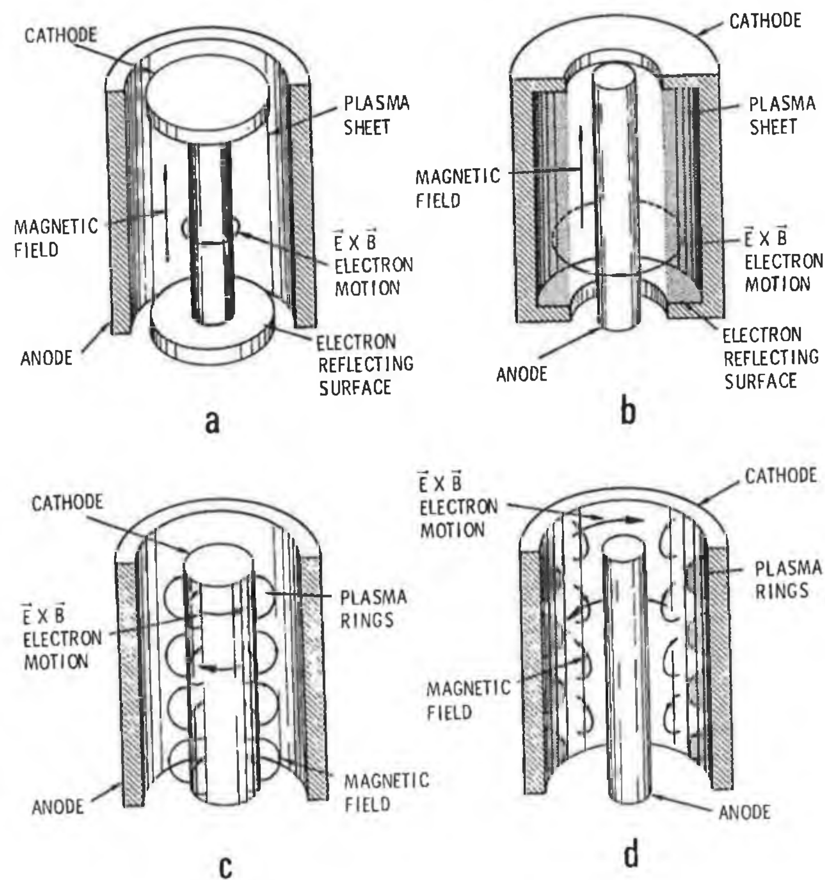

Figure 4.6 Illustration[6] of the configuration of different designs of (a), (b) cylindrical post magnetrons and (c), (d) cylindrical hollow magnetrons.

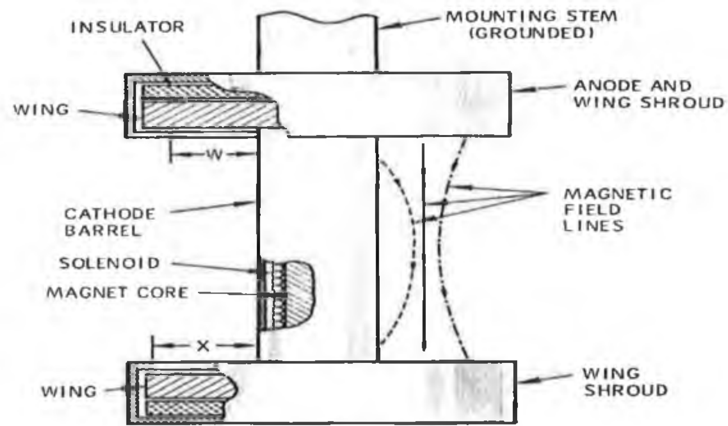

Figure 4.7[6] **Schematic of a cylindrical post magnetron-sputtering source with wing geometry detail.**

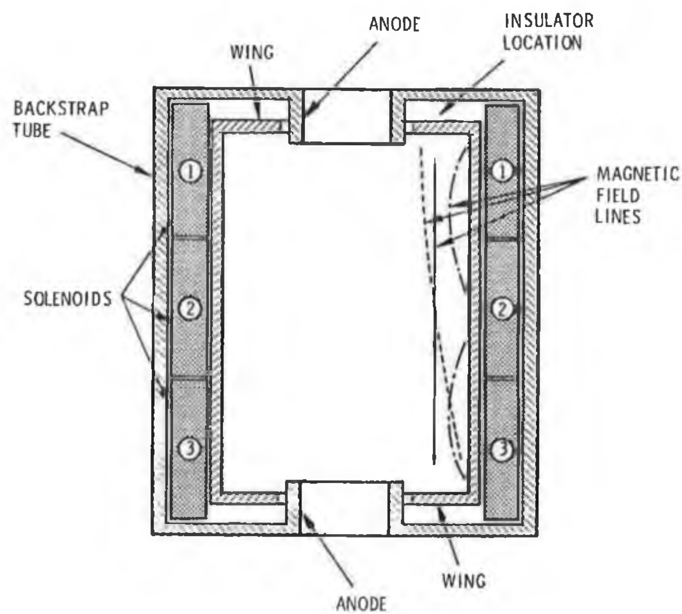

Figure 4.8 [6] **Illustration of a typical cylindrical hallow magnetron sputtering source.**

Hallow cylindrical magnetrons are similar to the post magnetron type. The inclusion of wing geometry is also used here as illustrated in figure 4.8. These wings have the same function of confining the plasma strictly to the cathode surface, as they are at the cathode potential. The use of banks of

electromagnets can also be employed. With good design they can form very efficient electron traps with tapered magnetic fields.

The erosion profiles of cylindrical magnetrons are usually consistent with the length of the cathode due to magnetic field designs. This would usually be uniform erosion along its length, with end tapers. From this it can be said that depositions are uniform also. These magnetrons can be operated at relatively low voltages and achieve high sputter rates. Devices from 10cm to 200cm can been used and uniform current densities over 200 mA/cm^2 have been achieved[6]. Both can be operated in RF mode.

A relationship exists between the spark voltage and axial magnetic field intensity in a coaxial cylindrical electrode configuration. This relationship[6] is

$$B_c = \left(\frac{2mV_c}{e}\right)^{1/2} \frac{2r_2}{r_2^2 - r_1^2} \qquad \text{Eqn 4.9}$$

where r_2 and r_1 are the radii of the outer and inner electrodes and V_c the voltage between the electrodes. Large variations can be seen if the field is too weak or too strong.

4.5 Unbalanced Magnetron Sputtering

One of the limitations of planar magnetron sputtering techniques is that the magnetic field is balanced, i.e. the flux density of the inner and outer magnets are of the same magnitude. This balanced field causes reduced or limited ion and electron bombardment of the growing film. This is advantageous in some applications such as silicon IC fabrication and the coating of temperature sensitive plastics. But when high deposition rates, well-adhered and highly dense coatings are required for complex, non-sensitive or robust substrates, such as drill bits or blades, then this isolation of the enhanced plasma to the target area is not fully desired. This problem can be overcome through the use of unbalanced magnetrons.

The research into unbalanced magnetron sputtering goes back to 1985, when a paper written by Window and Savvides[9] was published in the Journal of Vacuum Science and Technology. The paper discussed charged particle fluxes reaching the substrate from circular planar magnetrons designed by the authors. The difference between the three circular magnetrons used were the flux densities of the magnetic fields produced by electromagnets. The magnetrons were described as type I, type II and intermediate. Type I was an unbalanced magnetron with a stronger central pole, type II was unbalanced with the outer pole stronger and the intermediate was a balanced type. Figure 4.9 illustrates the field shapes examined.

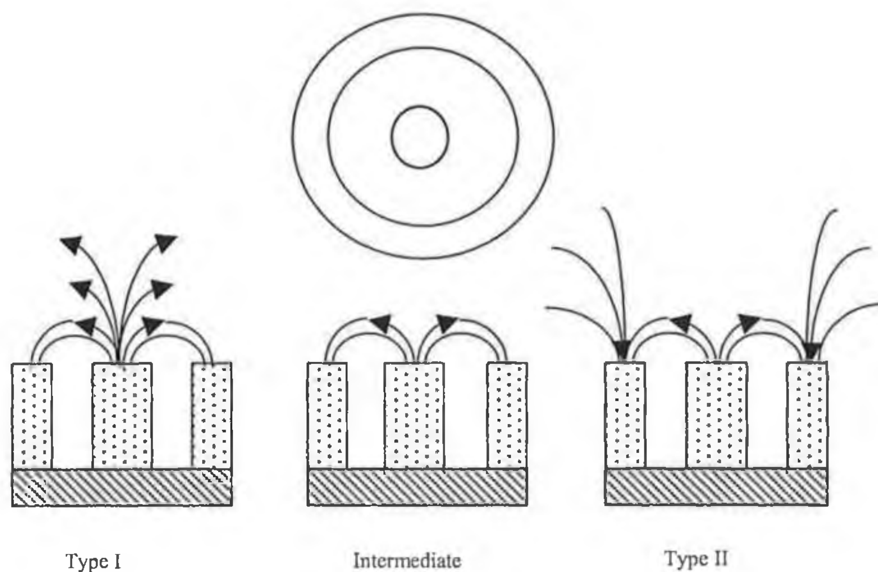

Figure 4.9[9] Illustrations of the magnetron designs developed by Window and Savvides

From their experiments it was noted that for type II magnetron deposition, the plasma extended from the target to the substrate due to the strengthening of the outer pole of the magnetron. This plasma column extending to the substrate leads to a significant increase in substrate ion current density and electron current density measurable at the substrate. The microstructural effects of this increased bombardment are fully packed and well-adhered coatings. Figure 4.10 shows the fundamental difference between conventional balanced and unbalanced magnetrons.

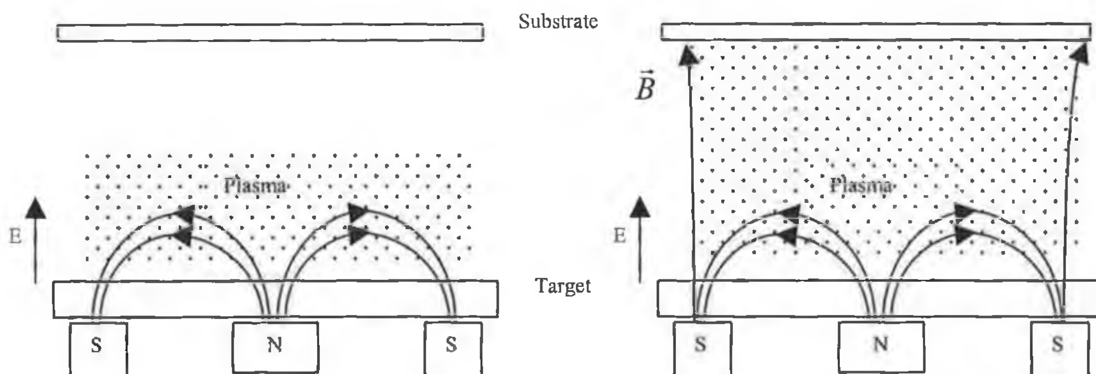

Figure 4.10[11] Conventional balanced and unbalanced magnetrons.

From the initial simple designs and ideas a large array of techniques has evolved for depositing films such as Al, Zr, W, AlN and TiN on complex objects. Conventional single cathode magnetron sputtering enjoys ion current densities up to 2mA/cm^2. With unbalanced single cathode magnetrons, current densities of 7mA/cm^2 have been reported [9,12,13] by Window and Savvides. As well as this Kadlec and Musil have reported[14] current densities measured up to 10mA/ cm^2 in their single cathode system.

The work of Window and Savvides showed that it would be practical to use unbalanced magnetron sputtering in commercial sputtering systems where it is often necessary to have large target-to-substrate distances of 20cm. Magnetron systems have been developed[18] over the past ten years with multiple cathodes to further enhance substrate current densities and film uniformity for complex and large objects.

In multi-cathode systems it is important for the magnetrons to be set up so that the magnetic field is closed. This closed field configuration will result in cathode electrons being confined to the space between the cathodes and therefore increase the plasma density. Magnetrons arranged with open fields will force electrons away from target areas, usually to the vessel walls. The ideal set up is implemented by arranging the magnets of opposite poles to face each other, and not like mirror reflections, as can be seen in figure 4.11 (b). Configurations of type (b) have been measured for substrate ion current density measurements. Results show[17] that the ion current density increases four fold for the unbalanced mirrored configuration over the balanced mirror configuration and a huge twelve fold for the unbalanced linked field configuration over the mirrored balanced field.

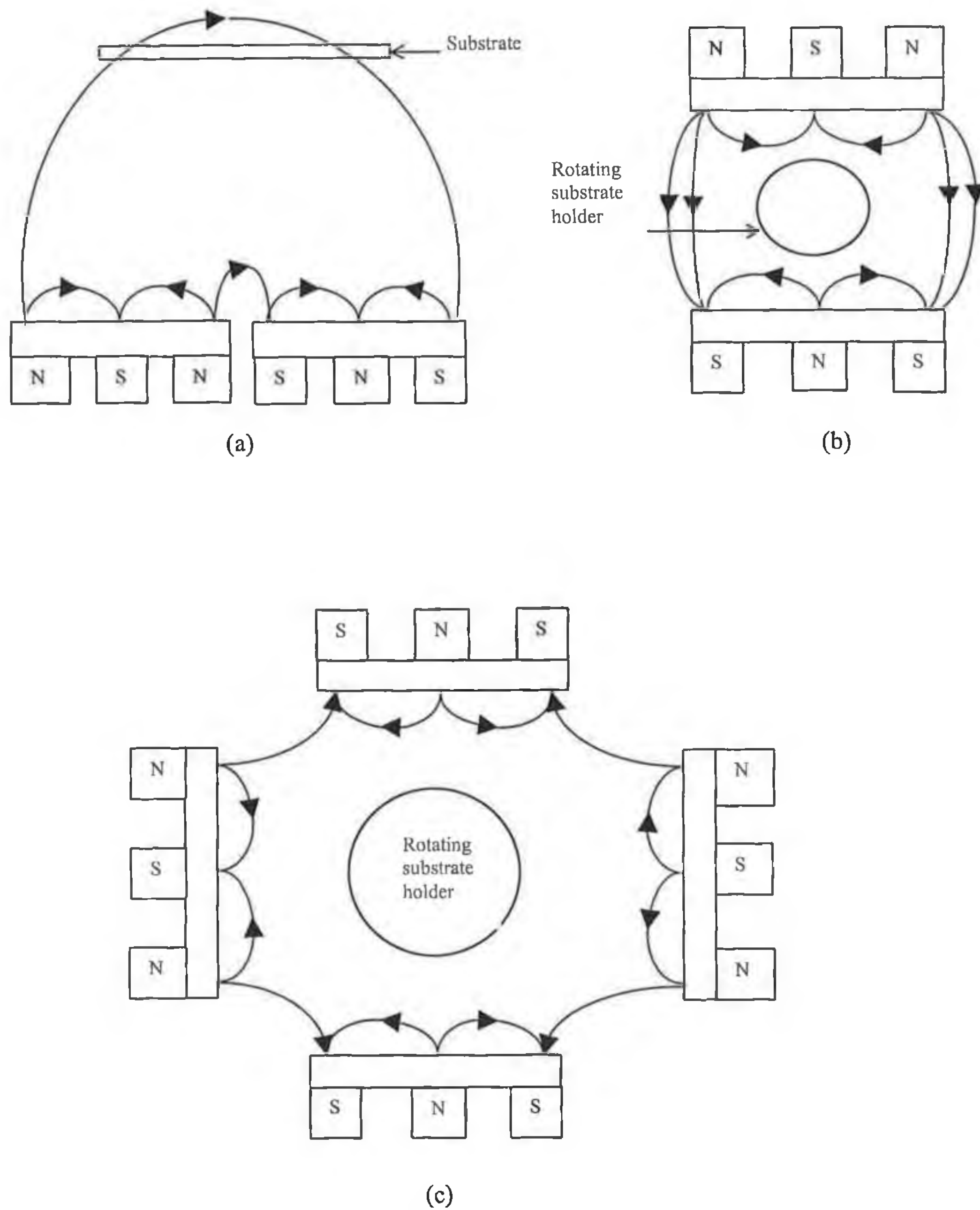

Figure 4.11[11] Multiple cathode configurations for (a) co-deposition, (b) dual closed field magnetron arrangement for alloy, multilayer and reactive deposition on complex substrates and, (c) quad magnetron closed field arrangement for exotic alloys, multilayers and reactive films.

4.6 The Sputter and S-Gun Magnetrons

Both developed by Clarke[10], the sputter and S-gun magnetrons are both circular in nature. The same operational principles apply to these as the other magnetrons described in this chapter. Operation of these magnetrons is at low pressures (0.1 – 2Pa) and they induce the same voltage and current characteristics as planar or cylindrical type magnetrons. Representations are shown in figure 4.12 below.

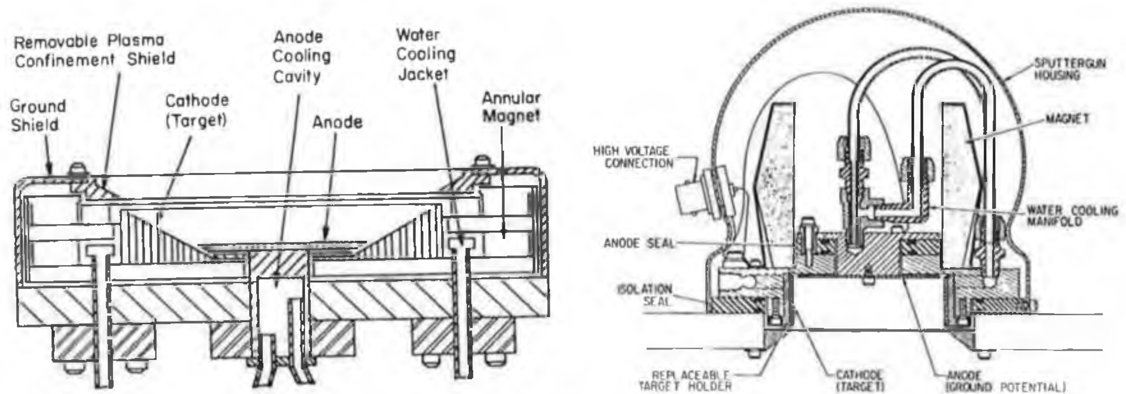

Figure 4.12[10] Cross sectional view of S-gun and Sputter gun magnetron designs.

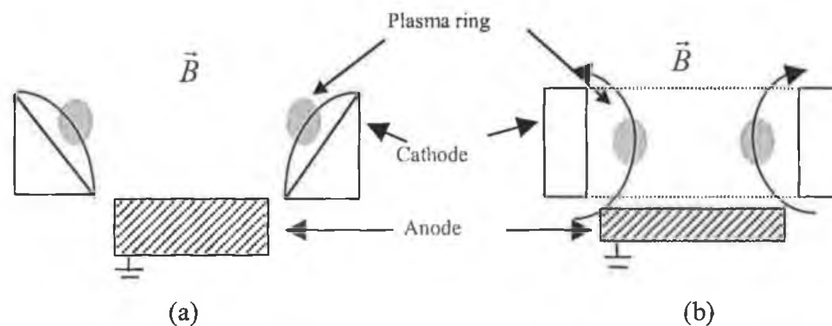

Figure 4.13[10] Cross sectional view of (a) S-Gun and (b) Sputter Gun electrodes with magnetic field and plasma ring designs.

The operation of these devices is based upon the same principles as the previously described magnetron sputter deposition technologies. Electron traps formed on the target surface enhance the ionization of bombarding species. This results in a racetrack type erosion path on the target surface.

The differences in these devices are the topology of the cathode and anode configuration, as can be seen from figure 4.13. Typical magnetic fields are in the low hundreds of Gauss and are usually set up with permanent magnets. These magnetron deposition systems, which are typically operated in bias mode, have good target utilization coupled with high deposition rates.

Chapter Four References

[1] K. Wasa and S. Hayakawa, Jpn. Patent 642,012 (1967), Matsushita Corp.

[2] A.S. Penfold, Handbook of Thin Film Process Technology, Institute of Physics Publishing, London (1995) A3.3.

[3] B. Chapman, Glow Discharge Process, Wiley, New York (1980).

[4] W.H. Class, Basics of Plasmas, Materials Research Corp. (1983).

[5] T. Sheridan and J. Goree, J. Vac. Sci. Technol. A 7 (1989) 1014.

[6] J. Vossen and W. Kern, Thin Film Processes, Academic Press, New York (1978) Chapter II.

[7] L. Hartsough and P. McLeod, J. Vac. Sci. Technol. 14 (1977) 123.

[8] R. Nowicki, J. Vac. Sci. Technol. 14 (1977) 127.

[9] B. Window and N. Savvides, J. Vac. Sci. Technol. A 4 (2) (1986) 196.

[10] J. Vossen and W. Kern, Thin Film Processes, Academic Press, New York (1978) Chapter II-3.

[11] P. Kelly, R. Arnell, and H. Ahmed, Surface Engineering vol. 9. No. 4, (1993) 287.

[12] B. Window and N. Savvides, J. Vac. Sci. Technol. A 4 (3) (1986) 453.

[13] B. Window and N. Savvides, J. Vac. Sci. Technol. A 4 (3) (1986) 504.

[14] S. Kadlec, J. Musil, W.D.Munz, and L. Valvoda, Int Conf. On Ion and Plasma Assisted Tech. Switz, (1989).

[15] W.D.Munz, Surf. Coat. Technol. 48 (1991) 81.

[16] P. Kelly and R. Arnell, J. Vac. Sci. Technol. A 16(5) (1998).

[17] W. Sproul, Rudink, Graham, and S. Rhode, Surf. Coat. Technol. 43/44 (1990) 270.

[18] D. Mononghan, D. Teer, P. Logan, R. Arnell, and I. Efeoglu, Surf. Coat. Technol. 60(1993) 525-530.

Chapter Five

Design and Operation of a Magnetron Sputtering System

5.1 Introduction

The following chapter is dedicated to describing the design and construction of both the variable balance magnetron sputtering system and energy analyser used in this project. Firstly, an introductory piece is given on typical sputtering system design.

5.2 Sputtering Systems

Sputtering systems are usually designed for a particular application and therefore can vary greatly in size and topology. Even though the arrangements may be different, the components are generally the same for all sputtering systems. Chapter four reviewed magnetron sputtering technology, and from the basic single cathode chamber designs to the more advanced multi-cathode systems it can be recognized that the same principle designs apply to all.

Commercial systems for depositing films on numerous types of substrates are available from companies such as Iontech, Balzers, Applied Materials and Novellus. These systems tend to be well equipped with advanced software and robotic arm substrate handler units and so tend to be extremely expensive. On the other hand, most systems that are designed in-house are of a much simpler design yet still incorporate the same functions be it on a more manual style of intervention. These systems usually encompass stainless steel chambers with the target and substrate holder designed to fit for the appropriate application, and to handle whatever substrates are to be coated. These systems are also usually designed for various modes of sputter deposition.

5.3 System Design

The design of the system was kept simple. A stainless steel T-piece chamber measuring 50cm long by 20cm in diameter was used as the main deposition chamber. Attached to this is a dual piston high-pressure VAT pneumatically operated isolation valve, which isolates a cryogenic pump from the main chamber. Clamped to either end of the chamber are removable wall plates for component feedthroughs and for accessing chamber

parts. There are two KF connection ports to the chamber for pressure gauges, electrical feedthroughs and a roughing line.

An overall schematic of the sputtering system is shown in figure 5.1 while figure 5.2 shows the electronics rack used with the various power supplies and meters required to run the system.

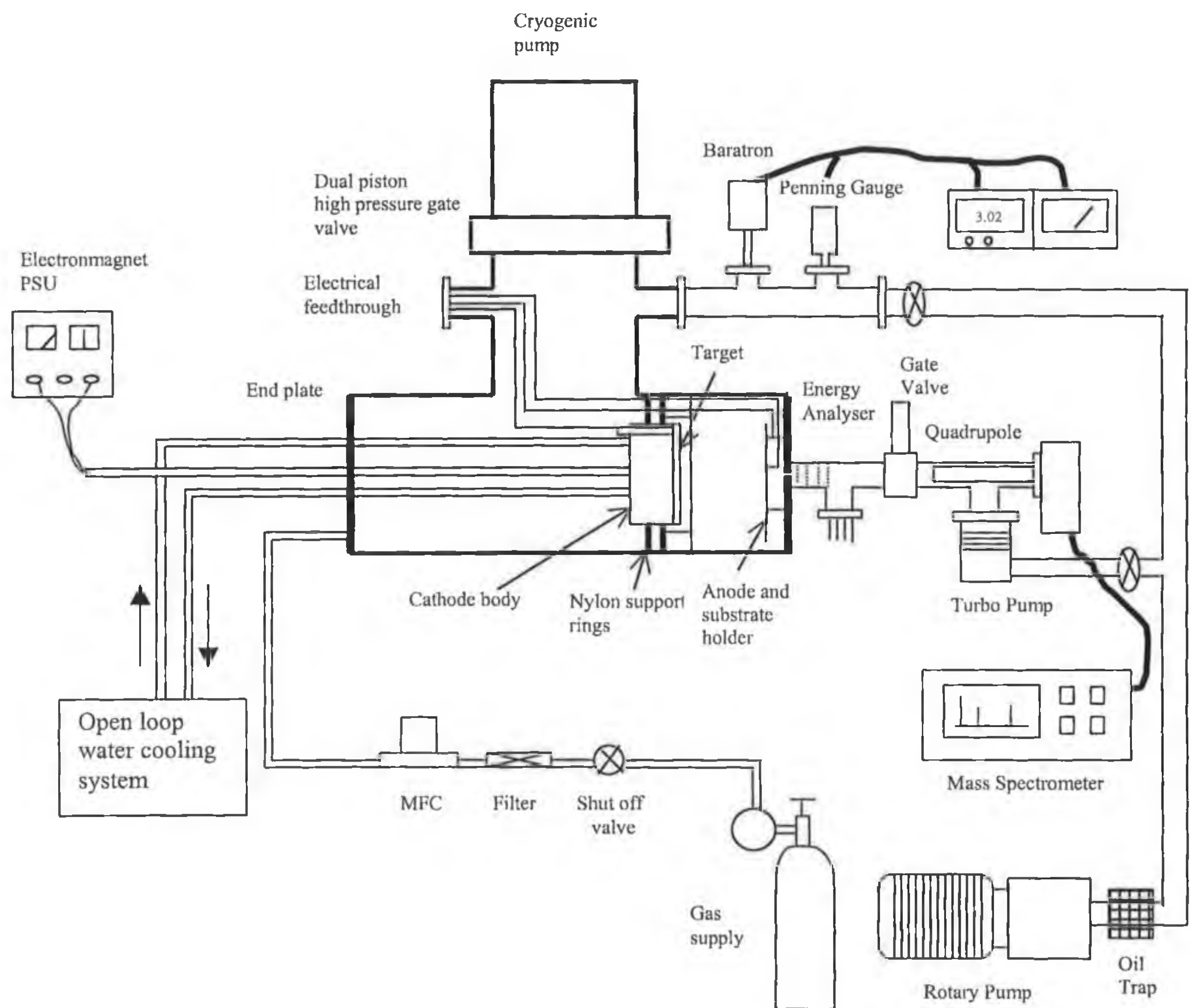

Figure 5.1 **Schematic of the sputtering system constructed and some peripheral devices.**

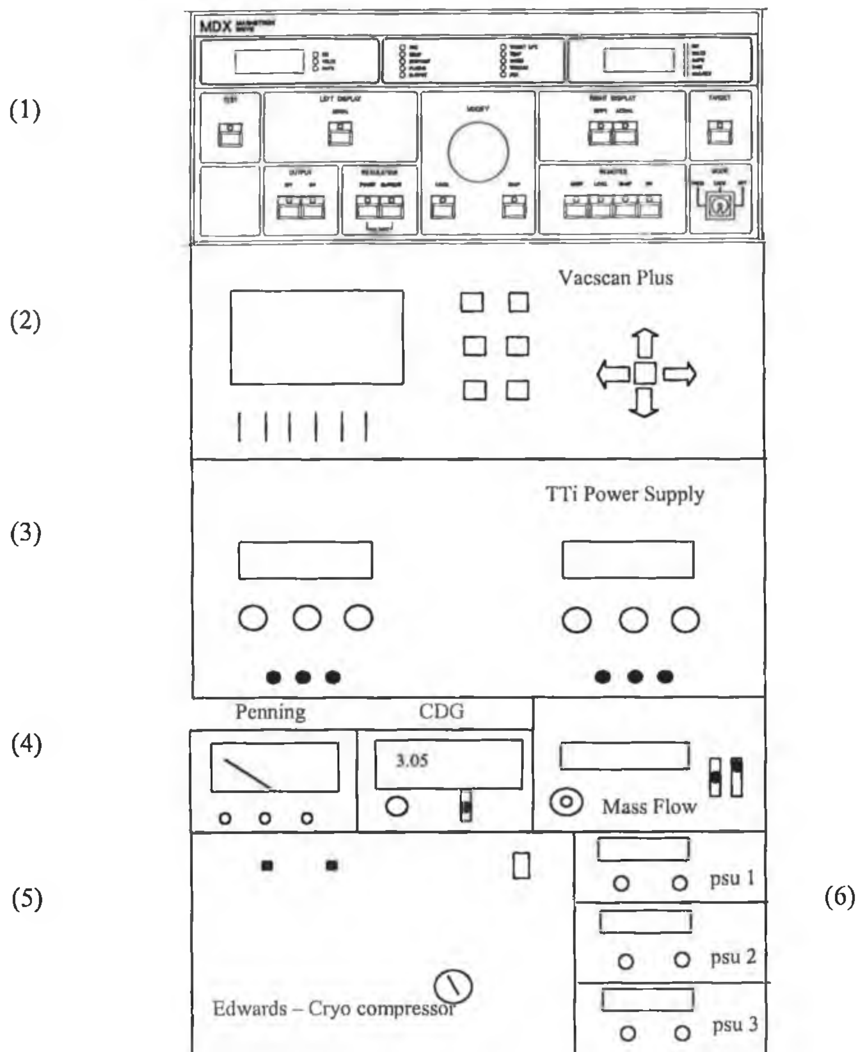

Figure 5.2 **Electronics rack required for operation of the sputtering system (1) magnetron driver, (2) TTL 4A solenoid power supply, (3) mass spectrometer controller and display unit, (4) pressure gauge displays and MFC controller unit, (5) Cryo-pump helium compressor unit and (6) additional power supply units for energy analyser.**

5.4 Pumping and Vacuum System

The pumping system must be able to evacuate the chamber to a very low base pressure so as to fully remove impurities in the system such as moisture, carbon dioxide, oxygen and nitrogen. These impurities cause increases in film stress, resistance and decreases in mechanical and optical properties. To bring the deposition chamber to within these specifications a cryogenic pump (see appendix A) with a pump rate of 1500 l/s (air) is used. This pump is roughed down initially with an Edwards' rotary pump. A chamber base pressure of below 5E-7 Pa is acceptable for the application at hand.

To ensure good vacuum, viton o-rings and copper gaskets are used where appropriate on all connections. Swagelock ferrules and olives are used on gas and water lines running into the chamber and for connection to the target.

The chamber is firstly roughed down with an Edwards' pump until an acceptable leak rate of below 0.2 Pa per minute is achieved. At this point the gate valve is opened to 25% with the first piston and the cryogenic pump is let evacuate the chamber to 1E-4 Pa. The gate valve is then fully opened and the chamber is let to pump down to base pressure (5 E-7 Pa). These high vacuums are measured with an Alcatel Penning gauge.

A foreline trap is used on the rotary pump in order to protect it from granular materials falling down the foreline into the pump and causing damage. An oil trap is also incorporated into the foreline to protect the chamber and components from oil back streaming up the line, which can happen at low pressures, when the pump is in use for long periods of time. This is due to the condition that as oil temperature increases vapour rises from the surface. This trap also protects the back-streaming vapors from reaching the turbo pump on the analyser chamber, which the roughing pump also backs during operation.

5.5 Gas Flow, Control and Pressure Measurement

The gas chosen for sputtering was argon with a purity of 99.999%. Benefits from using such a high purity gas are obvious. If the effort is taken to ensure the system is pumped to a very low base pressure and good sealing surfaces are used to avoid contamination, normal grade argon will result in poorer films due to nitrogen and oxygen content in the gas. The differences between five nines and standard grade argon are given below in table 5.1

Purity	N_2 (ppm)	O_2 (ppm)
99.999%	<3	<0.2
Standard	<10	<2

Table 5.1 Quantitative differences of contamination in different grades of argon gas.

The sputter gas is isolated from the chamber by a quarter turn valve ensuring that evacuation of the chamber can take place. When gas is required, the quarter turn valve is opened and the gas is forced through a 0.2 micron filter to a Tylan mass flow controller which responds to user inputted set points from a controller unit mounted on the electronics rack. The set point can be increased to reach a predetermined pressure value. Feed back to the controller unit is provided by the MFC.

The process pressure measurement is carried out by a heated sensor 100mTorr MKS Baratron® series 127 (appendix C.). This device measures accurately the pressure in the chamber in the range of 1 to 50mT. Zeroing can be carried out at chamber base pressure. Typical accuracy of this type of capacitance diaphragm gauge is +/- 0.25% of reading.

5.6 Cathode Considerations

In designing the cathode many factors had to be taken into account including an adequate cooling system, target attachment, magnetron dimensions and installation, power attachment and vacuum integrity. The cathode that has been designed satisfies all these criteria and requires minimum servicing. The cathode is machined from a H30 aluminum block. A schematic is given below in figure 5.3.

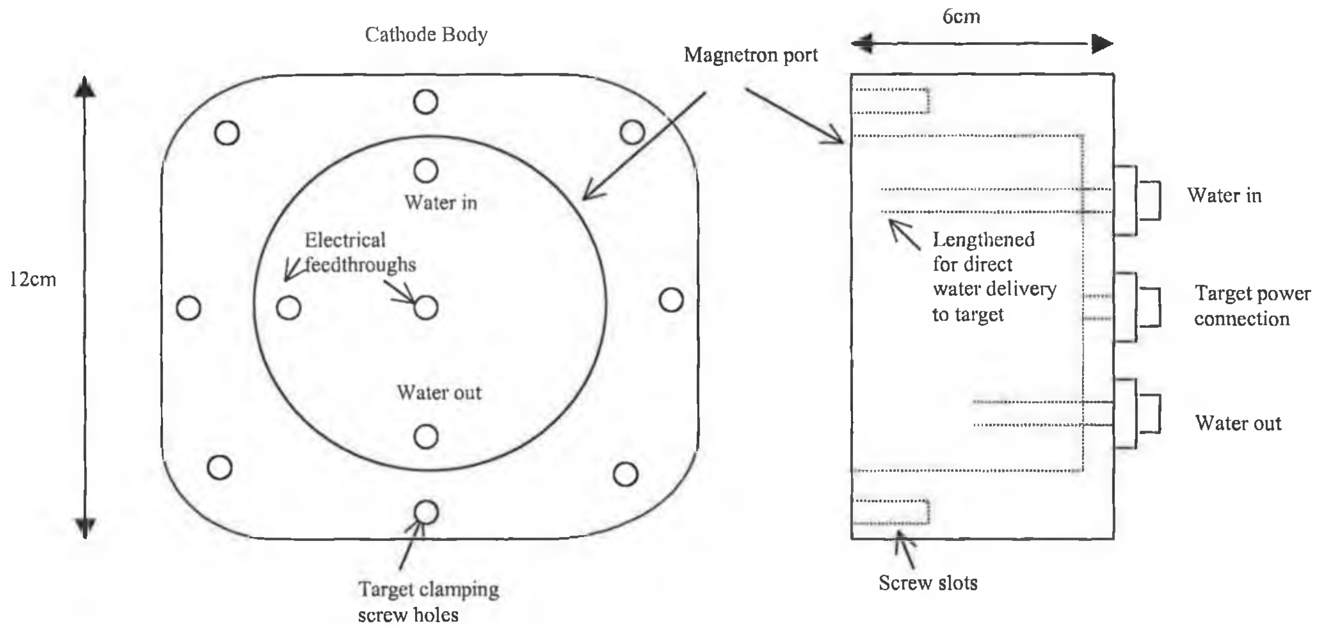

Figure 5.3 **Schematic of the manufactured cathode body.**

5.6.1 Target Fabrication

The target is fabricated from normal grade aluminum, a cost initiative, as film purity is not a main consideration of this project. Targets should be manufactured from non-strained metals and where possible without voids or bubbles as these can induce spitting or melting on the target surface due to the high power densities targets are operated at.

Ideally, high purity targets should be manufactured within a vacuum environment to ensure a low moisture and contaminant content. Such methods as hot-pressed sintering are available from target manufacturing companies and tend to be expensive due to the tight manufacturing tolerances.

Eight clamping holes were tapped in the 7mm thick target for fastening it to the cathode body as can be seen in figure 5.4. A smooth finish on the target cooling side is required for a good o-ring seal against the cathode surface.

Figure 5.4 Photograph of the target prior to and during sputtering.

5.6.2 Target Cooling

In magnetron sputtering, efficient target cooling is essential due to the high levels of power dissipated at the target surface. It has been estimated[1] that over 70% of the power delivered to the cathode is turned into heat at the target surface. A few practical methods of removing this heat are gas flow, oil, and water flow to the rear of the target. Due to the high temperature possible (app. 400°C) gas flow does not seem adequate and would turn out to be expensive and complex. Oil on the other hand would provide good thermal conductivity but is messy and dirty. Using chilled water with adequate flow rates provides the best, cleanest and least expensive choice even though hazards are present. Due to the cathode being inside the chamber the water must be piped to the cathode through the vacuum environment. Seal failure at the cathode or in the piping can be catastrophic for chamber components such as the cryogenic pump. To reduce probability of failure PTFE was chosen for its varying temperature characteristics, flexibility and strength over other materials such as Nylon.

The delivery of the water should be brought as close to the target rear as possible. Due to this, steel pipes have been welded onto swagelock tube connectors in order to provide a reliable and durable delivery of cooling water, in jet form, directly to the top of the target rear (figure 5.3). The pressure build up and line diameter govern the return flow of water from the cathode assembly. The maximum output of water from the return line has been measured at 5 liters per minute, which is adequate for the cooling of up to a 5kW discharge[2].

5.6.3 Cathode Insulation

It is generally not desirable to have objects other than the target, such as screws and fittings sputtered. To avoid this a shield at ground potential must cover the entire cathode body. This shielding is usually in the form of a cathode casing. The distance between the cathode and the casing cannot be greater than the cathode dark space. This is to ensure that the conditions are not present for the ignition of plasma between the two (less than 10mm typically).

Rather than design a shield for the cathode a new method for insulating was developed by the author. An inexpensive polybromide tape cured at 240°C was applied to the external surface area of the cathode. This insulating tape has a voltage rating of 120KV/mm. Once cured, an aluminum adhesive tape was then applied over the insulating tape so as it could be grounded to the chamber wall with a strap. This method avoided the use of a cumbersome shield that can be difficult to machine to the tolerances required and proved easy to clean and maintain. The cathode was then centered in the chamber by using two nylon rings that were machined to the exact dimensions of the cathode so as to fit around the outer body. These are shown below in figure 5.5 (b). This support proved consistently adequate and provided easy access to the target when it was required to be removed from the chamber.

A shield at ground potential is used to reduce 'rim effect' or ions attacking the sides of the target surface. This ground shield, illustrated in figure 5.5 (a), also covers the target clamping screws and ensures that the sputtered area is confined to the center of the target. These rim effects are illustrated in figure 5.5 (c) and (d).

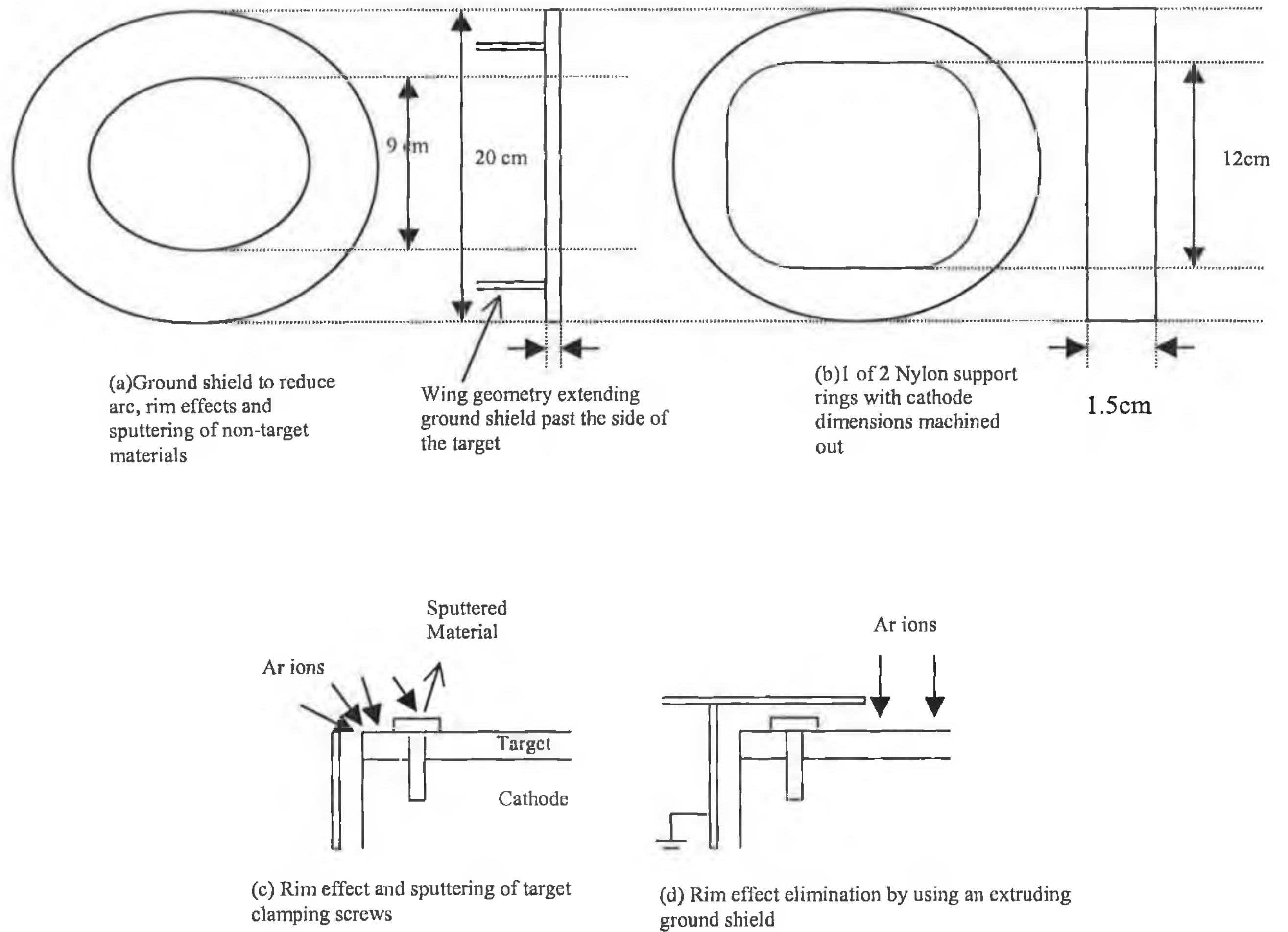

Figure 5.5 **Schematic representations of (a) target ground shield and (b) nylon target supports. Also shown is the (c) rim effect and (d) elimination of rim effects during sputtering by application of the protruding ground shield.**

Figure 5.6 below shows the cathode body removed from the chamber with the support rings attached

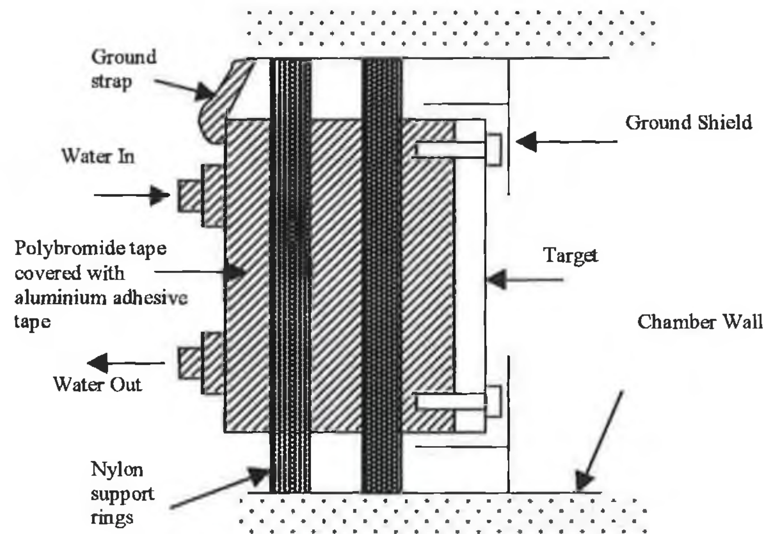

Figure 5.6 Schematic and picture of the overall cathode assembly with external components.

In effect the ground shield reduces the target area to an effective sputtering area which is measured by the aperture in the shield. This effective area can be seen below in figure 5.7. It has also been reported that this shield reduces arcs on metallic targets. This shield attaches onto the nylon centering rings and has the dimensions of the chamber diameter.

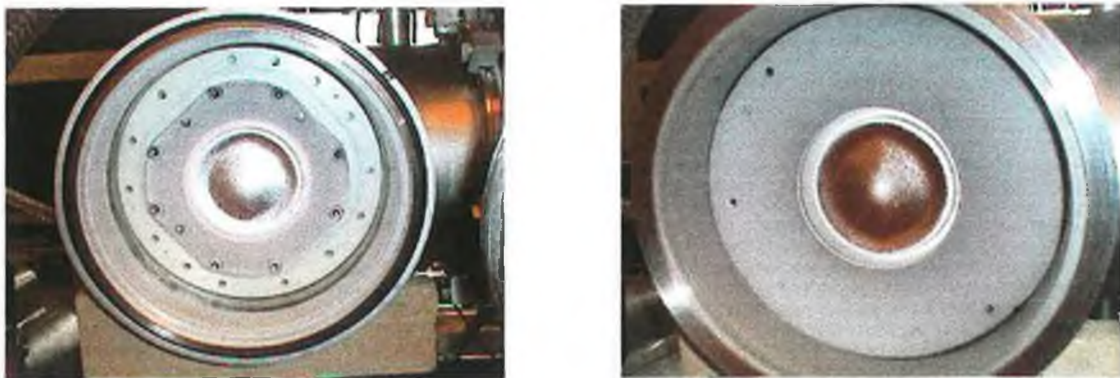

Figure 5.7 Picture of the target and cathode assembly in situ with and without the ground shield.

5.6.4 Power Control

For conventional DC diode sputtering, power supplies are required to have large voltage output (1000 to 5000VDC) capabilities as these devices are usually operated in a voltage regulation mode. In magnetron sputtering, however, these large voltages are not required as typical operating voltages are between 300 and 700VDC. For magnetron applications the power supply is operated in a current regulation mode due to the large current densities possible at the target. The size of the target and magnetron will dictate the size of the power supply output required. For cathodes less than 100cm^2 which are operated at relatively low currents (<1 amp) a 5 kilo-Watt generator will suffice.

These power supplies must be advanced enough to have good arc detection and suppression capabilities due to the major and minor arcs that often occur on target surfaces and also from the cathode to ground. Aluminum targets are prone to arcing as they are easily oxidized upon exposure to air. A power ramp up facility is a feature that is advisable to use when pre-sputtering a target after pump down.

A supply that satisfies these criteria and which was used for this application is an Advanced Energies 5kW magnetron driver. Some characteristics of this power supply are given in appendix B.

5.7 Anode Construction and Considerations

The anode was fabricated from a 2mm thick aluminum sheet. It measures 10cm square and has appropriate holes drilled for attachment of devices such as thermocouples and probes. A schematic of the anode and clamp is given below in figure 5.8.

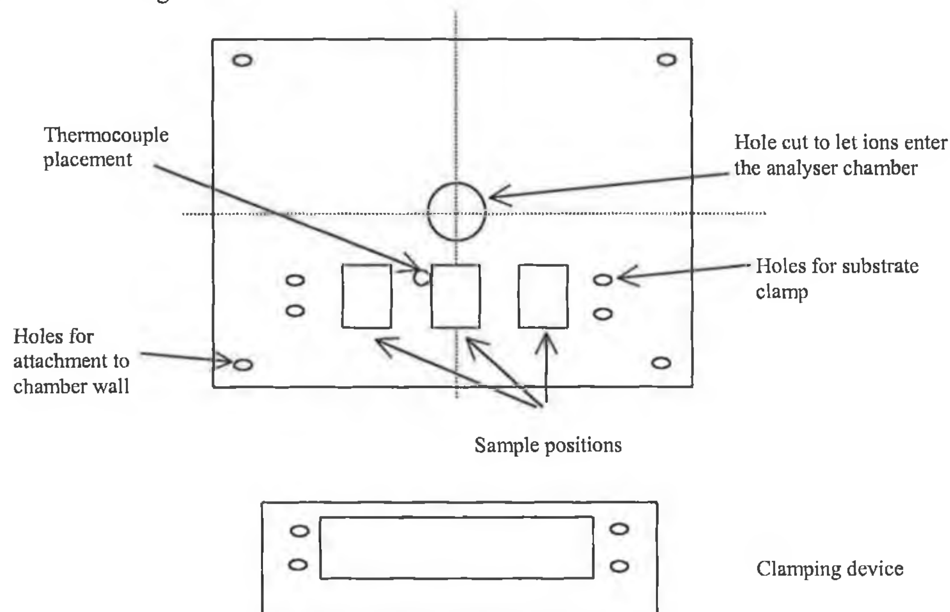

Figure 5.8 **Schematic of the anode and substrate clamp.**

The anode is attached to the chamber wall plate with four insulating spacers. These allow the anode to sit 10mm form the wall and allow for biasing the substrate during deposition or for applying large negative voltages to the substrate for sputter-etch cleaning prior to deposition.

No substrate heating device is required as this is one of the measurable parameters of the process. The hole at the center of the anode plate is to allow ions that are emitted from the magnetron discharge to pass through and into the analyser chamber for detection. A corresponding hole of much smaller dimensions is placed in the center of the chamber wall plate. This will be discussed later.

To allow for the independent growth of samples without opening the chamber between depositions a rotary feedthrough and shutter were designed to allow for the covering of two samples with the exposure of one at all times. This allows for multiple experiments to take place without effecting two samples and allows for the study of depositions at different positions relative to the target center. The sample positions are shown in figure 5.8 above. Figure 5.9 below shows schematic diagrams of the rotary and the shutter system.

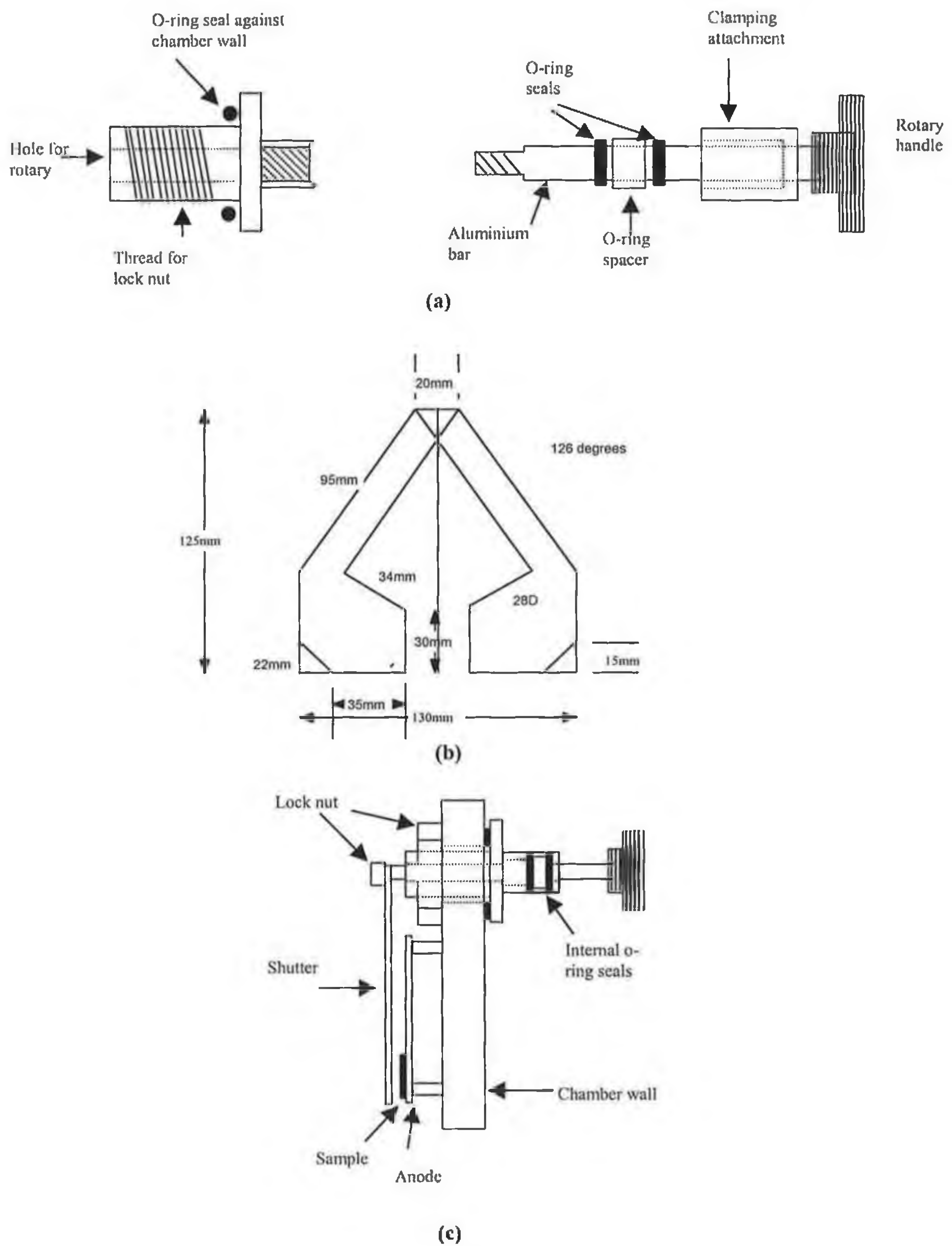

Figure 5.9 **Schematic of the (a) rotary feed through,(b) shutter design and (c) the assembly of both in situ.**

5.8 Magnetron Design and Construction

Due to restrictions in the cathode size, the magnetron had to be designed to fit within the given space behind the mounted target. Typical circular magnetron design geometry was employed, as shown in figure 5.10 below, with ferrite magnets arranged in a ring pattern for the outer pole assembly. The inner pole is a solenoid constructed in house with an iron core.

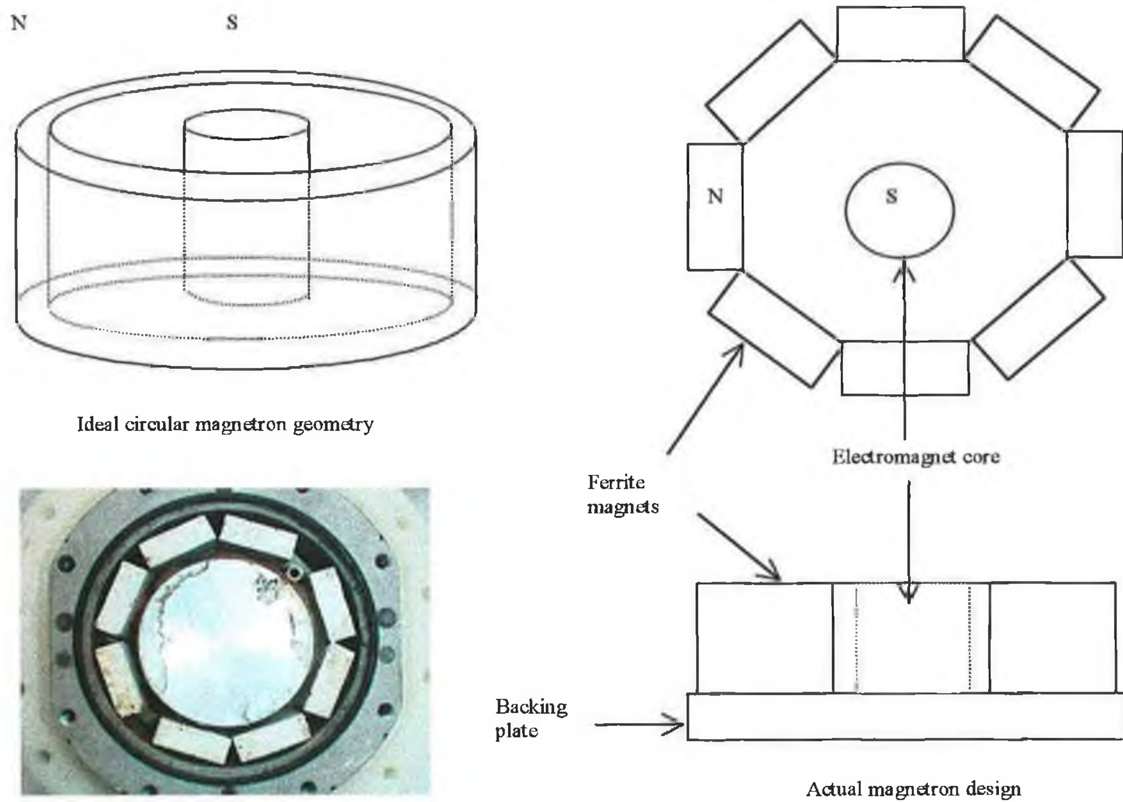

Figure 5.10 Schematic representations of an ideal and actual magnetron designs. Photograph of actual magnetron with solenoid inserted in cathode body.

The arrangement of the target to magnetron can be represented schematically below in figure 5.11.

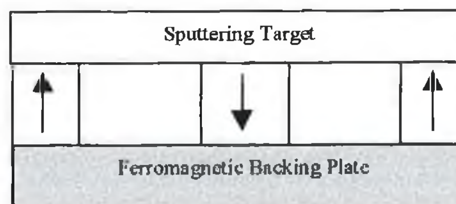

Figure 5.11 Schematic[3] representation of a standard two dimensional magnetron geometry. The arrows indicate the direction of the magnetization vector.

The eight ferrite magnets measure 10mm x 25mm x 28mm in volume. These are glued to the ferromagnetic backing plate, which is fabricated from a 10mm thick iron plate. The magnetron is then coated in a corrosion resistive paint due to the water flow present in the system. The design of the backing plate must take some considerations into account such as cooling lines, solenoid power lines and solenoid attachment. These conditions are satisfied with the construction carried out to the specifications in figure 5.12 below.

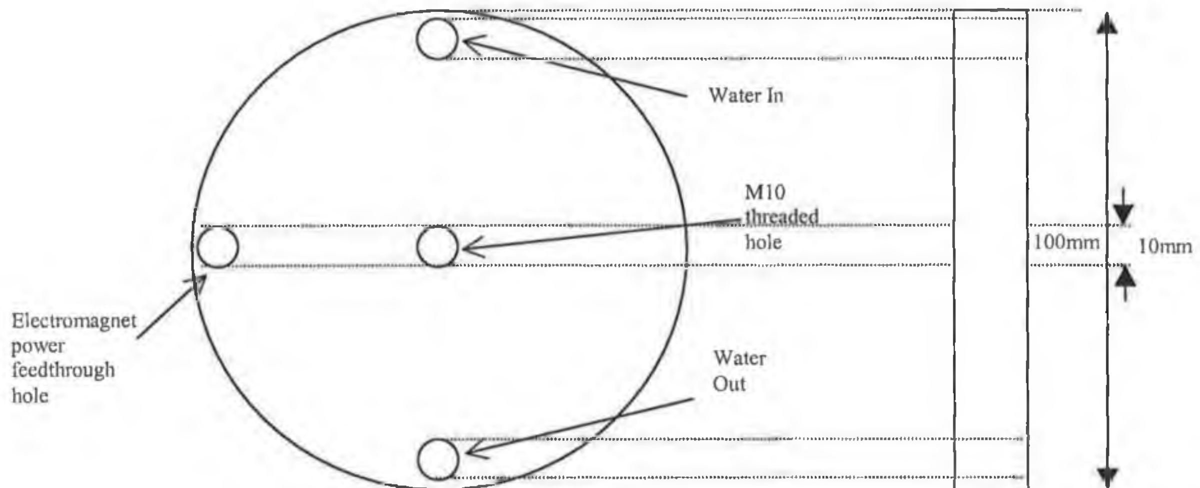

Figure 5.12 Construction of the ferromagnetic backing plate.

The M10 tapped hole in the center allows for the reliable attachment of a suitable electromagnet constructed to the allowed specifications. These specifications are reported on below.

5.8.1 Solenoid Design

The solenoid is constructed around an ideal design. Due to the length of the solenoid being small and not a minimum of ten times the diameter, the ideal equations of magnetic flux induction cannot exactly be applied but do give a reasonable estimate. The basic idea of a solenoid is when a coil of wire is rapped tightly around a core, and a current (I) is passed through that coil, a magnetic field is produced along the axes of the core.

Firstly, it can be explained in terms of the magnetic field produced around a long wire. This is represented in figure 5.13

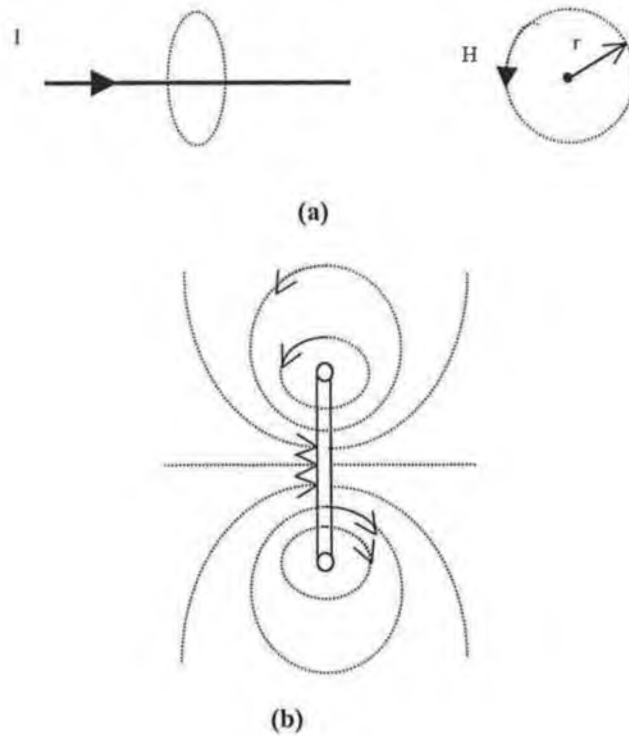

Figure 5.13 Field produced (a) around a long current carried wire and (b) around a single turn of wire

This field produced can be written[6] as

$$\oint H dl = H \times 2\pi r = I \qquad \text{Eqn 5.1}$$

so

$$H = \frac{I}{2\pi r}$$

where H is the magnetic field strength at a distance r and has units of amperes/meter.

A solenoid can then be constructed from a set of coils like that in figure 5.13 (b). The field produced is represented below in figure 5.14

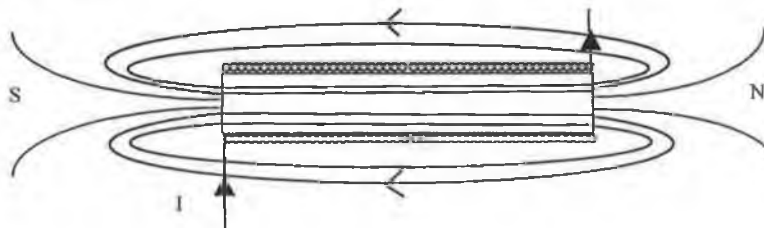

Figure 5.14 Illustration of the effect of the field produced from N turns of a wire.

The insertion of an iron core allows for the concentration of the magnetic flux lines. It also allows for the amplification of the magnetic flux due to the domains of the iron core being lined up in the direction of the magnetic field orientation. Temporary field poles of north and south are set up when a current I flows through the coil.

An expression to equate the flux density can be written as

$$B = u_r u_0 H \qquad \text{Eqn 5.2}$$

where μ_r is a constant for a particular material called the relative permeability. This is introduced due to the iron core (typically around 1000 and has no units), μ_0 is the permeability of free space (4.7E-7) with units of mass, length and charge^{-2}. B is measured in Tesla and H in Am^{-1}.

For a solenoid, H can be represented as a function of the number of turns and the current I that flows through the wire.

$$H = \frac{Ni}{l} \qquad \text{Eqn 5.3}$$

where N is the number of turns in a solenoid winding, l the length of the solenoid and I the current.

It can then be written that at either end of the solenoid the flux density can be approximated to

$$B = \frac{\mu_r \mu_0}{2} \frac{Ni}{l} \qquad \text{Eqn 5.4}$$

5.8.2 Solenoid Construction

To avoid damage to the iron core and to the magnetic field geometry from welding, aluminum discs are bonded to the iron core with a Loctite 326 adhesive and activator. This gives a strong, durable bond that is also resistant to moisture. The iron core is covered with an anti corrosive paint to avoid degradation from the cooling water. The coil used has 1000 turns of insulated copper wire with a diameter of 0.71mm and was manufactured in house. This wire can hold up to 2 amps in the coil for deposition periods without over heating. The aluminum discs provide good heat conduction to the cooling fluid surrounding the electromagnet. In order to prevent water from circulating between the coils and to keep the coil tight the surface of the solenoid was covered in an epoxy resin and allowed to harden.

As can be seen from figure 5.15, an M10 thread has been machined on one of the aluminum discs. This allows the electromagnet to be threaded into the backing plate so as it can be supported in the center of the

cathode behind the target. It also ensures that there is equal spacing between the core of the electromagnet and the ferrite magnets at all times, which is important for field geometry and uniformity.

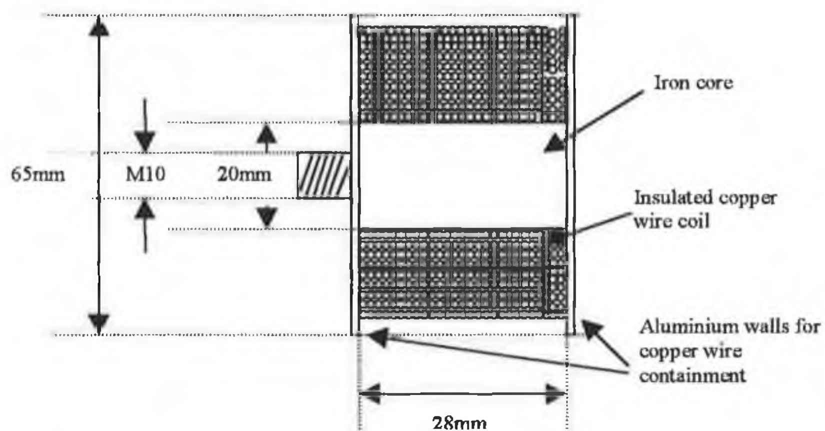

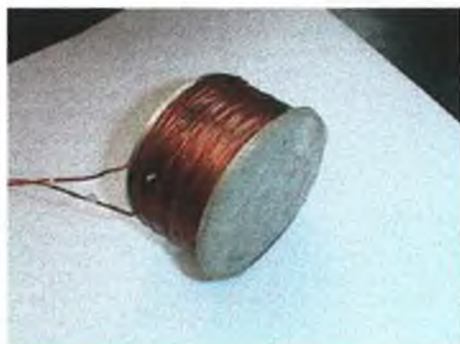

Figure 5.15 Design of an removable solenoid with 1000turns.

5.9 Analyser Chamber

The analyser chamber that is attached to the main sputtering chamber is an important part of the overall system. This chamber allows ions, atoms and electrons that are bombarding the anode to be sampled and categorized into their various species according to their energy and mass. The chamber is divided into two portions, the energy analyser and the mass analyser. A schematic of the analyser chamber is given below in figure 5.16.

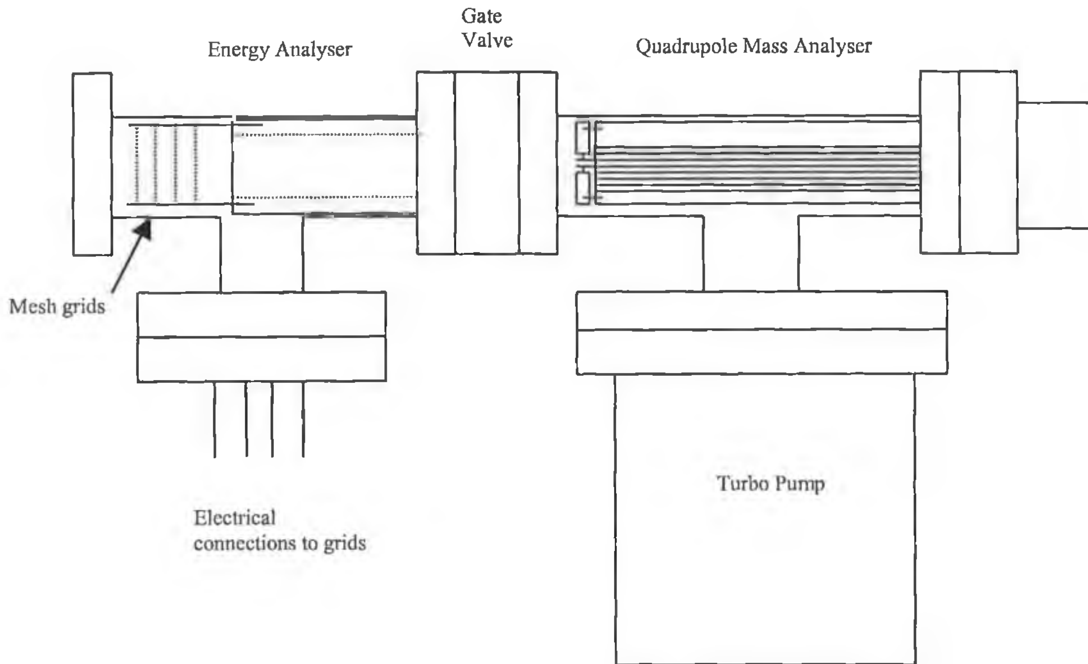

Figure 5.16 Schematic of the analyser chamber

5.9.1 Energy Analyser

In many plasma experiments it is desirable and even necessary to measure the energy distribution of plasma particles. The use of multi grid electrostatic analysers generally can be employed to carry out this task. These devices can take two forms, spherical grid systems or planar grid systems. These are represented in figure 5.17. The analyzing grid in these systems is usually a metallic mesh. A voltage is applied to the analyzing grid, which is used to block lower energy constituents of the plasma or particle beam that pass through it.

Parameters affecting the characteristics of the analyser are size, material, electrode shape, spacing between grids and the mesh size. Materials that can be used are stainless steel, tungsten, nickel, molybdenum and copper amongst others.

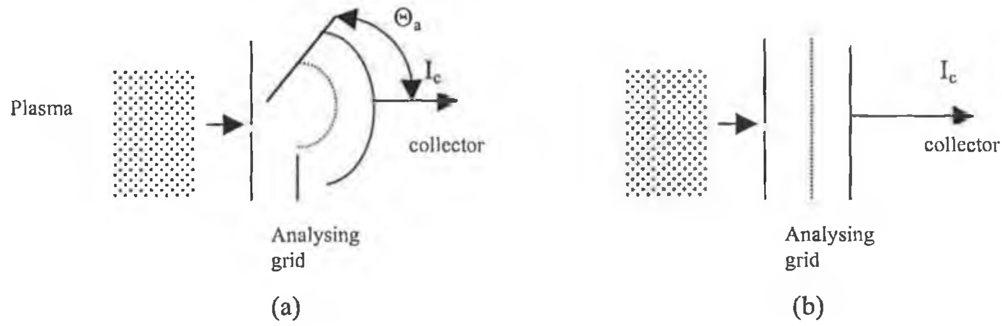

Figure 5.17 Typical designs of (a) spherical grid and (b) planar grid analysers

When using an analyser in a plasma it is necessary to minimize two things (a) distortion of the plasma due to the presence of the analyser which is carried out by minimizing the aperture which samples the plasma and, (b) distortions of the energy distributions due to the field effects at the orifice which can be reduced by correctly designing the aperture between the chambers.

The current seen at the collector electrode is a function of many parameters. For the spherical grid analyser this electron current can be expressed[5] as

$$I_c = \frac{ne}{4} dA \sin^2 \Theta_a \int_{V_a}^{\infty} vf(v)dv \qquad \text{Eqn 5.5}$$

where V_a is the minimum energy required to be collected, Θ_a is the acceptance angle of the analyser, n the electron density, dA the area of the aperture which is assumed to small, e the electron charge and v the velocity. The integral term can also be expressed as energy dependent and then the minimum energy to be detected is E_a.

$$vf(v)dv = \frac{\sqrt{2E}}{m} F(E)dE$$

For a planar grid analyser the electron current collected can be expressed[5] as

$$I_c = endA\frac{\sqrt{2}}{m}\int_{E_a}^{\infty} \sqrt{E}F(E)dE \qquad \text{Eqn 5.6}$$

Alternatively, the plasma beam can be allowed to pass through the analyser into a mass analyzing chamber. This allows for constituent and partial pressure determination of the molecular beam.

The energy analyser designed and built in house is shown in figure 5.18 (a). The supporting body of the analyser is an aluminum cylinder with the center machined out. This is designed to fit within the barrel of a KF 40 T-piece connector. The nickel wire mesh grids of 50 lines per inch used are attached onto aluminum machined frames (figure 5.18(c)) by means of silver paint. Each grid is electrically isolated with nylon spacers designed for the application (figure 5.18 (b)). The grids are locked in place with two screws that secure the 4 grids to the support body. Figure 5.19 shows photographs of the analyser assembled and placed within the T-piece.

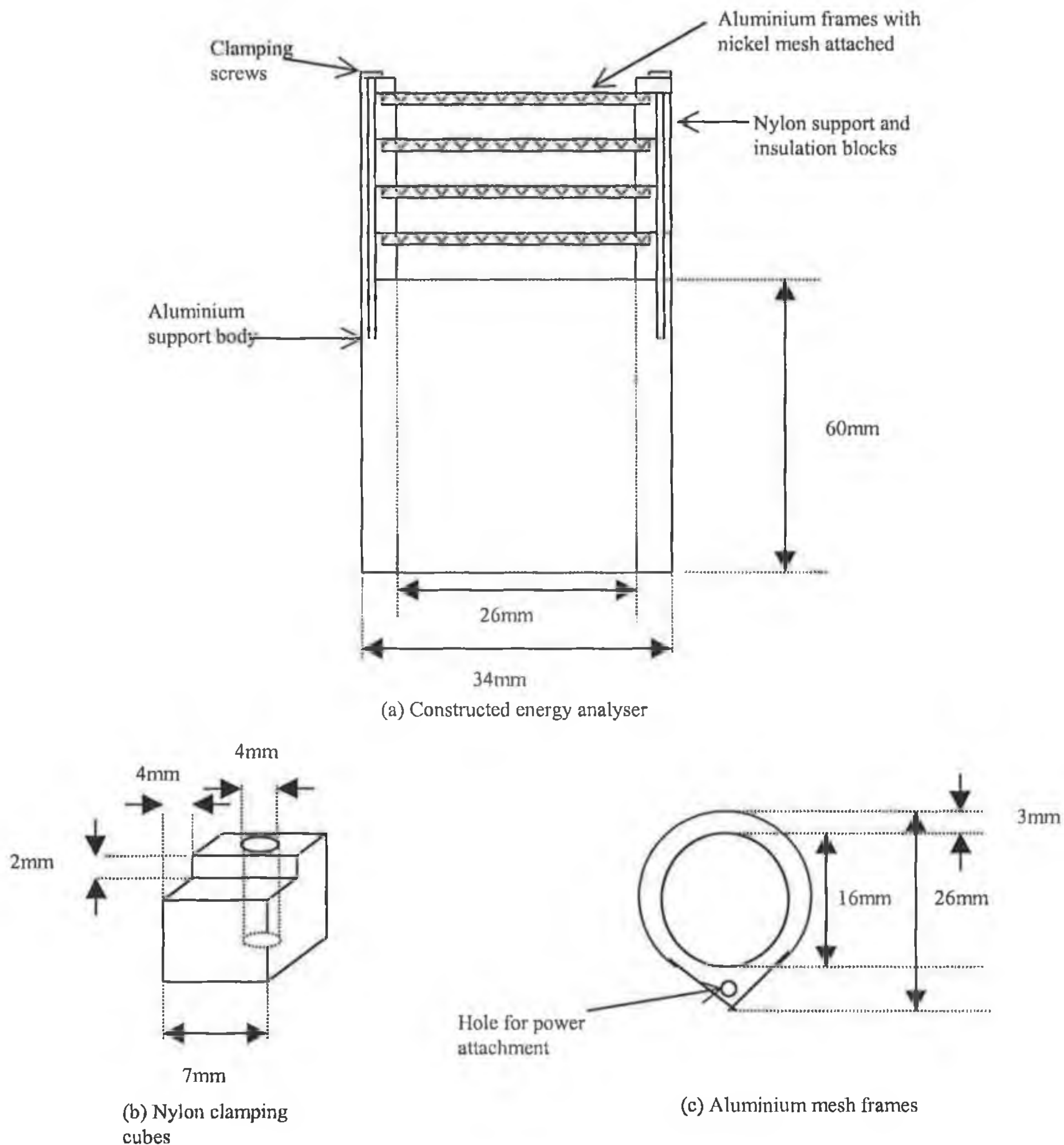

Figure 5.18 Design of an energy analyser (a) overall schematic of the assembled piece and (b) detail of the insulation and support blocks along with (c) the aluminum machined mesh frames.

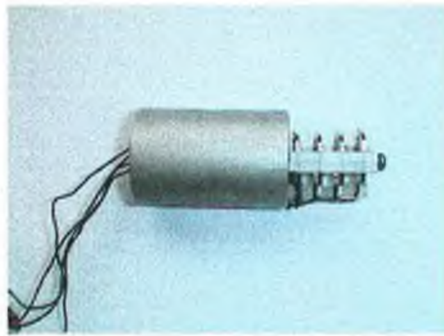

Figure 5.19 Photographs of the analyser assembled and situated in the CF40 T-piece ready to be attached to the chamber.

5.9.2 Mass Analyser

The mass analysis of particles in the analyser chamber is carried out by a quadrupole mass analyser, which is mounted in a CF40 T-piece configuration. A Balzers turbo pump, which can pump to 50 liters per second, is attached to the T-piece in order to evacuate the mass analyser chamber below E-4 Pa. This turbo pump is backed by an Edwards' high vacuum mechanical rotary pump. The mass chamber is isolated from the energy analyser and main chamber with a MDC high-pressure gate valve. The quadrupole is connected via a RF head to the controller unit mounted on the electronics rack.

5.9.3 Pressure Control

The control of pressure in the analyser chamber is an important factor in the resolution of the detector system. Numerous factors must be taken into account including process chamber pressure and pumping speed in the analyser chamber. It is important to note that the quadrupole must operate in the background pressure of E-4 to E-6 Pa while still receiving a representative sample from the plasma source. The result is an aperture in the wall plate between the process chamber and the analyser. The dimensions of this aperture are calculated with the following formula for single stage differential pumping.

$$P_1 = \frac{P_0 11.61 \pi d_1^2}{4S_1} \qquad \text{Eqn 5.7}$$

where P_1 and P_o are the pressures in the analyser and the process chambers respectively, d the diameter of the aperture and S the pumping speed in the analyser chamber.

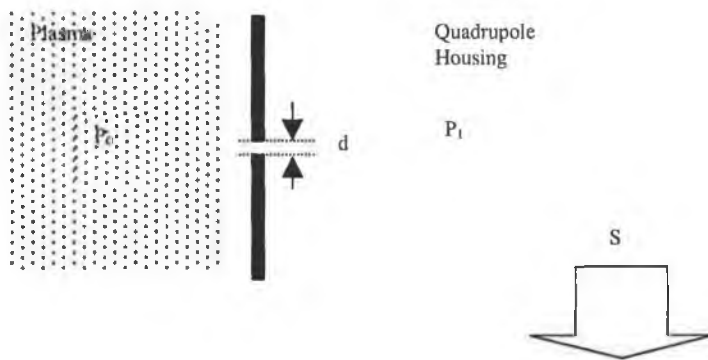

Figure 5.20 Illustration of single stage differential pumping

With the size of the analyser designed so as single stage pumping is adequate, as illustrated in figure 5.20 above, the task is somewhat simplified due to reductions in both the plasma beam diameter and the distance between the quadrupole and source. This helps to reduce collisions and ion loss to the walls.

With P_0 typically between 0.2 and 1.5 Pa and due to the necessity for P_1 to be in the E-4 Pa range, the calculations result in the combinations given in table 5.2 below.

P_0(Pa)	P_1(Pa)	d (cm)
0.4	7E-4	0.095
0.4	1.4E-4	0.033
0.6	7E-4	0.074
0.6	1.4E-4	0.024
1.2	7E-4	0.052
1.2	1.4E-4	0.018

Table 5.2 Calculation of aperture diameters for different levels of P_0 and P_1.

With the aim being to keep the sample large enough for adequate flux measurements, the pressure in the analyser chamber was typically kept between 1E-4 and 1E-3 Pa. For processes carried out at 0.4 Pa then a 1mm aperture was used. For process pressures near 1.2 Pa an aperture of 0.8mm should be used.

5.9.3.1 Aperture Design

The design of the aperture especially when dealing with such small diameters is important. To ensure a meaningful sample is extracted from the test volume the aperture must be designed to act as an effusive source. When this is achieved the composition of the plasma beam is the same as the plasma body. In order to satisfy effusive conditions it is necessary to ensure that an atom, ion or molecule can leave the source and pass through the aperture into the analyser region without making any collisions.

This can be achieved by putting

$$\frac{\lambda_0}{d} > 10 \qquad \text{good limit}$$

or, more usually,

$$\frac{\lambda_0}{d} > 1 \qquad \text{approximate limit}$$

where λ_o is the mean free path at the pressure P_o.

It can be estimated that the mean free path of plasma beam constituents is in the region of 1cm at 0.4 Pa. Therefore it can be written

$$\lambda_0 p_0 = 3x10^{-3} torrcm$$

This gives a new limitation on *d* that can be written as

$$d < \frac{(0.1 - 1.0)x3x10^{-3}}{P_0} cm$$

The apertures in use satisfy this condition.

A second condition is the thickness of the plate that contains the aperture must be as thin as possible so as to reduce collisions at the edge of the aperture. As the plate thickness increases the molecular beam density distribution changes due to collisions. Thus, the forward intensity changes but more importantly for the active species the surface collisions can change the measured beam composition dramatically. The number of collisions[4], P, can be calculated from

$$P = \frac{4s}{d} \qquad \text{Eqn 5.8}$$

where s is the plate thickness and d the aperture diameter.

In order to reduce collisions the aperture holes have been drilled in thin aluminum discs. These discs have then been machined down in the center to give a thin wall effect between the process chamber and the analyser. The discs are clamped in a slot machined in the chamber wall plate. Figure 5.21 illustrates the design.

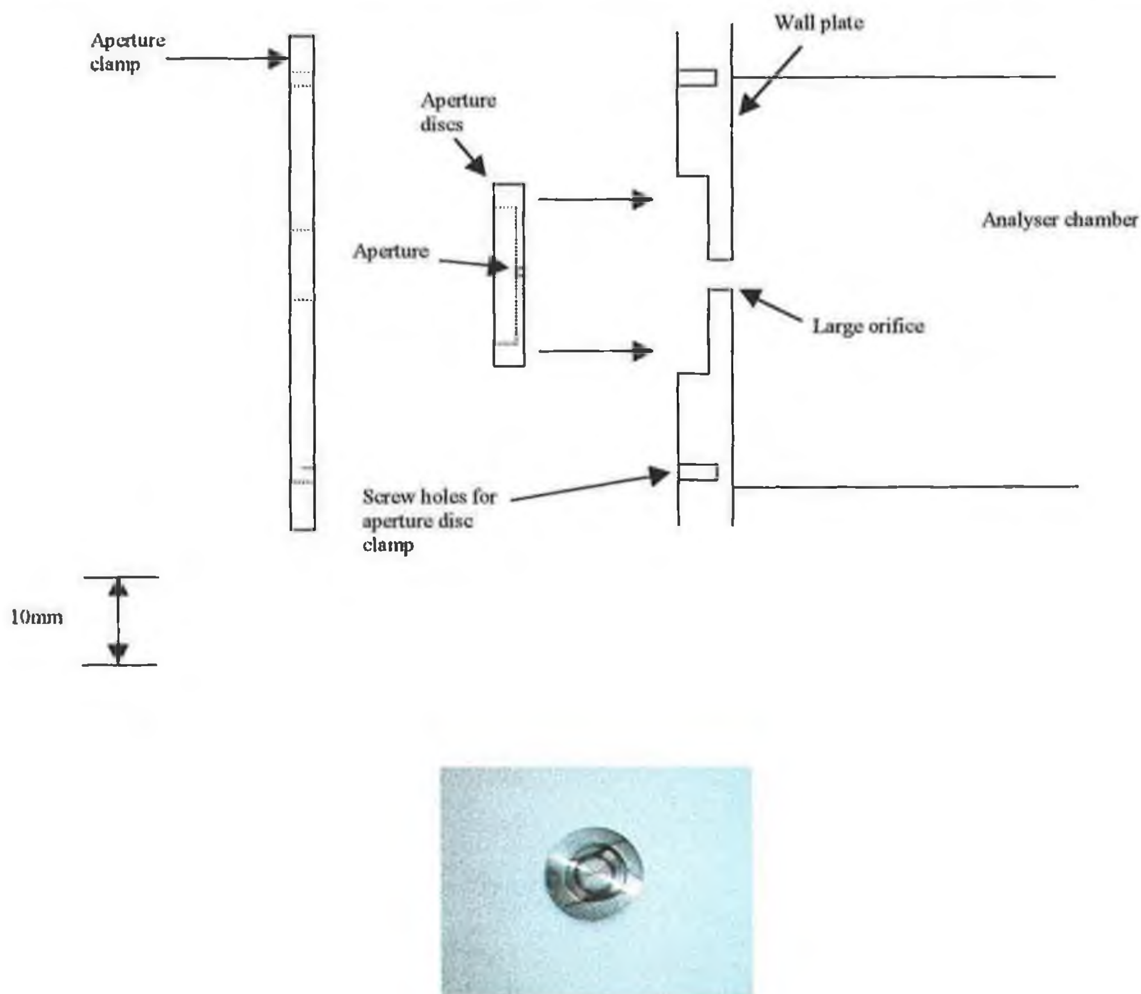

Figure 5.21 Illustration of the aperture disc installation to the chamber wall plate and a photo of one of the apertures used.

5.10 Electrical and Thermocouple Wiring

Wiring required for the internal chamber components includes target power connection, anode grounding connection and thermocouple connection. These are accomplished with the use of a multipoint electrical feedthrough.

The power connections for the solenoid are passed through a PTFE tube to the cathode body. A rubber feedthrough was then fabricated from a viton o-ring for the wires to pass through so the target cooling water pressure is not lost through this port. This design is illustrated below in figure 5.22.

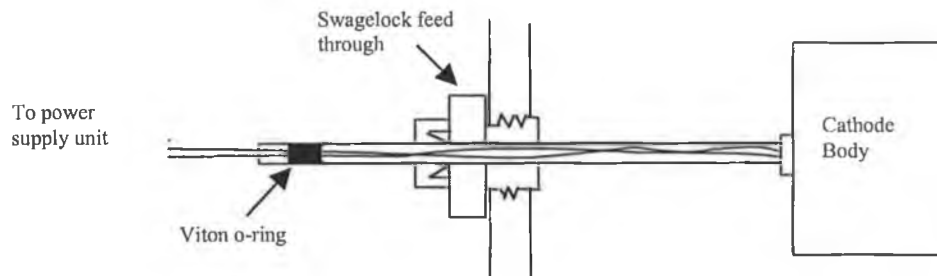

Figure 5.22 Solenoid power feedthrough.

The thermocouple and anode grounding wires are passed through the nylon support rings and up the rear of the anode electrode as shown in figure 5.23 below. The wires are taped down with aluminum foil so as not to be etched by the plasma. The ground wire is attached to one of the four anode supports via a removable wire clamp and the thermocouple is taped onto the rear of the anode with a poly-bromide high temperature tape. The thermocouple is protruded out a machined hole on the anode and placed touching the sample. This way the sample surface temperature that is recorded is done so at the same point for all samples taken.

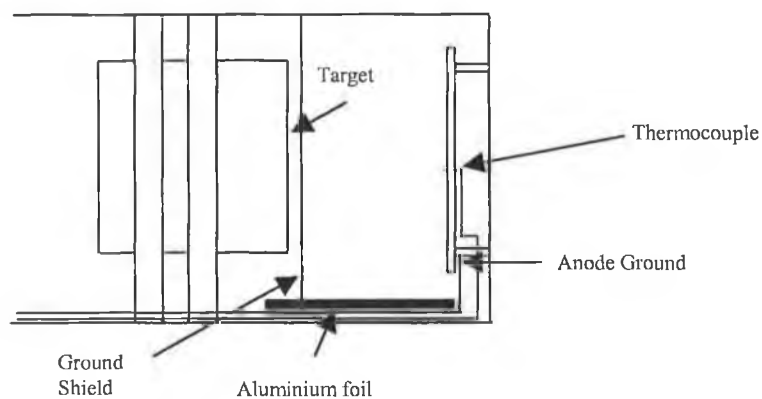

Figure 5.23 Illustration of the electrical wiring to the anode

Chapter Five Reference

[1] D. Ball, J. Appl. Phys. 43, (1972) 3047.

[2] J. Vossen and W. Kern, Thin Film Processes, Academic Press, New York (1978) p140.

[3] M. Murphy, D. Cameron, and S. Hashmi, J. Vac. Sci. Technol. A 13(4) (1995).

[4] Hiden Analytical, Handbook of Plasma Diagnostics, Hiden Analytical, Warrington (1986).

[5] M. Sugawara, B Bergevin, B Stansfield, and B Gregory INRS, Energie Rapport Interne, Number 033 (1970).

Chapter Six

Magnetic Field Analysis

6.1 Introduction

The design of a successful magnetron sputtering system depends heavily on the design of the magnetic field that enhances the sputtering at the target. In order to achieve efficient magnetron sputtering the field is best normal to the target surface as it intersects it. This is usually accomplished by placing the magnetron close to the target rear and by making sure that there is equal spacing between the outer and inner poles.

In order to analyze the field produced a mapping system must be used. This mapping system enables the field to be measured at discrete points and then modeled within a polar system. From this, representative field lines can be plotted on a 2 dimensional plane that represent the cylindrical shape of the field. By using this system the effects of varying the magnetic field balance can be seen more clearly, and can be related directly to the variation in results and deposition conditions of the grown films.

6.2 Field Mapping

In order to show the effect of varying the magnetic field balance between the inner and outer poles the field has been measured at discrete points in the radial (r) and in the axial (z) directions with a F.W.Bell gauss meter (model 4048). These measured values can be represented using vector arrows with lengths proportional to $1+\log|B|$ so as the field at increased distances from the target may be represented. The co-ordinates along with the vector components can be programmed into Matlab and graphically represented as will be shown in section 6.3.

A mapping technique developed by Kadlec and Musil[1] in 1995 to model magnetron fields has been employed and adapted for the application at hand. This technique requires using both the measured field vectors described above (B_r,B_z) and the discrete points (r,z) at which the readings were recorded. The field may then be fitted with Bessel functions. This was carried out with programs developed by the author using Excel and Matlab applications.

Due to the cylindrical symmetry of the magnetron and so the magnetic field induction **B**, solving Maxwell's equations under the following simplified[1] conditions can represent the field.

(1) The entire geometry is cylindrical and can be described by a radius r and an axial distance z. The magnetic field source also has cylindrical symmetry and is below the magnetron surface ($z \leq 0$).
(2) There are no time or heat variations of the currents and of the magnetic field.
(3) Modifications of the magnetic field by currents flowing in the magnetron discharge plasma are neglected.

We assume for Maxwell's equations that

$$\nabla \cdot B = 0 \qquad\qquad \nabla \times B = 0$$

The problem is now reduced to a magnetostatic problem at $z>0$ and so it is possible to find a scalar potential U, where

$$\mathbf{B} = \nabla U = \left(\frac{dU}{dr}, 0, \frac{dU}{dz} \right) \qquad \text{Eqn 6.1}$$

The function $dU/d\varphi=0$ because there is no function of the polar angle φ due to the cylindrical symmetry. Taking the Laplace transform for U we can then write

$$\Delta U = \frac{\partial^2 U}{\partial r^2} + \frac{1}{r}\frac{\partial U}{\partial r} + \frac{\partial^2 U}{\partial z^2} = 0 \qquad \text{Eqn 6.2}$$

The solution[1] can be expressed as a Fourier series of Bessel functions J_0, as a function of r, and an exponential decay as a function of z.

$$U = \sum_{i=1}^{\infty} \alpha_i J_0\left(\frac{l_i r}{r_0} \right) \exp\left(-\frac{l_i z}{r_0} \right) \qquad \text{Eqn 6.3}$$

where l_i is the ith root of the equation $J_0(l)=0$, so that $J_0(l_i r/r_0)=0$ for $r=r_0$. α_i is the ith coefficient of the series. For the magnetic field induction **B** we obtain the following from equations 6.1 and 6.3.

$$B_r = \sum_{i=1}^{n} a_i J_1\left(\frac{l_i r}{r_0} \right) \exp\left(-\frac{l_i z}{r_0} \right) \qquad \text{Eqn 6.4A}$$

$$B_z = \sum_{i=1}^{n} a_i J_0\left(\frac{l_i r}{r_0} \right) \exp\left(-\frac{l_i z}{r_0} \right) \qquad \text{Eqn 6.4B}$$

where the coefficient a is

$$a_i = \frac{\alpha_i l_i}{r_0}$$

From the discrete measurement points (r,z) and the radial and axial components of the magnetic flux measured at these points (B_r, B_z) the coefficients *a(i)* may be calculated. Equations 6.4A and 6.4B were programmed into Excel where the Solver and Analysis tool-pak are used to equate the Bessel functions and solve for the first five coefficients a_i[1-5].(See appendix D)

Once the coefficients *a(i)* are found for a particular magnetic field shape then any point of that field (r_i,z_i) may be calculated by using equations 6.4A, 6.4B and the equated coefficients *a(i),* which are constant for any one field configuration.

Field lines may then be calculated starting from any suitable point (r_1,z_1). Once *n* terms of equations 6.4A and 6.4B are calculated at (r_1,z_1) a vector may be plotted at that point which is a tangent to the field line in the direction of **B**. A suitable numerical method for differential equations may then be applied such as the Runge-Kutta or Euler formulae, so as the next point (r_2,z_2) may be calculated at a step size 'h' away. The process is repeated a user-defined number of times and a continuous field line may be plotted tangent to the field vectors.

This process was carried out in Matlab software with the coefficients a_i and the roots of the Bessel functions l_i set as constants in the program for a particular value of the solenoid current I_s. The couple (r_1,z_1) are entered at the start of the program and the field line is plotted from that point. By changing r_1 the next field line may be calculated and plotted. The step size *h* is an important constant for detailed field lines especially at low *r*-values as the B_r and B_z values here are typically the largest, and will so ultimately determine the field line direction. It is usually found through trial and error.
The field line plotting software program developed by the author is listed in appendix G.

6.3 Field Vectors

The discrete measurements of magnetic flux can be graphed so as the general field shape can be seen. Figure 6.1 shows vector arrows representing B_r and B_z measured with a gauss meter. The arrow lengths are proportional to 1+log|B| in order to observe the field at distant points. These values of (B_r,B_z) and (r,z) are the values used to find the coefficients *a(i)* in Excel.

Figures 6.1 (a) and (b) below were generated in Matlab with a software program developed by the author. The program developed for I_s=0.8A can be seen in appendix E. For other values of I_s the values of $r,z,B_r,$ and B_z can be entered in the appropriate arrays from Excel.

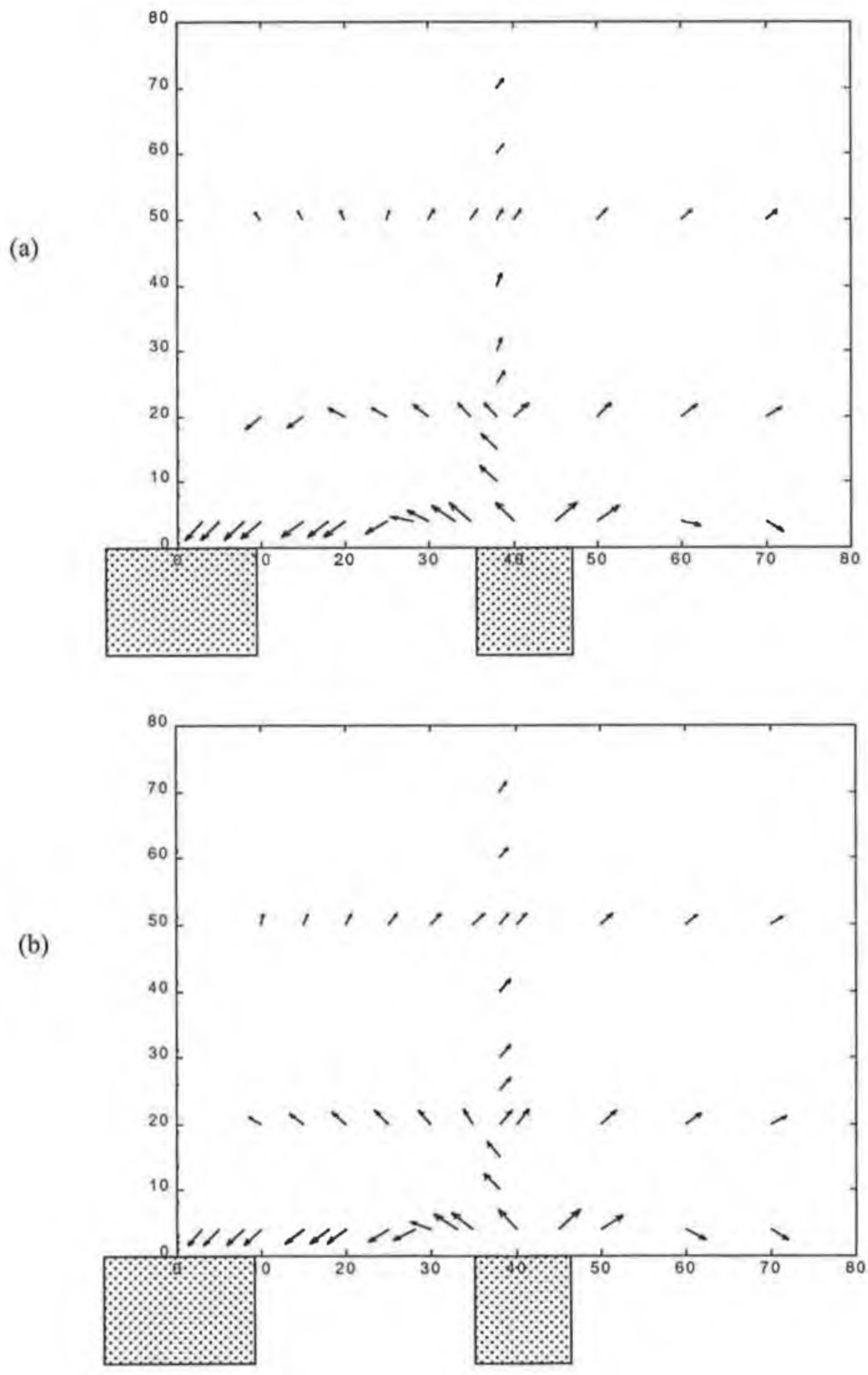

Figure 6.1 Vector arrow plots for (a) Is=0.8 Amps and (b) Is= -0.4Amps. The point (0,0) represents the center of the inner pole of the magnetron surface. The outer ring begins at r=37mm. The rectangles represent the magnetic poles of the magnetron as described in chapter 5.

6.4 Magnetic Field Shapes

The software developed by the author was used to plot the field lines of four magnetic field configurations. The difference between the fields plotted is the value of I_s, the current flowing through the solenoid which is the central pole of the magnetron placed behind the sputtering target. This magnetron configuration along with explanations on solenoid fields has been described in detail in chapter five.

The author has plotted fields with I_s having values of 0.8A, 0.4A, 0A and –0.4A. Field lines have been plotted starting at r-values of 36mm to 44mm in steps of 1mm. A second plot accompanies each solenoid current value and is the result of additional detail or flux lines calculated between the r-values where the field diverges from the central core towards the substrate. These field lines were plotted first at

$$r_{x1} = (r_n + r_{n+1})/2$$

If the field line from r_x converges to the central core then the second additional field line is calculated at

$$r_{x2} = (r_{x1} + r_{n+1})/2$$

or, if the field line meets the anode, then the second additional field line is calculated at

$$r_{x2} = (r_{x1} + r_n)/2$$

A third additional field line is then calculated. Again depending of the direction of the second additional field line.

For r_{x1} converging on the central core then,

$$r_{x3} = (r_{x2} + r_{n+1})/2$$

else

$$r_{x3} = (r_{x2} + r_n)/2$$

This technique is basically to show, in more detail, the split between the farthest reaching field line that intersects the cathode twice and the point at which the field diverges towards the anode.

Below in figures 6.2 to 6.5 are the four magnetic field configurations plotted.

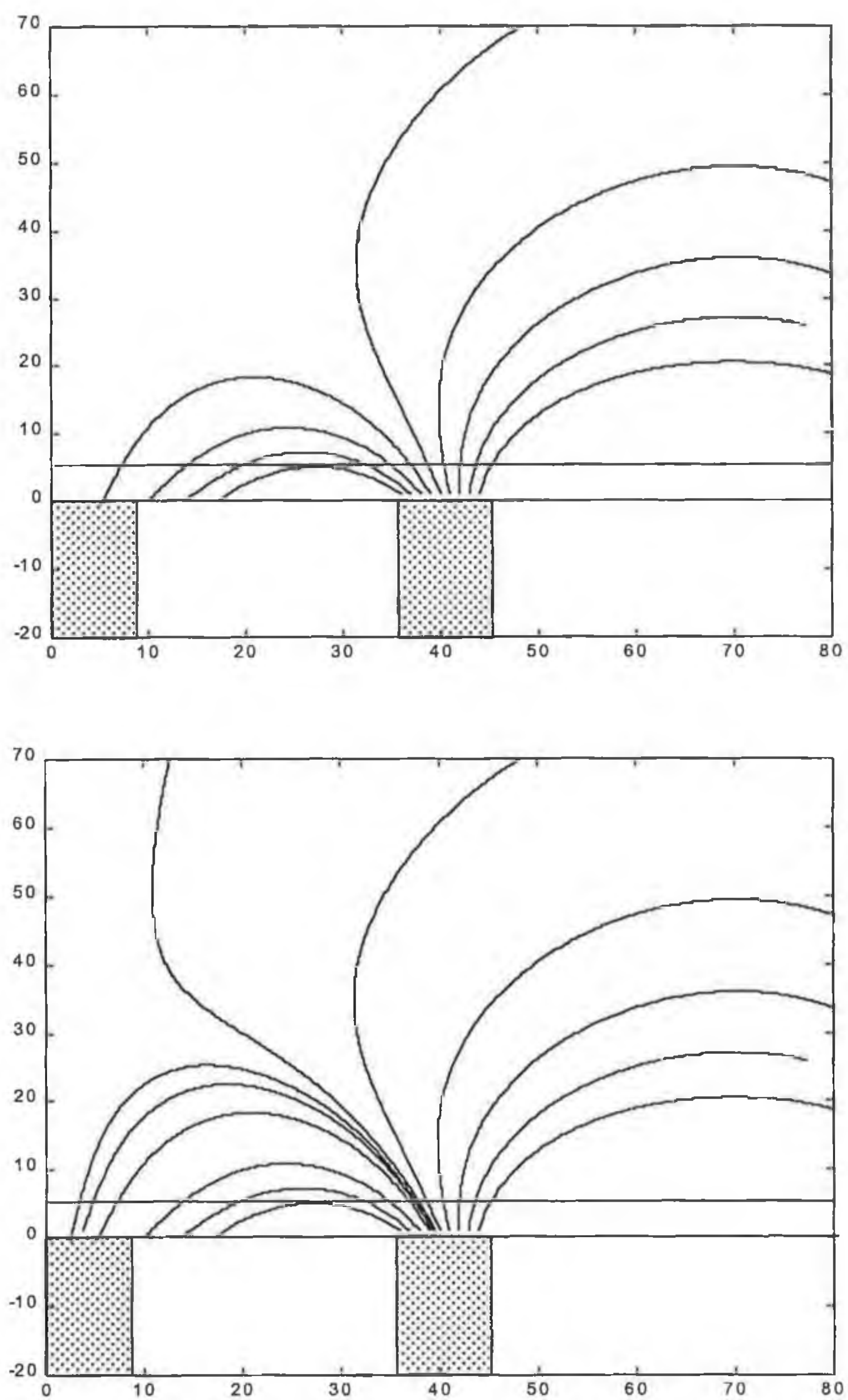

Figure 6.2 **Magnetic flux lines with I_s=0.8A. The farthest reaching field line that intersects the cathode twice can be seen extending to z=25mm.**

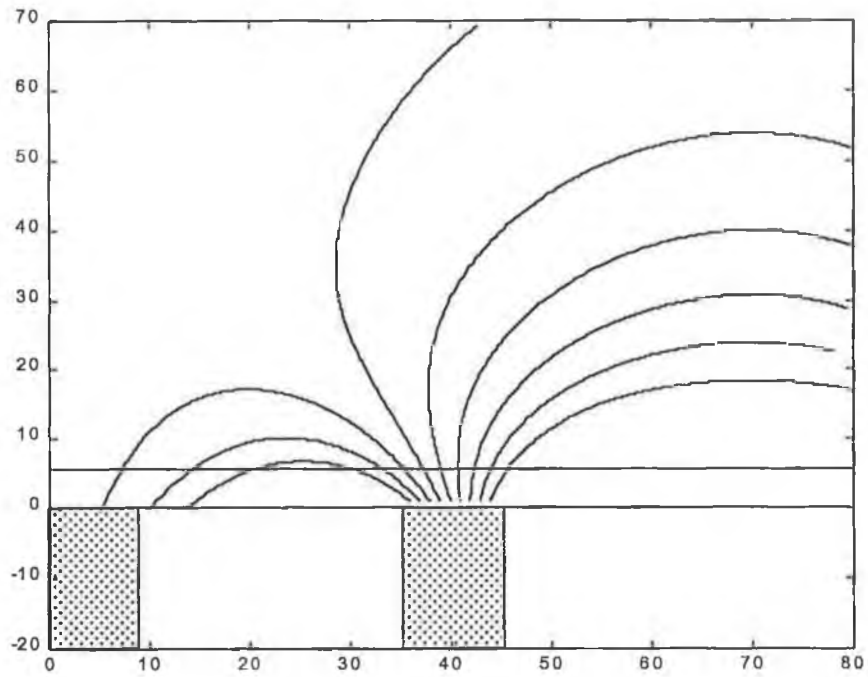

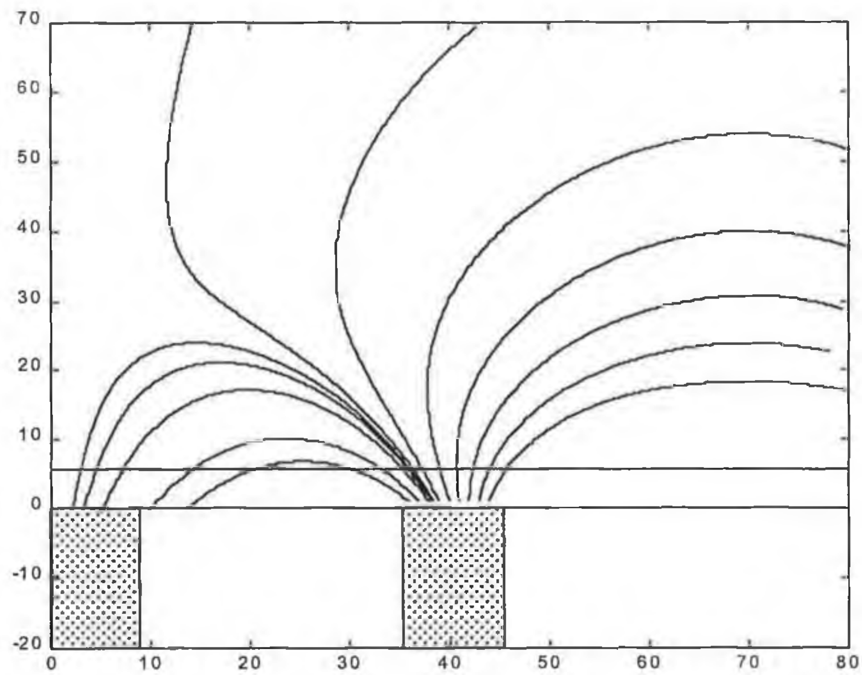

Figure 6.3 Magnetic flux line diagrams for $I_s = 0.4A$.

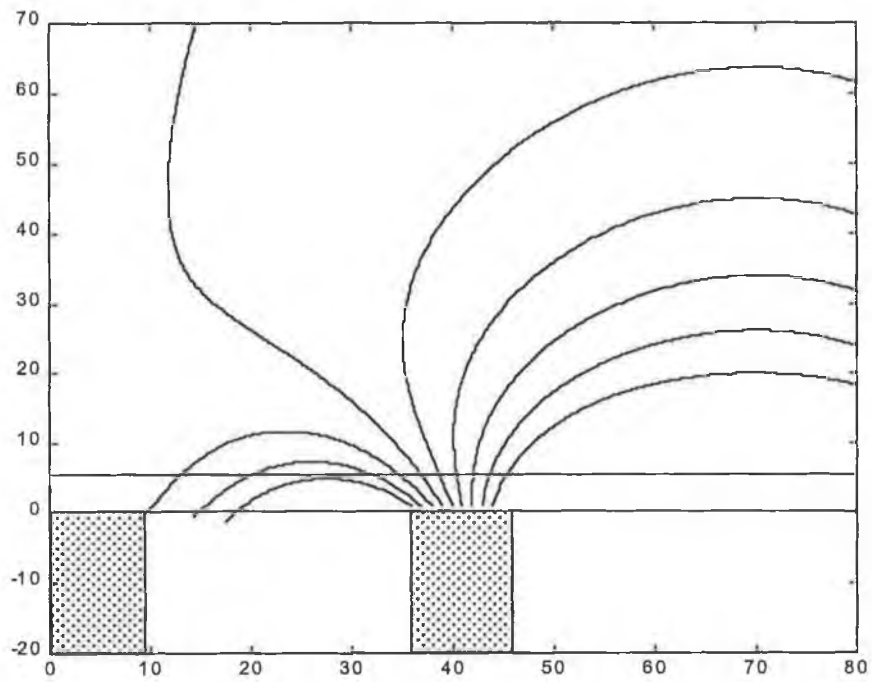

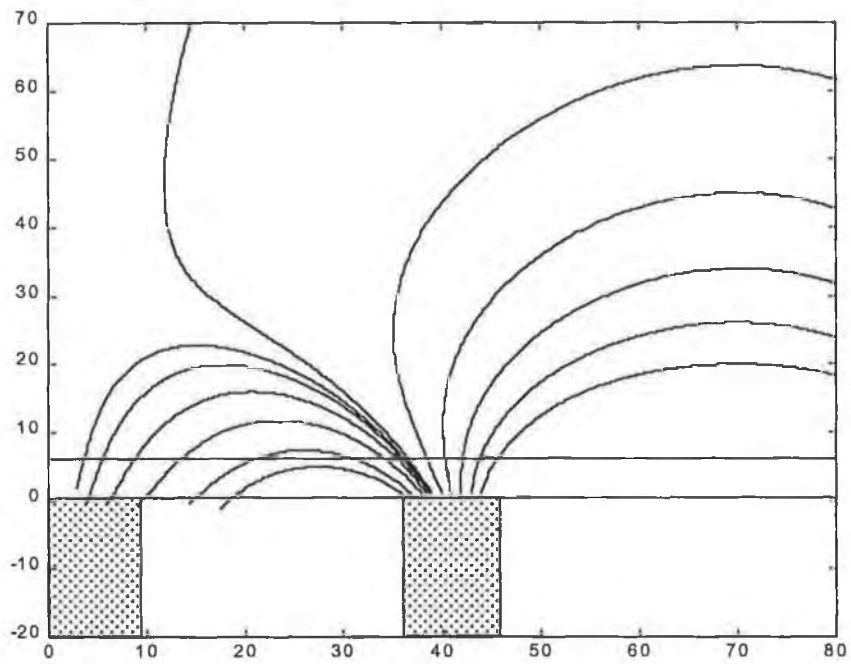

Figure 6.4 **Magnetic flux line diagrams for $I_s = 0A$.**

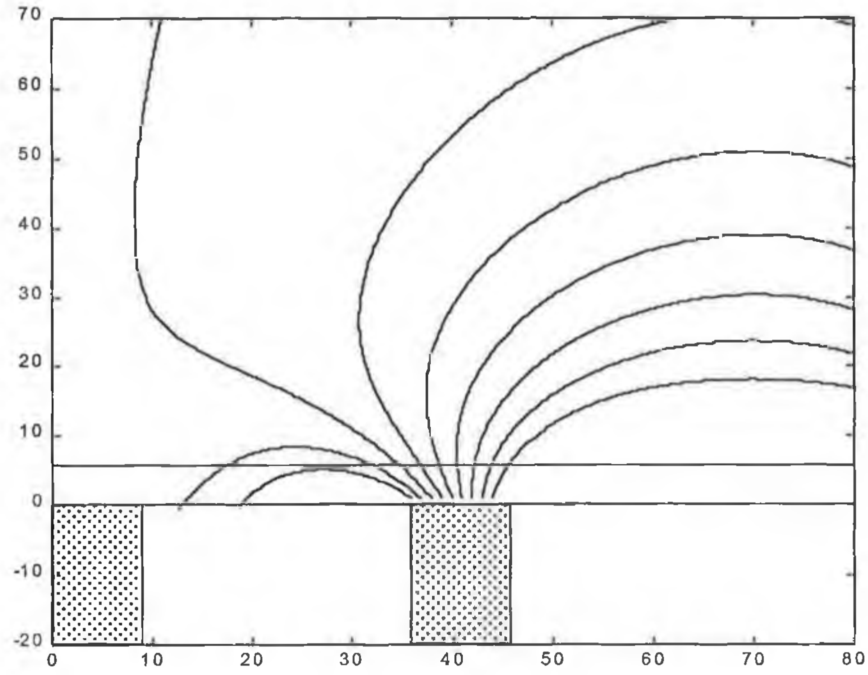

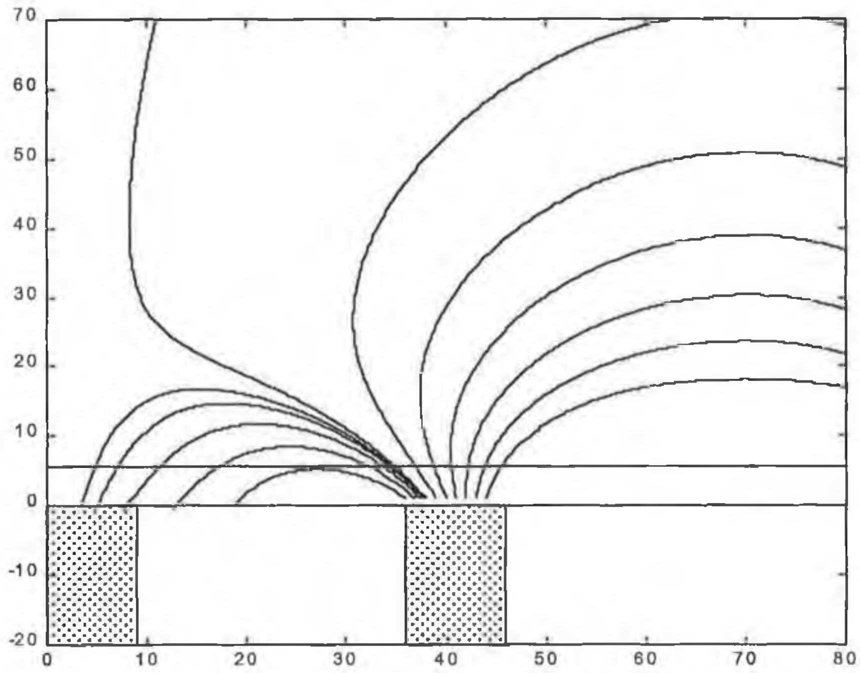

Figure 6.5 Magnetic flux line diagrams for I_s = -0.4A.

6.5 Field Analysis

It is important to note that the field maps are not directly related to or proportional to the strength of or flux density of the magnetic field. The mapping system allows the flux lines of the outer pole to be viewed relative to the other configurations only.

Initially, from looking at the field lines of the four configurations it might be thought that little difference can be drawn between them. However, when one uses the data gathered in chapter seven on target characteristics, the differences between the fields seems much more apparent.

Firstly is can be noted that the racetrack which is eroded on the target corresponds well with the field lines plotted on all of the field figures above. As would be expected the deepest part of the racetrack is located at approximately *r*=28mm from the target center. Reasons for this are obvious, as the low (z) field lines typically have the strongest parallel component of the field, B_r. As *r* reduces to zero the racetrack reduces in depth until it is nearly at the original thickness at the center of the target (*r*=0).

At I_s=0.8A the field in the solenoid causes a large proportion of the flux from the outer pole to be attracted towards the central pole. When extra detail is revealed in the second diagram it shows a divergence toward the anode at *r*=39.5mm. At the target surface high electron capture is feasible and as a result low irradiation levels can be expected at the anode (The anode or substrate holder is not represented in the field maps but has its center situated at *z*=57mm (target to substrate distance of 50mm)).

When I_s=0.4A the field looks similar. The main difference that can be seen is the change in direction of the fourth field line from the central pole at I_s=0.8A, now towards the anode. The result of this is that the flux at the anode has increased, but electron capture due to the first three field lines proves adequate to have the target operate at the same voltage for both values of I_s. Judging from the field alone one could postulate that ion and electron irradiation of the anode should be of a similar magnitude, with deposition rate and conditions due to both solenoid currents also being similar.

At I_s reduced to 0A it can be noted that the fourth field line has shifted to a lower r-value. It also can be seen that the field lines on the right of the outer pole have shifted up and are beginning to firstly sway to the left into the main plasma body and then right. These shifts are obviously due to the elimination of the solenoid current but represent a reduction in magnetic flux towards the central pole and to increased flux density at the anode. An increase in the target operating voltage would be expected in order to sustain the discharge. This is mainly due to increased electron loss to the anode caused by the increased flux density extending from the magnetron outer pole to the anode electrode.

In the final field plot with I_s = - 0.4A it can be seen from the first figure that the third field line that converged towards the central pole in the previous figure now extends to the anode. With the additional detail added in the second diagram it can be seen that the extension of the furthest reaching field line, that intersects the cathode twice, has been significantly reduced from z= 22 to 23mm down to about 16mm. Now that the divergence of the field lines is reduced to about r=37.8mm, the result is a further increase in magnetic flux density at the anode electrode. Once again an increase in voltage would be required to sustain the discharge due to higher amounts of electron current escaping from the magnetron discharge. Consequently, increased substrate temperature during deposition should be evident.

Chapter Six References

[1] S. Kadlec and J. Musil, J. Vac. Sci. Technol. A 13(2) (1995) 389.

[2] E. Kreyszig, Advanced Engineering Mathematics,7th Ed, Wiley, New York (1995) Chapter 20.

[3] I.S. Grant and W.R. Phillips, Electromagnetism, Wiley, Bristol (1982).

[4] P. Hammond, Electromagnetism for Engineers, Pergamon Press, London (1985) Chapter 6.

Chapter Seven

Results

7.1 Introduction

Once the sputtering system was designed and constructed by the author, a test and evaluation period was carried out in order to monitor and record the deposition characteristics of the system. Initially, target characteristics such as voltage and power were measured at constant current settings as a function of solenoid current. Deposition rates of the fabricated aluminium target were then measured at different process pressures, again as a function of the current running through the solenoid. These characteristics are reported below.

Once the operational and performance characteristics were carried out the analyser chamber was set up. Measurements of species impinging upon the substrate were recorded in terms of their energy and mass as a function of solenoid current. These results are also reported on and evaluated for their effects on the films growth.

7.2 Target Characteristics

The target was operated by an Advanced Energy Magnetron Driver in constant current mode at a value of 500mA, as discussed in chapter five. At this current, the voltage and power of the target were recorded during deposition and plotted against the solenoid current, which was kept as the only variable parameter in the deposition process. Evaluations were carried out at two process pressures, 0.4 Pa and 1Pa (3mTorr and 7.5mTorr). These results are reported on below in figures 7.1 and 7.2.

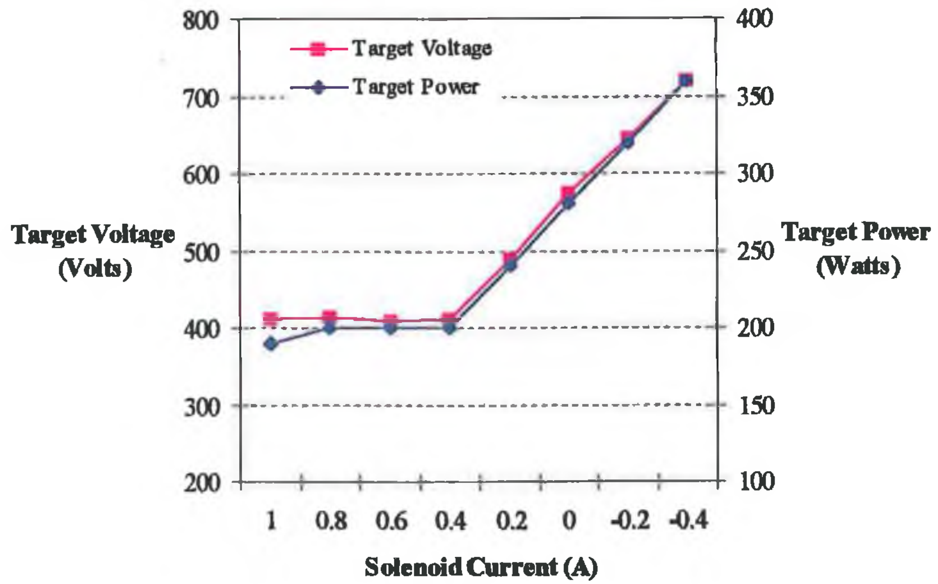

Figure 7.1 **Target power and voltage characteristics as a function of solenoid current at 0.4 Pa**

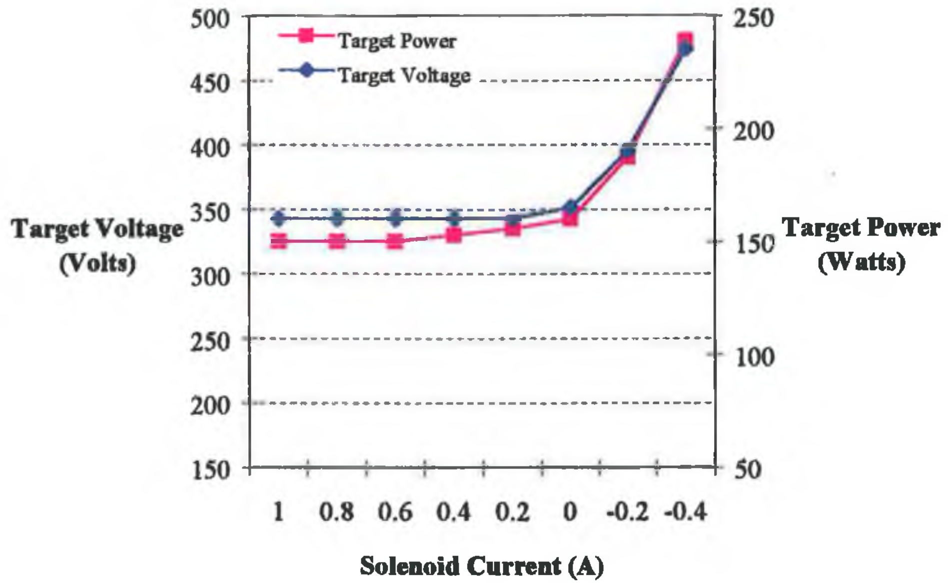

Figure 7.2 **Target power and voltage characteristics as a function of solenoid current at 1Pa**

It is obvious from figures 7.1 and 7.2 above that the voltage required to sustain the discharge is directly related to the solenoid current and process pressure. At each pressure, as the solenoid current reduces to zero and below, the voltage requirement increases and correspondingly, the power running from the target increases. This voltage increase can be directly related to the solenoid current. As reported in chapter six, the effect on the field of the outer pole of the magnetron, as the solenoid current is reduced, is an increase of magnetic flux away from the target surface. It has been noted that the furthest reaching field line that intersects the cathode twice is reduced significantly, and so as a direct result, the capture volume for secondary electrons that are emitted from the target is reduced. Due to this, more secondary electrons are required in the magnetron discharge so they can form more argon ions to sustain the discharge current at 500mA. Due to a dependency of secondary electron emission γ on incident ion energy[1], increasing the energy of $^{40}Ar^{+}$ ions bombarding the target satisfies the increase required in secondary electrons. This increase in argon ion energy comes about from the increases in target operating voltage measured.

The voltage and power differences measured between the process pressures is mainly due to the number density of the background gas at those pressures. In effect, at a lower pressure the ionization probability of secondary electrons is lower due to a larger mean free path. Therefore, as the target needs the same flux of bombarding argon ions to operate at 500mA, the operating voltage needs to be greater at a lower pressure. This larger voltage produces more secondary electrons upon ion bombardment[1] (greater energy) so as more argon ions may be formed from secondary electron-neutral collisions.

7.3 Deposition Characteristics

In order to characterise the unbalanced magnetron system, depositions were made on substrates at anode ground potential at both pressures and again with varying solenoid current. Films were grown on pre-cleaned polished silicon slides typically measuring 4cm^2. The substrates were oven baked for over four hours and then blown with nitrogen before being clamped to the anode ready for deposition. All samples were grown at the same position on the anode, at a target to substrate distance of 50mm and again at a constant current of 500mA.

Measurements of film thickness were carried out using a Tencor Sigmascan® and generally taken at the same place across all samples, so as the thickness measurements are relative to one another and to the target position. Figure 7.3 and 7.4 show the results obtained for film thickness.

Deposition temperatures of the samples taken were measured and can also be plotted as a function of solenoid current. The temperatures are again all taken from the same point on the substrates and read after 10 minutes of deposition. Measurements were taken in milli-Volts by a mineral insulated welded tip type K thermocouple and converted to degrees Celsius with the calibration chart for the TC.

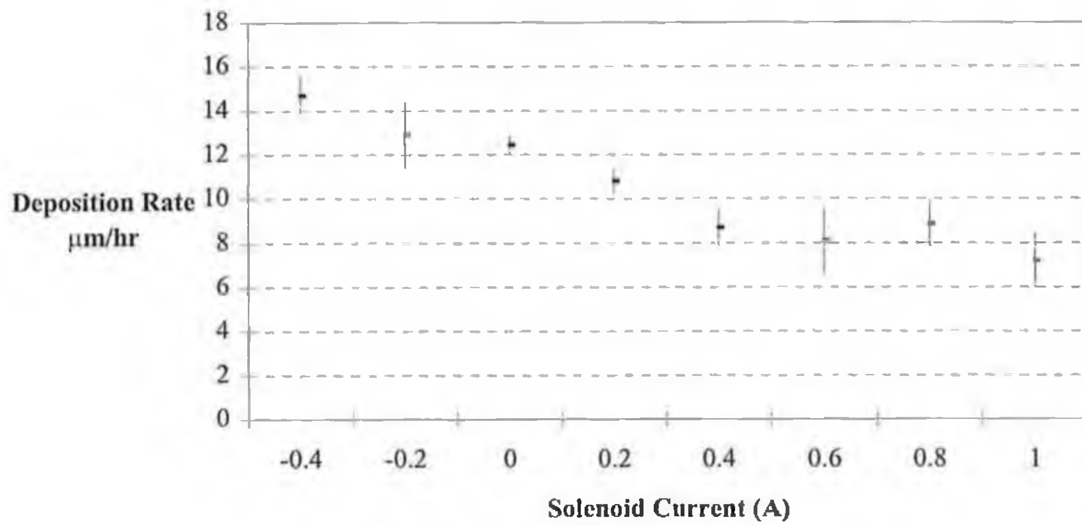

Figure 7.3 Deposition rate versus solenoid current at 0.4Pa

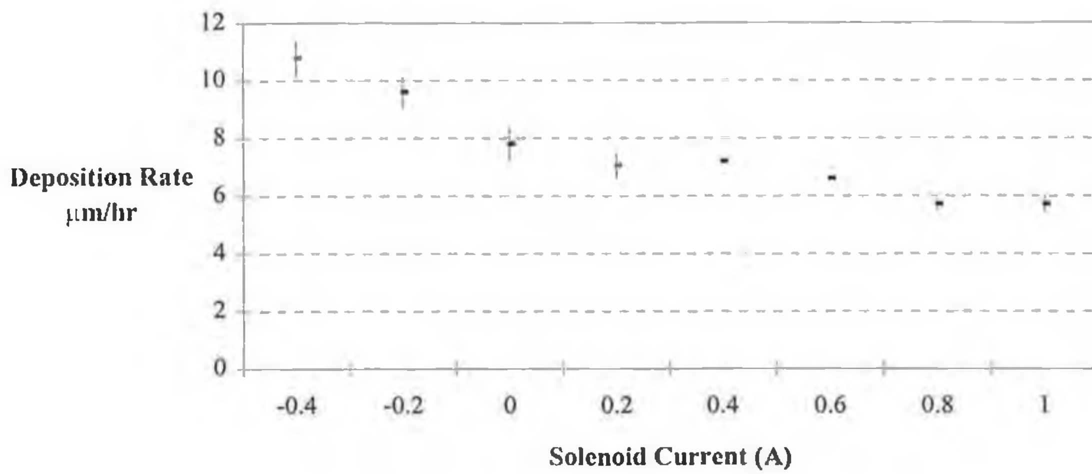

Figure 7.4 Deposition rate versus solenoid current at 1Pa

From the deposition rates recorded at 0.4Pa and 1Pa an interesting trend can be seen, the deposition rate increases with decreasing solenoid current for the same discharge current. Operating the target at constant current ensures that the same flux of argon ions bombard the target surface. Due to the solenoid current decreasing, the flux of electrons escaping from the magnetron discharge increases. This increase can be measured as temperature increases at the substrate. The loss mechanism of electrons has been reviewed in chapter six with the magnetic field line plots. These electrons that are lost from the electron trap cause reductions in the number of ions produced from collisions in the discharge with argon neutrals. In order to sustain the discharge current the operating voltage of the target needs to increase as has been reported. Again, this is to produce increased numbers of secondary electrons from the target, which will produce argon ions. This target voltage increase results in an increase in the average ion energy that bombards the target. As the energy of the argon ions increases so to does the sputter yield for a particular target material. Figure 7.5 shows data collected by General Mills in 1962 for the sputter yield of aluminium in an argon discharge at varying levels of ion energy.

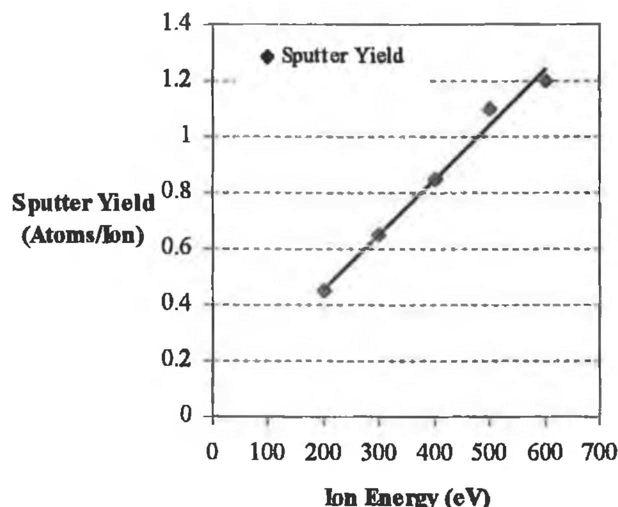

Figure 7.5[3] **Sputter Yield for Aluminium as a function of incident ion energy**

In summary it can be said that due to reductions in the solenoid current at each process pressure the target voltage increases causing a shift in the mean energy of the argon sputter ions. This ion energy increase results in an enhanced liberation of target atoms due to sputter yield dependency on energy. The increase in bombarding energy also results in an increase in the energy profile of the ejected target atoms[4], thus reducing the probability of an atom being thermalized before it interacts with a surface. In all this leads to increased deposition rates at the substrate but also causes an increased erosion rate of the target.

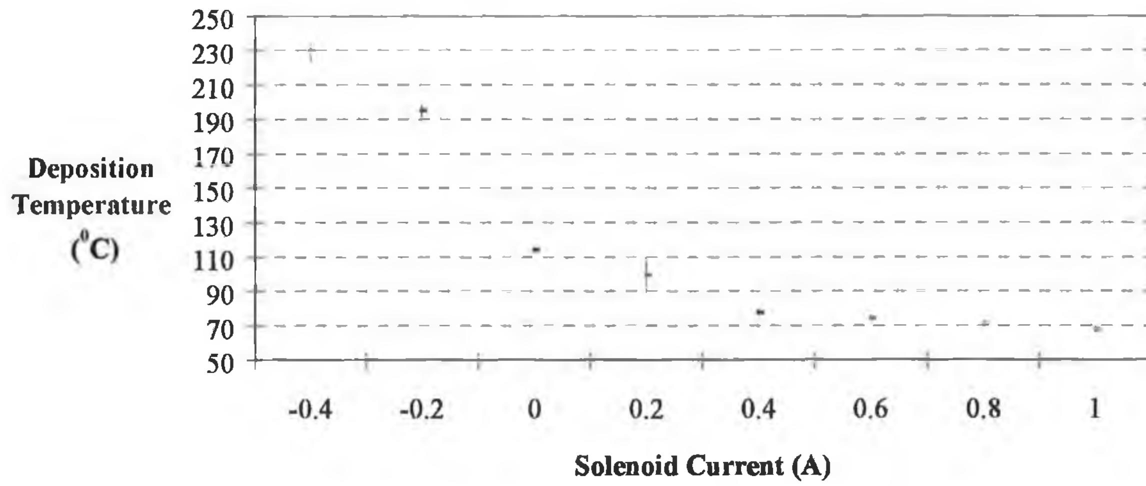

Figure 7.6 Deposition temperature versus solenoid current at 0.4Pa process pressure

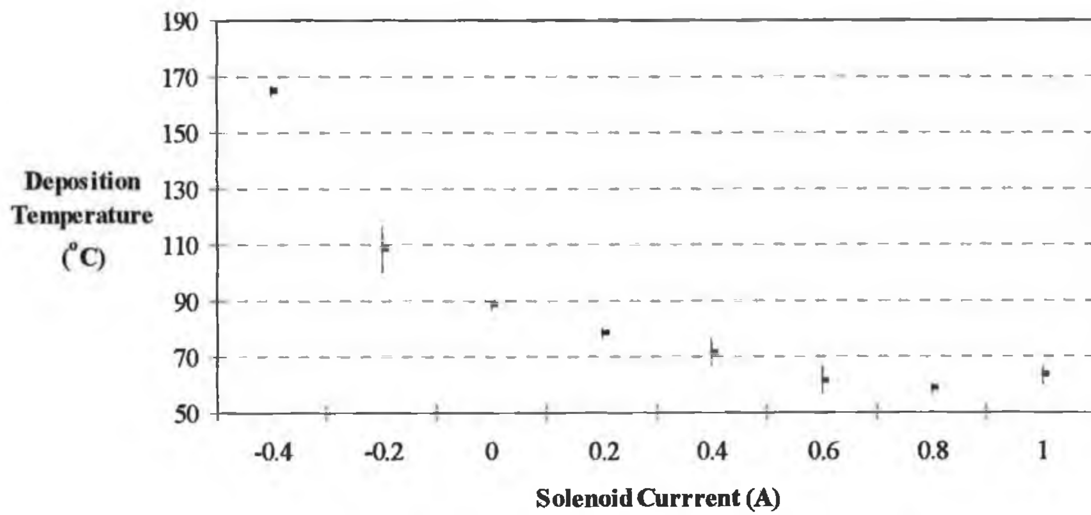

Figure 7.7 Deposition temperature against solenoid current at 1Pa process pressure

The temperature of the deposited film can also be plotted as a function of the solenoid current. This is represented in figures 7.6 and 7.7 above. The temperature increases measured are due to the increasing flux of argon ions, target atoms, argon neutrals and electrons bombarding the substrate as the solenoid current is reduced. These ion and electron currents dissipate most of their energy as heat upon collision, which will be reported on later, and bring about interesting effects on the film characteristics such as improvements in adhesion, microstructure and film hardness which have been discussed in chapter three on thin film growth. The author has also measured the flux of argon ions hitting the substrate, which can be illustrated with a number density as a function of energy. This will also be reported on later.

7.4 Adhesion

The adhesion of a film to a substrate is an important factor for many processes in IC manufacturing and for hard and protective coatings. Bad adhesion results in unreliable coatings that can cause cracking or separation of the film from the substrate. High stress content in films can also reduce adhesion due to buckling effects, while severe stress content leads to cracking in the film.

Adhesion properties are also very dependent upon deposition characteristics such as moisture content, gas purity, kinetic energy of the incident species and nucleation density. These effects have been discussed in chapter three.

In order to try and characterise any differences in adhesion between the samples taken the author has tried a peeling method using an adhesive aluminium foil tape. The tape was attached to an area in the

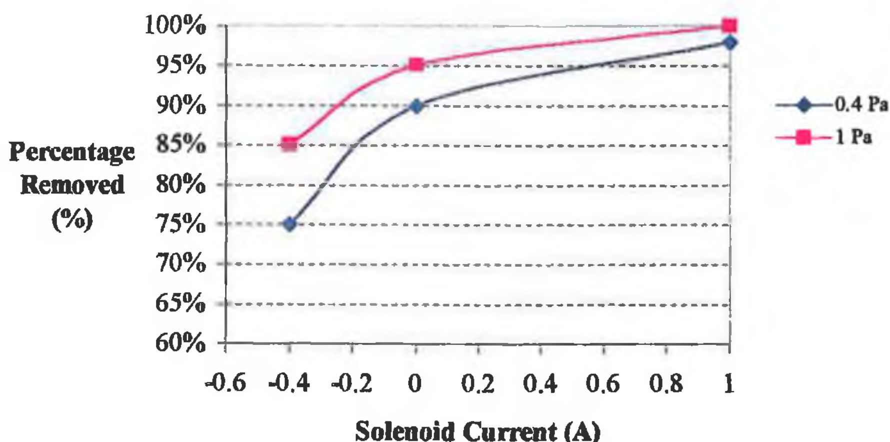

Figure 7.8 Comparison of sample adhesion varying with solenoid current at different process pressures

centre of the sample ($0.5cm^2$ typically), let to set for a few minutes and then peeled off at a moderate rate. The test was carried out on samples deposited at different solenoid currents and process pressures. Results gathered are shown above in figure 7.8.

Estimating exact percentages is difficult, but clear distinctions could be made between the amount of film removed by the tape for reducing values of solenoid current. This result was consistent at both process pressures. The results concur with increases in the sample deposition temperature as reported in the deposition characteristics and with increasing energy and flux of bombarding species which will be reported on in section 7.6. At a solenoid current of one amp and at both pressures almost the entire sample covered by the tape was removed. As the solenoid current is reduced the amount of film removed decreased, mainly towards the edges of the tape.

To summarise it can be said that the results show an increase of up to 25% in adhesion as the solenoid current is decreased and show a shift to enhanced adhesion as process pressure is reduced. In relation to the unbalance of the magnetron it can be said that increasing the degree of unbalance between the inner and outer poles results in superior film adhesion.

7.5 Microstructural Characteristics

To characterise the films microstructure the author has shown comparisons with Thornton's structural zone model[2], using the measured deposition temperature (T) in relation to the melting temperature of the target material (T_m) and the deposition pressure.

As the deposition temperatures are relatively low in comparison to production methods for thin films, the structural zones can only be related up into zone 2 at 0.4 Pa and into zone T at 1Pa. The structures of the films were tested for vertical strength with a Leitz miniload. After the indentation was made the films were then checked for cracking. All films were subjected to the same indentation made with a 5N load. Test results are shown below in figures 7.9 and 7.10 with micrographs.

At the 0.4 Pa process, the highest temperature (at a solenoid current of I_s= - 0.4A) recorded was approximately 240°C which has a T/T_m value for an aluminium target (T_m ~600 °C) of nearly 0.45. This film structure should be in zone 2, which is characterised by adatom diffusion and should show dense columnar grain growth with good mechanical properties. As I_s is increased, deposition temperature reduces and the film structure reduces to zone T which is characterised by a dense array of needle like fibrous grains which exhibit poorer mechanical characteristics. Further increases in solenoid current reduce the deposition temperature until zone 1 is reached. This region is characterised by tapered crystals that are poorly bonded.

In order to properly observe the indentations the films where looked at with a scanning electron microscope (SEM). The following micrographs were taken of the films grown at 0.4 Pa.

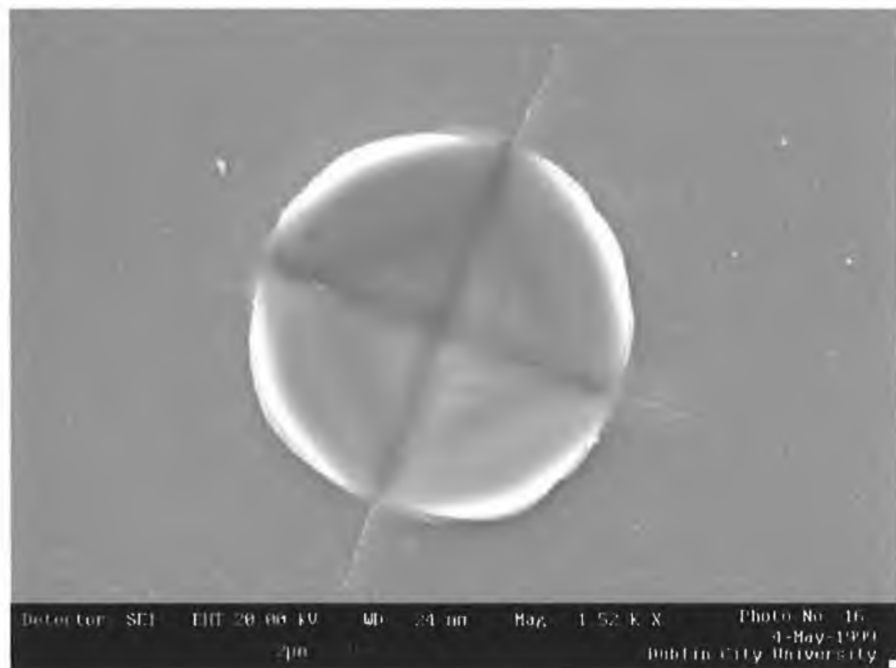

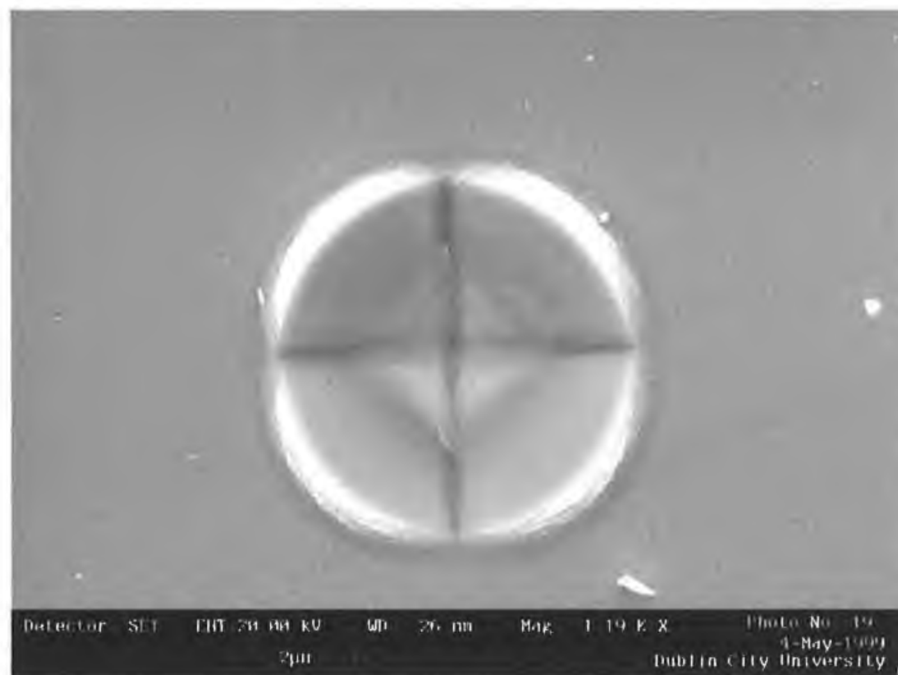

Figure 7.9 SEM micrographs of indents made with a Leitz mini-load on films deposited with I_s=0.8A (top) and I_s= - 0.4A (bottom) at a process pressure of 0.4Pa.

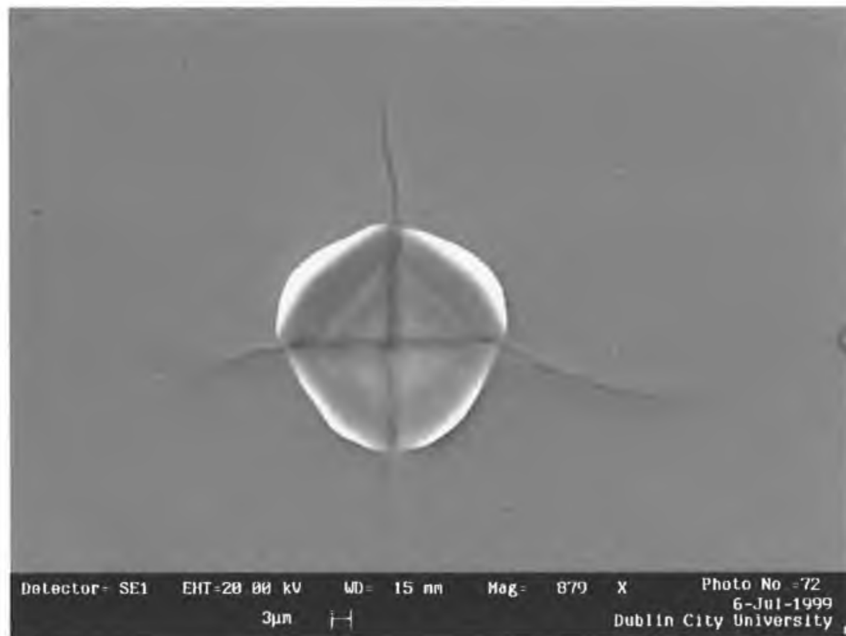

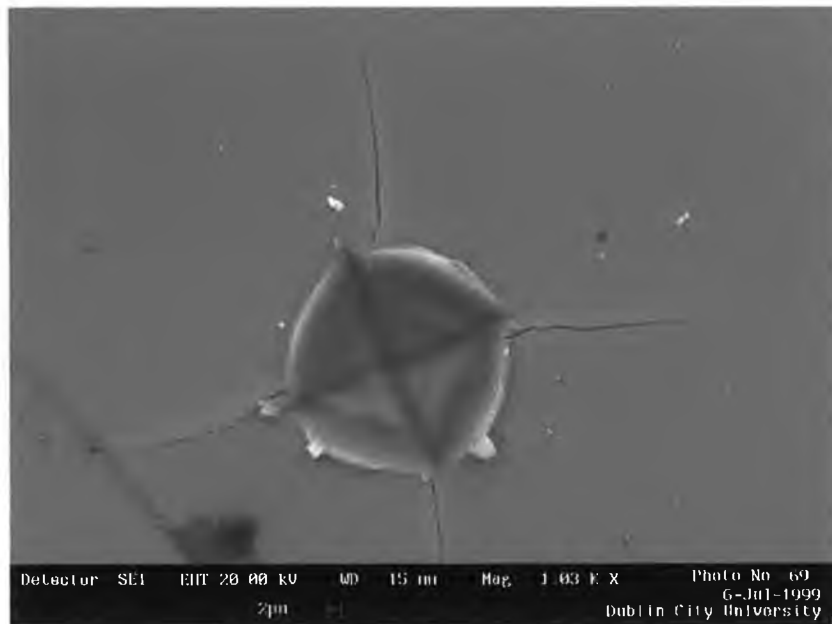

Figure 7.10 SEM micrographs of indentations carried out on films grown at 1 Pa with a solenoid current of (top) I_s=-0.4A and (bottom) I_s= 0.8A.

As can be seen from the differences between the 0.4 Pa micrographs in figure 7.9, the structural properties of these films have changed due to the current in the solenoid. The effects of temperature and the level of ion and electron bombardment during deposition have caused a shift from zone 2 to zone 1 microstructure at a constant pressure level. This is evident through the cracks seen on the film deposited at a solenoid current of 0.8A.

At a higher pressure of 1Pa an identical test procedure was carried out by using the grown films for indentation tests and reviewing the indents made with a SEM. The micrographs in figure 7.10 show the features observed.

It can be seen that cracking is evident at each value of solenoid current. At the highest deposition temperature for the 1Pa process the value of T/T_m is near 0.25 and so falls into zone T but is close to the zone 1 boundary. Again, this transitional microstructure is characterised by fibrous grains that are densely packed. The overall mechanical strength is poor due to voiding between grains and tapered grain ends. As temperature reduces with increasing solenoid current the structure falls into zone 1 which is characterised by poorly bonded crystals.
It is difficult to distinctly differentiate between the micrographs at each solenoid current. However, the cracks are longer and more profound on the sample deposited at a higher solenoid current.

As a general trend it can be said that the deposition temperature and the effects that cause temperature increases effect the microstructural characteristics of the grown films. The films with the highest deposition temperatures exhibit the best mechanical and structural characteristics. This effect reduces with increases in process pressure. This reduction is possibly due to the ratio of gas atoms to adatoms impinging upon the substrate, and also possibly because of the reduction in energy of the impinging species, which is again related to the gas number density.

7.6 Ion and Electron Bombardment

7.6.1 Introduction

The measurement of the most abundant ion species in the plasma ($^{40}Ar^+$) was carried out with the use of the energy and mass analysers. An effusive molecular beam can be extracted from the plasma for analysis as described in chapter five. In order to break the beam into energy and mass components the beam is first energy analysed by the electrostatic analyser constructed in house. The flux of ions with energy greater than that of the analysing potential V_A will have sufficient energy to pass through the energy analyser, and are detected by the mass spectrometer. The end result is an energy spectrum of the flux of argon ions bombarding the substrate during deposition.

The ion and electron currents (J_i and J_e) were also measured by changing a grid of the energy analyser to a collector plate. Saturation currents were measured with an electrometer by applying a negative or positive voltage for the appropriate species. The ion current J_i is assumed to be due to argon ions. Other species are known to be present in small amount such as Al^+ along with impurities.

7.6.2 Energy Analyser Set-up

The analyser was constructed with four grids so that numerous set-up configurations were possible for the analysis of any species. It was found through trial and error that for the analysis of argon ions no negative voltages were required to attract or accelerate the bombarding ions. A simple analysing voltage V_A applied to the four grids reduced the probability of ions with energy V_A and below getting through to the detector.

For the measurement of ion current the first grid of the analyser can be converted to a collector plate. This plate can then be put at an increasing negative potential until the current saturates. The aperture size (A_p) is known and so the ion current per unit area hitting the substrate can easily be calculated. To measure the ion current that collides with and is absorbed by the grid wires, the four grids can be connected together and grounded. This is important to measure so the fraction of the ion current that reaches the mass spectrometer is known and a calibration curve can be drawn to relate detected levels to ion flux. This is required as the mass spectrometer detection units are in Torr.

For the measurement of electron current a screen grid is required in front of a positively biased plate in order to capture secondary electrons emitted from the plate. This screen grid is held at –5Volts with respect to ground. The positive voltage is increased until the electron current saturates.
Figure 7.11 shows the set-up of the analyser for three different measurement techniques.

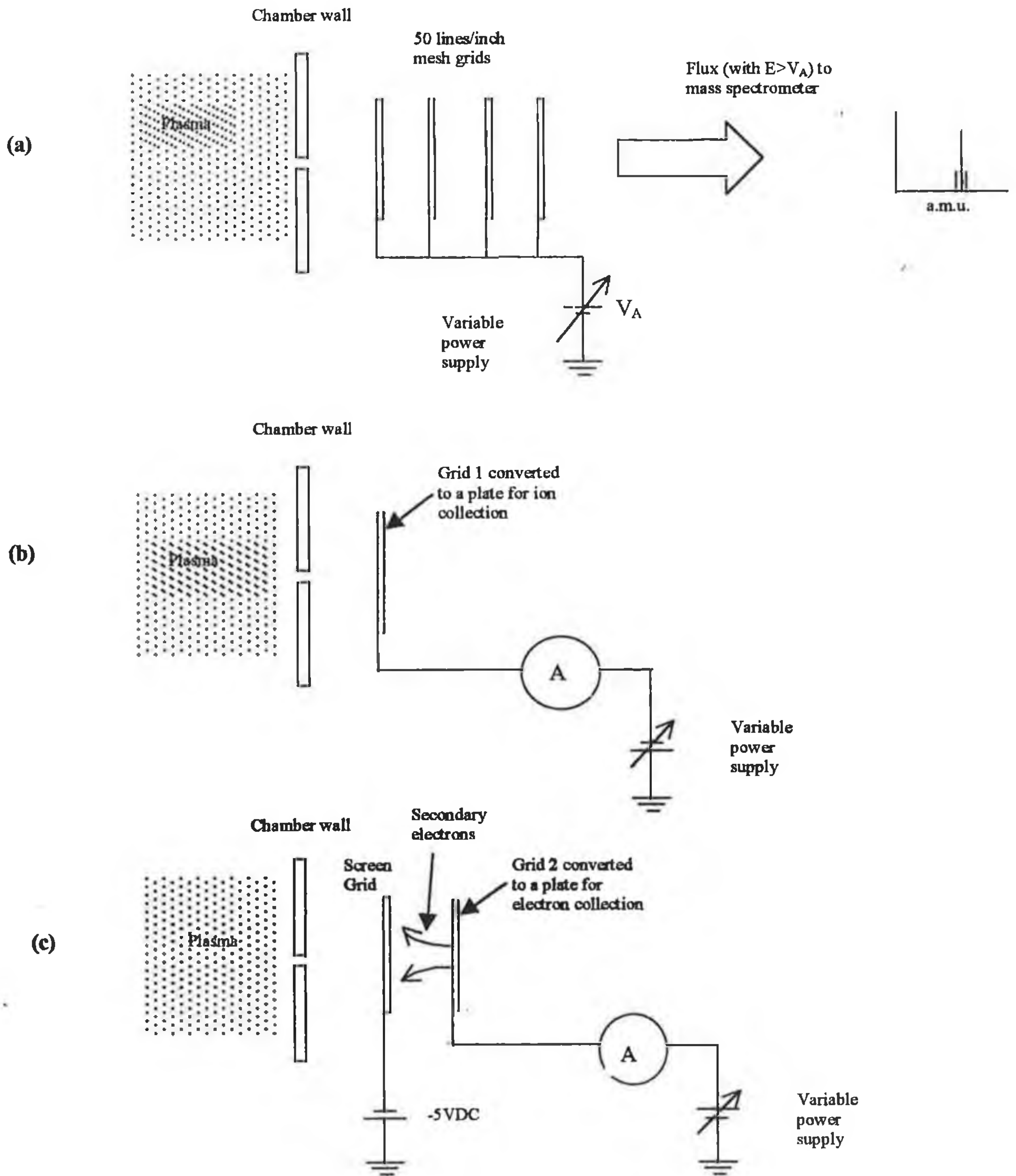

Figure 7.11 Set up of the energy analyser for the collection of different particle data. (a) retarding field analyser repelling ions with $E < V_A$ (b) collection of ion saturation current J_i and (c) collection of electron saturation current J_e.

7.6.3 Ion and Electron Currents

Using configurations (b) and (c) in figure 7.11 the ion and electron currents bombarding per unit area of the substrate during deposition were measured. The aperture used for the data collection was 1.15mm in diameter. The results can then be easily normalised to mm^2 or cm^2. Measurements were taken at both varying solenoid current and process pressure so as they could be related to the grown films. The results in figures 7.12 and 7.13 below illustrate typical values obtained.

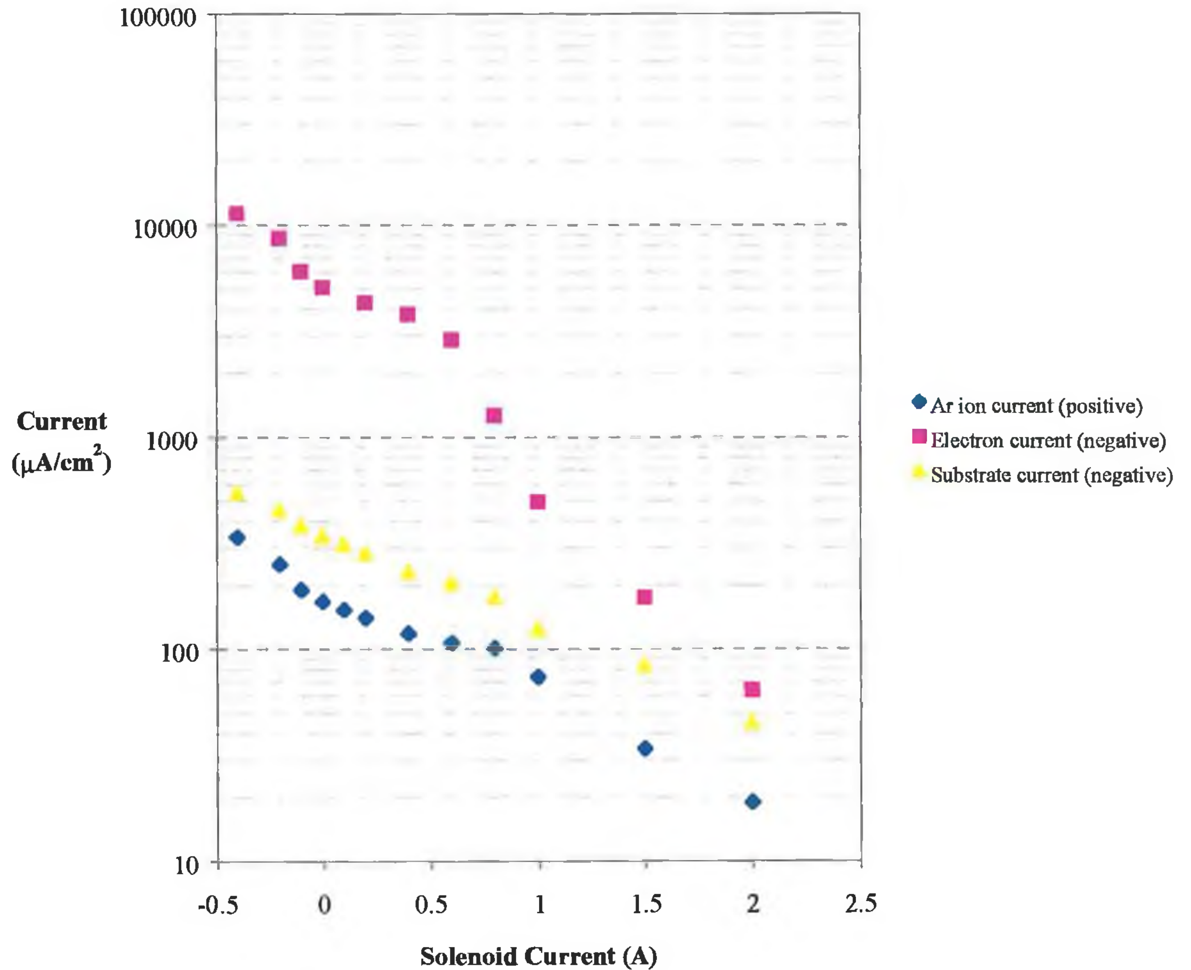

Figure 7.12 Ion and Electron saturation currents measured along with current to a grounded plate as functions of solenoid current. Measurements carried out at a process pressure of 0.4Pa. (Data in Appendix H)

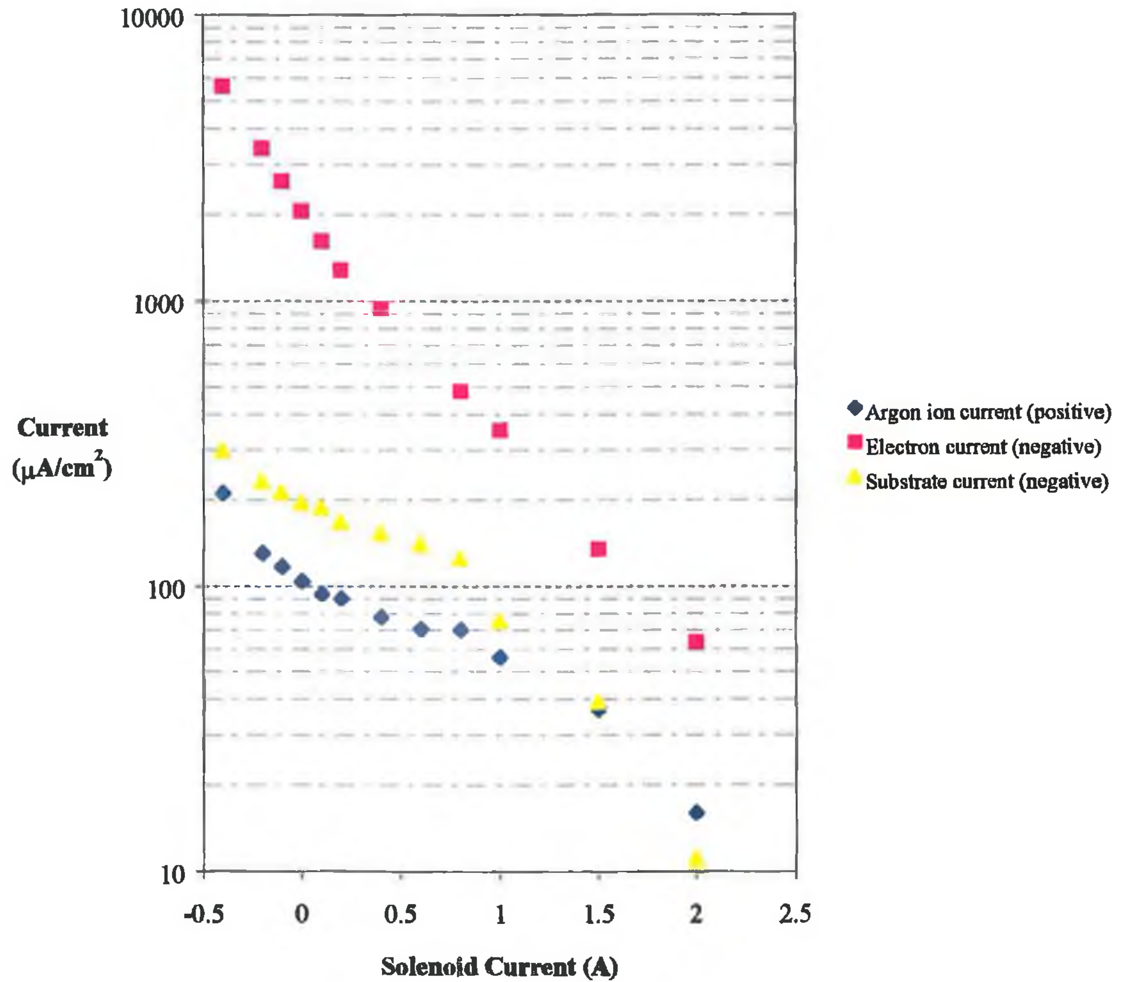

Figure 7.13 Ion and Electron saturation currents measured along with current to a grounded plate as a function of solenoid current, at a process pressure of 1Pa. (Data in Appendix H)

The measured differences are significant. For current measured to a grounded plate, which is what the substrate and growing film would be exposed to, the values change significantly with solenoid current. At 0.4Pa the current to the grounded plate changes by over an order of magnitude for a change in solenoid current from 2A to –0.4A. At the same pressure the changes in electron and ion currents measured by biasing the plate are also significant. Electron current increases by over two orders of magnitude and ion current by nearly 16 times over the same range of solenoid current. These current levels make it clear that significant changes in the film microstructure and deposition conditions are possible. They also show the mechanism for deposition temperature increases with decreasing solenoid current as the power dissipated to the substrate is proportional to the flux of particles bombarding per second.

The currents measured for the 1Pa process show much the same trends, albeit to a lesser extent. This would be expected from the results on deposition temperature and microstructural characteristics reported earlier. Ion and electron currents increase by similar amounts, 13 times for the ion current and approximately two orders of magnitude for the electron current but overall levels are reduced at each setting of solenoid current due to the higher gas pressure and lower operating characteristics of the target. The current measured to the grounded plate increases by a factor of nearly 30 over the solenoid range.

7.6.4 Ion Detection

The ion currents detected can be broken down into energy components by using the energy analyser described in figure 7.11 (a). With the filament switched off ions entering the mass spectrometer can be detected and represented at their atomic mass numbers. Knowing V_A, ion levels detected can be plotted as a function of their energy. This energy is the voltage applied to the grids V_A.

Measurements were carried out at both 0.4Pa and 1Pa of $^{40}Ar^{+}$ ions entering the mass spectrometer for a 500mA discharge. At 0.4Pa, a 1mm diameter aperture was used and at 1Pa a 1.15mm diameter aperture was used due to the lower ion levels present at that pressure. The results were then normalised for 1mm^2 apertures and are reported below in figures 7.14 and 7.15.

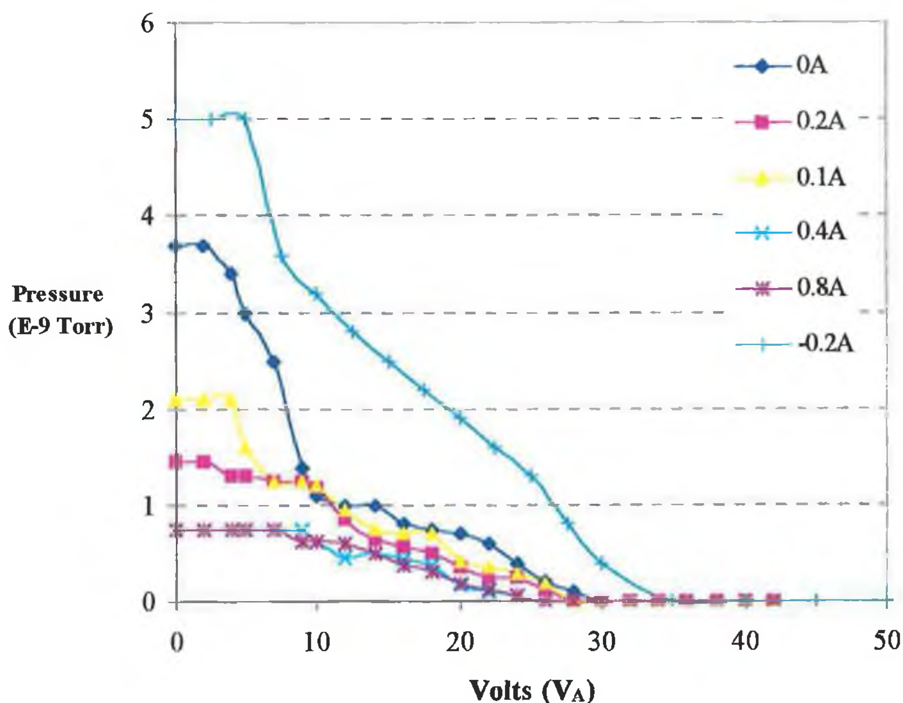

Figure 7.14 **Ion levels detected at 0.4Pa process pressure with varying solenoid current**

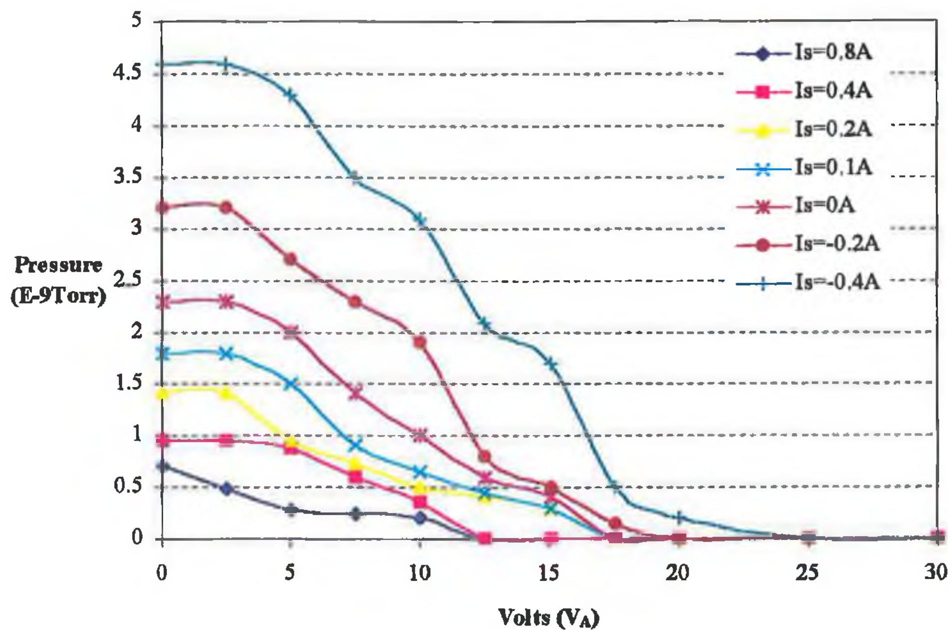

Figure 7.15 Ion levels detected at 1Pa process at varying solenoid current

From initial studies of the plots two distinct observations can be made (a) the flux and energy of ions bombarding the substrate are dependent on process pressure and (b) the flux and energy of ions impinging upon the substrate are dependent upon the solenoid current.

(a) Process Pressure Effects

Reductions in both the energy and flux levels of bombarding ions have been measured as the process pressure increases from 0.4Pa to 1Pa. The main reason for the general decrease in flux and energy of bombarding ions are increased collisions in the plasma body due to higher densities of neutral gas atoms or simply, the mean free path of argon ions is reduced. This decrease has also been measured in the ion current mentioned previously and is also evident from the earlier data gatherer on deposition rate and deposition temperature.

(b) Solenoid Current Effects

As the solenoid current is reduced, increases can be seen in the flux and energy of the bombarding ions at both process pressures. The current in the solenoid is directly responsible for these high-energy tails detected and for the total levels of flux measured.

These high-energy tails must be formed in the plasma body as the target is negatively biased. What causes these tails must be binary collisions with other plasma species. In order to form high-energy ions the flux levels and energies of these other colliding plasma species must also increase with reducing solenoid current. Measurements of electron current confirm the large increases possible for this species and it is a possible candidate for ionization (1) of high-energy neutral Ar atoms rebounding from the target surface after being neutralized. Species such as ^{27}Al atoms and ions also increase in energy as the solenoid current reduces due to an increase in the target operating voltage[4]. This sputter particle energy increase is due to the average energy increase of the argon ions bombarding the target as discussed in target characteristics. Collisions of target atoms in the plasma body with both high-energy neutrals and low energy argon atoms are also possible with ionization taking place through the liberation of an electron from the argon atom ((2),(3)).

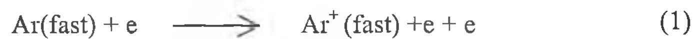

$$\text{Ar(fast)} + e \longrightarrow \text{Ar}^{+}\text{(fast)} + e + e \qquad (1)$$

$$\begin{aligned} \text{Al (fast)} + \text{Ar(fast)} &\longrightarrow \text{Ar}^{+}\text{(fast)} + \text{Al} + e \\ \text{Al (fast)} + \text{Ar(slow)} &\longrightarrow \text{Ar}^{+}\text{(fast)} + \text{Al} + e \end{aligned} \qquad (2)$$

$$\begin{aligned} \text{Al}^{+}\text{(fast)} + \text{Ar(fast)} &\longrightarrow \text{Ar}^{+}\text{(fast)} + \text{Al}^{+} + e \\ \text{Al}^{+}\text{(fast)} + \text{Ar(slow)} &\longrightarrow \text{Ar}^{+}\text{(fast)} + \text{Al}^{+} + e \end{aligned} \qquad (3)$$

The flux of fast neutrals rebounding from the target is approximately the same at each pressure due to the fact that the flux of ions impinging upon the target is the same for a constant discharge current. Their numbers measure[5] approximately 62% of the number of argon ions that make up the discharge current (app. 1.9E18 rebounding fast neutrals, see appendix G). The different levels of ion flux bombarding the substrate then comes about from different probabilities of ionization of these and other neutrals. This probability depends on different levels of electron current escaping from the magnetron discharge at varying solenoid current and, different fluxes of target atoms being ejected from the target, as measured in the deposition rate.

As the process pressure increases the greater the effect on the number of high-energy neutral atoms reaching and exiting the plasma body. This is due to increased collisions with mainly near stationary neutral gas atoms. Ions formed from these binary collisions in (2) and (3) above undergo more collisions due to increases in neutral gas density. The ionization probability of fast neutrals is also reduced due to increased levels of target atom and electron thermalization. This directly effects the ion flux and energy reaching the substrate.

In order to view the flux of ions at energy values, the derivative of figures 7.14 and 7.15 can be plotted in order to get a number distribution of ions as a function of energy. The results typically show a

low energy peak of ions and then a high-energy tail. Figures 7.16 and 7.17 below are the derivatives calculated for each process pressure at different values of solenoid current.

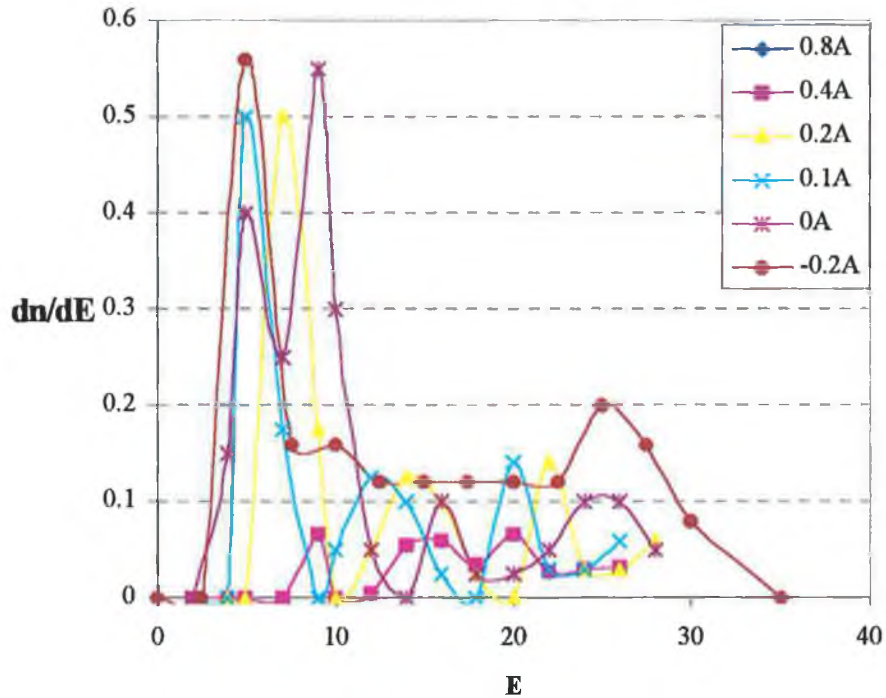

Figure 7.16 **Derivative plot as a function of energy at 0.4Pa process pressure**

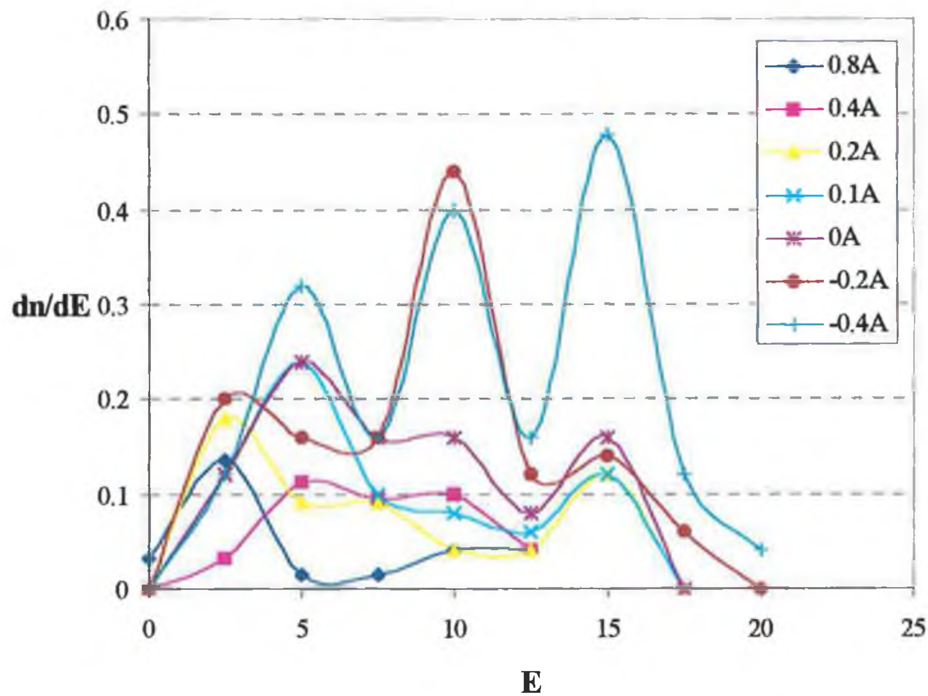

Figure 7.17 **Derivative plot as a function of energy at 1Pa process pressure**

The 0.4Pa plot shows a low energy peak between 4 and 7eV for each value of solenoid current. Detector resolution and stability limit the exact energy location and order of these peaks as it is operating near its lower detection limit (E-10 Torr), noise also becomes a factor. It would be expected that all the low energy peaks should be at the same energy value if not increasing with reducing solenoid current due to the target operating voltage trends previously reported. From the graphs the mean argon ion energy may be calculated. When averaged over the solenoid current range an arithmetic mean particle energy of 12.02eV results for the 0.4Pa process.

The 1Pa plot shows much noisier curves but it does show low energy peaks between 2 and 5eV. Also present are high-energy peaks at low solenoid current levels. The presence of these high-energy fluxes would be unusual and has to be questioned. It could be read from the graphs that this at least points to definite increases in high-energy fluxes at lower solenoid currents but probably not to the extent measured. Again the arithmetic mean argon ion energy has been calculated and averaged over the solenoid current range for the 1Pa process. This has been found at 9.87eV.

In summary it can be said that the levels and energy of argon ion flux bombarding the substrate varies with solenoid current and therefor is controllable. At both pressures low energy peaks are evident in the ion distributions. Reduced levels of high-energy ions are also present which typically have the most effect of modifying the growth characteristics of thin films. It can be seen that the levels of high-energy fluxes are also controllable at different process pressure through the solenoid current setting. This provides an easy way of measuring the effects of high-energy particle bombardment upon growing films.

Using a binary collision model the mean energy of target atoms can been estimated. Due to the large mass differences between Ar^{40} and Al^{27}, argon being over 50% greater, the percentage of energy lost by a target atom for a 180^0 interaction is over 95% per collision. This result causes a much lower energy distribution for Al atoms at the substrate. Mean target atom energies have been calculated at both process pressure and are reported on below.

7.6.5 Power Dissipation

To calculate the power dissipated at the substrate by species impinging upon that substrate a technique developed by Paturaud et al[6] has been employed. The sum of the contributions of each of the species is the total energy transferred to the substrate during deposition, and can be expressed in terms of power dissipated, which can be written as:

$$P_{Total} = P_a + P_i + P_n + P_e + P_r \qquad \text{Eqn. 7.1}$$

where the subscripts *a, i, n, e, r* stand for atom, ion, neutral, electron and radiation respectively.

(a) Atom power

Each condensed atom transfers both its kinetic energy and heat of condensation to the substrate. The power delivered to the substrate is then related to the total atom flux, the mean particle energy and the condensation energy of an aluminium atom. This can be expressed[6] as

$$P_a = J_a(U_o + E_a) \qquad \text{Eqn. 7.2}$$

where J_a is the flux of atoms arriving on the substrate, U_o the condensation energy[12] which is 3.14eV for Al, and E_a the mean energy of the aluminium atom's.

The mean energy of aluminium atoms at the substrate, E_a, can be calculated from the following equation[7]

$$E_a = \sum_{n=0}^{n_{max}} p(1-p^n)E_T R^n \qquad \text{Eqn. 7.3}$$

where p is the probability of an atom passing the target-substrate distance without collision, $p=\exp(-d/\lambda)$, n_{max} the number of collisions required for complete thermalization of a target atom at a given pressure, R is the ratio between the energies of the scattered atom after and before collision. λ is the mean free path between collisions at a given pressure. d the target to substrate distance and E_T the mean energy of the target atoms upon ejection from the target surface.

In order to simplify the calculation it is assumed that a flux of mono-energetic target atoms leave the target surface with energy E_T. It is also assumed that the target atoms obey binary collision laws when they interact with argon atoms. As stated previously, due to the large mass difference between the target and gas atoms, the percentage of energy lost by target atoms is over 95% per 180^0 collision with an argon atom.

Results calculated by the author using an average collision angle of 135^0 or simply a 50% energy reduction upon collision show an energy distribution at the substrate with mean energies of $\langle E_a \rangle$=1.15eV at 0.4Pa and 0.056eV at 1 Pa. It is assumed that n_{max} has a value of 5. E_T has been calculated[8], using sputter simulation software, at 9eV by Daniel's for the author's application.

The flux of target atoms, J_a, has been calculated from the average deposition rates measured. It is assumed that the atoms are ideally stacked. The radius[9] of an aluminium atom is 143 pm.

(b) Ion power

The ion power is a measure of the power dissipated at the substrate due to bombardment by argon ions as discussed in the previous section. This can be expressed[6] in a similar fashion as

$$P_i = J_i(\gamma E_i + V_i) \qquad \text{Eqn. 7.4}$$

where J_i is the flux density of ions which can be calculated from the ion current, E_i the mean ion energy, γ the fraction of ion energy transferred to the substrate (0.7 for argon)[6] and V_i is the ion neutralisation energy (Ar^+ = 15.75 eV)[6].

The values of E_i used will be that of the arithmetic means calculated previously at each process pressure. It is noted that mean energies have been calculated for each value of solenoid current, but detector resolution and accuracy at higher solenoid current values cause unreasonable mean energy distributions due to operation near it's lower detection limit.

(c) Neutral power

The flux of neutrals that bombard the substrate, during sputtering, can also be accounted for. This neutral power comes about from a process termed 'Intrinsic Sputtering'[5], where the growing film is sputtered by high-energy neutral argon atoms. These neutrals are generally argon ions that are neutralised upon bombarding the target and are then reflected back towards the substrate at high energy. The flux of these neutrals reaching the substrate is significant (appendix G), but is dependent on the target voltage[5] and process pressure amongst other parameters. The power dissipated at the substrate by these neutrals can be written[6] as

$$P_n = J_n E_n \gamma_n \qquad \text{Eqn. 7.5}$$

where J_n is the flux density of these neutrals, E_n their mean energy and γ_n the fraction of energy dissipated at the substrate.

(d) Electron power

The power dissipated by electron flux is more complex. Secondary electron emission coefficients are required along with knowledge of the percentage of electrons that escape from the electron trap and the fraction that reach the anode. The power dissipated by the electrons can be written[6] as

$$P_e = R\eta\left(\frac{\gamma}{\gamma+1}\right)I_T e\left(V_c - V_s\right) \qquad \text{Eqn. 7.6}$$

where η is the fraction of electrons that escape from the magnetic field, R the fraction of η that reaches the substrate, γ is the secondary electron emission coefficient for Ar^+-Al interactions, I_T the target current, $e(V_c$-$V_s)$ the energy of electron that arrive at the substrate with V_c being the cathode voltage. This electron energy assumes no collisions in transit from the target to substrate.

Knowing the electron currents measured at the substrate, the author believes that this equation can be reduced significantly. If it can be assumed that all the electron energy is dissipated at the substrate upon collision, then the electron power can be represented as a function of flux density and energy. This can be simply written as

$$P_e = J_e E_e \qquad \text{Eqn. 7.7}$$

where J_e is the electron current density and E_e the mean electron energy impinging upon the substrate.

The mean electron energy has been estimated using Ivanov et al's[7] experimentally obtained results from their unbalanced magnetron system; E_e <0.4Pa> = 5eV and E_e <1Pa> = 3.5eV. The author notes that mean electron energy is possibly a function of solenoid current, but does not have experimental data and believes that the above estimates are reasonable.

(e) Plasma radiation

The plasma radiation contribution is written[6] as

$$P_r = \frac{1}{2}R\lambda_r I_T \qquad \text{Eqn. 7.8}$$

where R is the fraction of energy radiated from the plasma to the substrate, λ_r is the average energy used in the excitation for each sputtering ion created ($Ar^+ \sim 10eV$) [6] and I_T is the target current.

With the results and estimations gathered, the power dissipated at the substrate by target atoms, argon ions and electrons can be calculated. This may be carried out at various solenoid currents for the author's variable balance magnetron process. Figures 7.18 and 7.19 below show the calculations for argon ions, target atoms and electrons detected at the substrate.

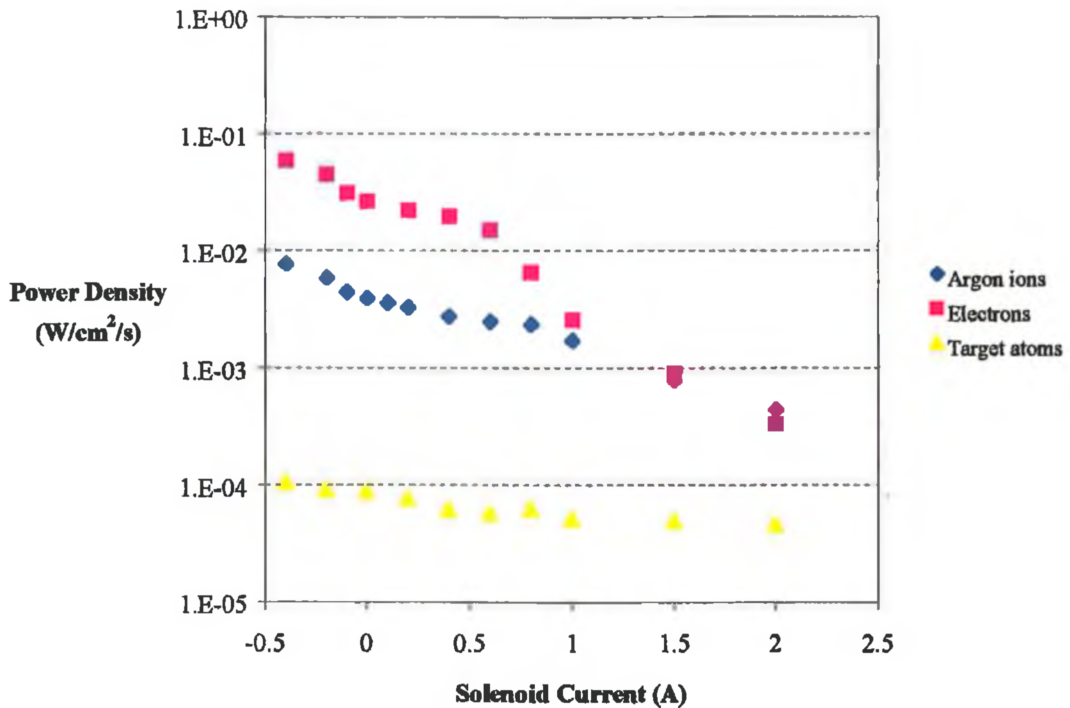

Figure 7.18 **Power density of each species delivered to the substrate at 0.4Pa (Data in appendix H).**

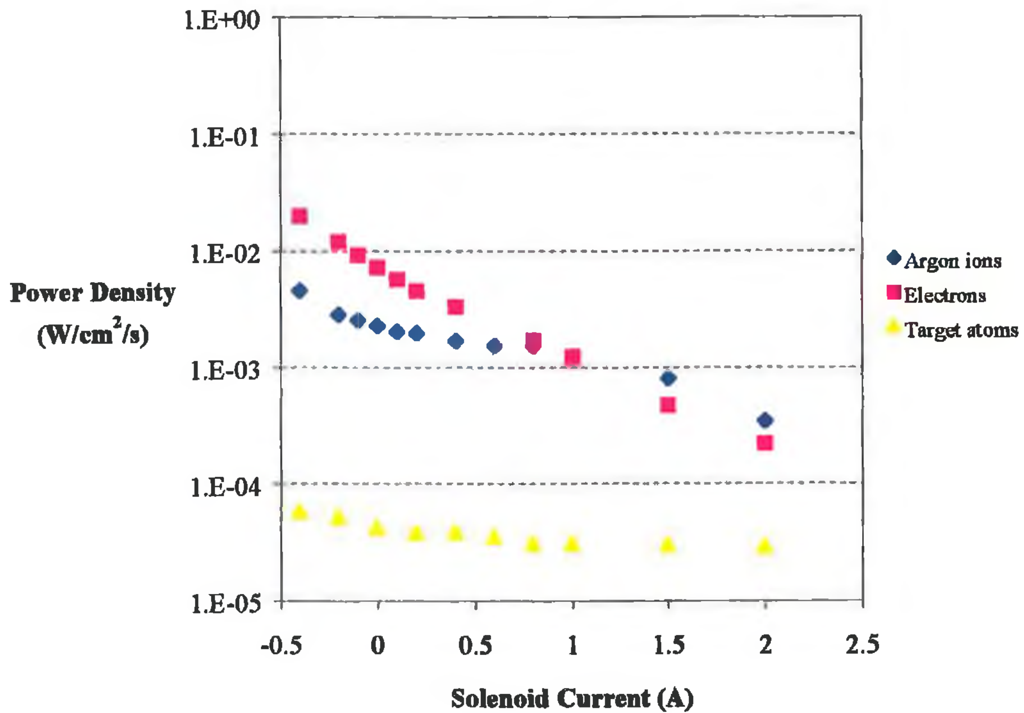

Figure 7.19 Power density of species delivered to the substrate per second at 1Pa. (Data in appendix H).

The sum of the measured species power dissipation at the substrate is represented as a function of solenoid current at each process pressure by figure 7.20 below.

The results shown support previous data on deposition conditions relative to solenoid current settings. No large increases are measured until solenoid reaches below 0.2A. The rate of change of power dissipated at the substrate then increases drastically as a function of solenoid current. From the data in figures 7.18 and 7.19 it can be seen that this is primarily due to secondary electron current escaping from the magnetron discharge and reaching the substrate. This coincides with the magnetic field maps previously reviewed in chapter six.

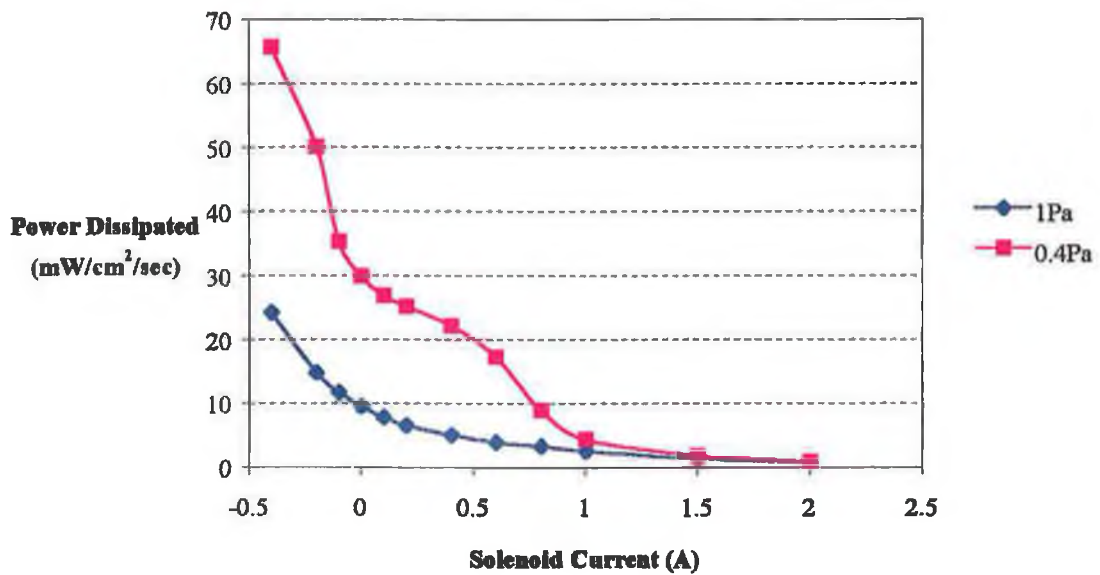

Figure 7.20 Total power dissipated at the substrate by target atoms, argon ions and electrons as a function of solenoid current.

The power dissipated at the substrate by the three species can be plotted against the deposition temperature at each process pressure. The plots reveal characteristics that would be expected, in that the deposition temperature is proportional to the power dissipated by these three species. The plots in figure 7.21 below show the relationships found at each process pressure.

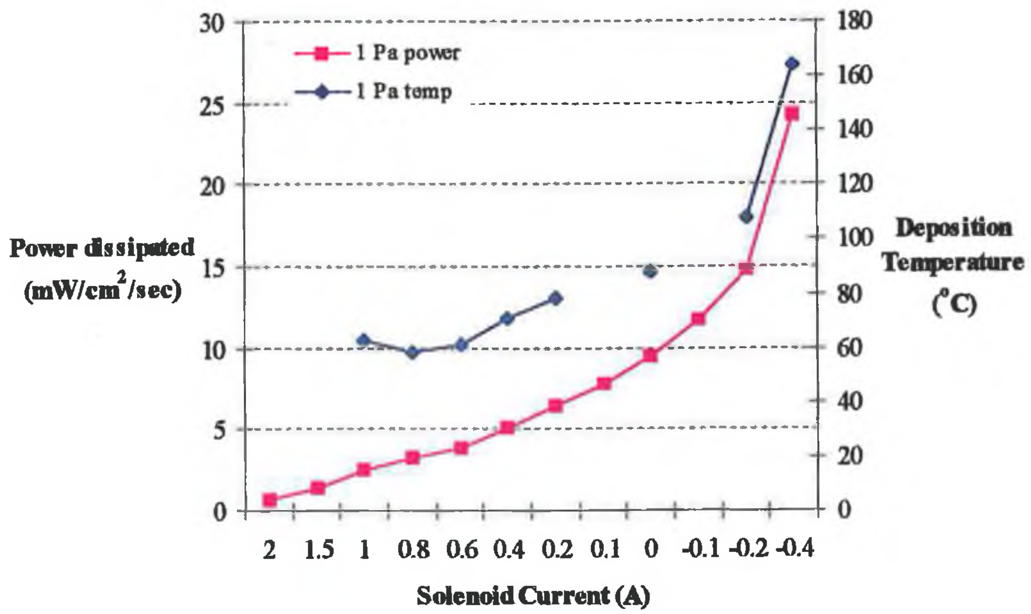

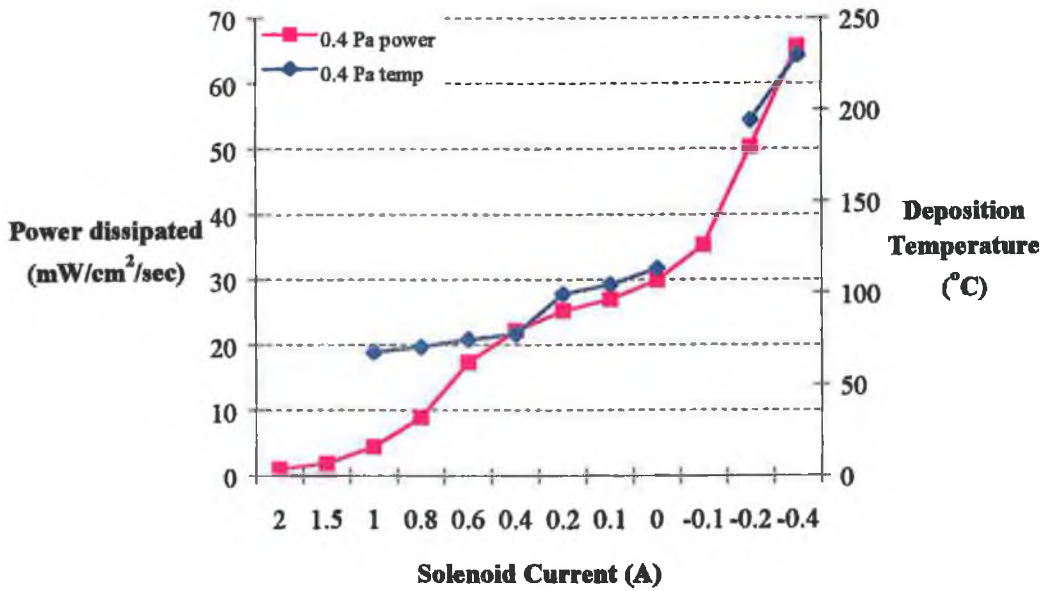

Figure 7.21 Power dissipated by the three species as a function of solenoid current against measured deposition temperature at each process pressure.

Chapter Seven References

[1] B. Chapman, Glow Discharge Processes, Wiley, New York (1980) p82-90.

[2] J. Vossen and W. Kern, Thin Film Processes, Academic Press, New York (1978) Chapter II-2.

[3] B. Chapman, Glow Discharge Processes, Wiley, New York (1980) p380.

[4] K. Wasa and S. Hayakawa, Handbook of Sputter Deposition Technology, Noyes Publications, New Jersey (1992) p49-55.

[5] D.W. Hoffman, J. Vac. Sci. Technol. A 8 (5) (1990).

[6] C. Paturaud, G. Farges, J. Machet, and M. Sainte Catherine, Surf. Coat. Technol. 98 (1998) p1257-1261.

[7] I. Ivanov, P. Kazansky, L. Hultman, I. Petrov, and J. Sundgren, J. Vac. Sci. Technol., A 12(2) (1994).

[8] S. Daniel's, Private Correspondence, July (1999).

[9] www-tech.mit.edu/chemicool/ March (1999).

[10] D.W. Hoffman, T.S. Morley and J-S. Park, J. Vac. Sci. Technol. A 12(4) (1994).

[11] D.A.Lide, Handbook of Chemistry and Physics, CRC Press, New York, 79th Ed., (1998-1999), 6 p100-115.

Chapter Eight
Discussion

8.1 Discussion of Results

All the deposition results obtained from the author's variable balance magnetron sputtering system show a similar characteristic. In general it can said that as the solenoid current reduces, the deposition rate increases due to increases in the target operation voltage. This effect is caused by an increase in the mean energy of bombarding argon ions, which results in an enhanced sputter yield from the target surface as has been reported. This result occurs at both process pressures. The mapping system used in chapter six reveals why the target voltage increases. This is mainly due to a reduction of the furthest reaching field line that intersects the cathode twice. Resulting from this reduction is (a) a decrease in capture volume of secondary electrons emitted from the target and (b) an increased probability of electrons in the race-track region to escape from the discharge. Due to these losses of secondary electrons from magnetron discharge the voltage increases to enhance the secondary electron emission coefficient γ, which is also dependent on the energy of the incident argon ions.

Ultimately, the solenoid current controls the deposition characteristics of the system when the target is operated in constant current mode. With I_S = 0.2A and above only slight changes in operating voltage and power are observed as the field produced is adequate to capture enough secondary electrons to sustain the discharge without a change in voltage. When I_S drops below 0.2A, rapid increases in the voltage, power and deposition rate have been recorded due to a reduction in magnetic flux towards the target surface.

The measurements made of deposition temperature are due to the same effects the solenoid current has on the plasma discharge. The difference being that, the species lost from the discharge that cause increases in target voltage and power can be recorded at the anode as increases in ion and electron currents. These currents dissipate their energy in the form of heat at the anode as has been reported in chapter seven. Once again, the magnitude of change is dependent on the solenoid current setting and therefore is controllable.

Measurements carried out with the analyser chamber show that the flux and energy of argon ions bombarding the substrate is directly dependent on the solenoid current at a particular process pressure.

Lower flux and energy levels of argon ions have been recorded, again generally at I_S >0.2A. With I_S <0.2A, rapid increases have been measured in both J_e and J_i. These results are directly due to the magnetic field configuration of the magnetron.

The argon ion energy distributions bombarding the substrate during film growth are mostly of a low energy thermalised peak at a few electron volts and a high-energy tail extending to ten's of electron volts. Two processes are responsible for the level and energy of ion flux detected:

(1) Increases in electron current (J_e) reaching the anode, which causes ionization in the plasma body of rebounding fast neutral argon atoms from the target.

(2) Level and energy of target atoms colliding with argon atoms in the plasma body.

  (a) As target atom flux increases with reducing solenoid current, argon ion flux increases at the anode due to enhanced probability of collisions.

  (b) As target atom energy increases so to does the energy transferred to the argon atom. (95% energy transfer for 180° binary collision due to large mass difference, $M_{Ar} >> M_{Al}$).

The current densities measured by the author's electrostatic analyser show that by far electrons are the most abundant species reaching the substrate. Levels measured increase rapidly as the solenoid current decreases. From the power dissipation calculations and graphs reported in chapter seven it can be seen that they are most responsible for the temperature increases measured during film deposition. Figure 7.20 of total power dissipated by argon ions, target atoms and electrons, shows a curve similar to that of the deposition temperature data reported earlier. Figure 7.21 compares these two sets of data directly on the same axes and similar slopes can easily be recognised.

When the ratio of electron to ion current (J_e/J_i) is compared at reducing values of solenoid current it is revealed that the figure has a large deviation. Typically starting at 3, when I_s =2A, the electron current increases rapidly until at I_s = -0.4A, the ratio value is near 30 independent of the process pressure. Relating the electron current then to the formation of substrate bombarding argon ions it can be said that J_e has only a minor effect on argon ion generation as the ratio increase is so large. It would then appear that the increases measured in argon ion flux and energy are more dependent on increases in the flux and energy of target atoms and ions ejected from target surface.

When the microstructures of the films grown under different levels of flux bombardment were tested some interesting features were found. Cracks reveal the relative vertical strength of the films after indents made with a Leitz mini-load of 5N. In all it can be said that the strongest and possibly densest film

has the highest flux and energy of bombarding species. These density increases can be caused by the collapsing of voids that can form during growth, as discussed in chapter three. Correspondingly, it has the highest deposition temperature, as would be expected from the levels of ion and electron bombardment detected. The film tested at 0.4Pa with I_s =-0.4A shows no cracking while small cracks are evident when the solenoid current is increased to 0.8A due to temperature and flux decreases during deposition. At 1Pa more profound cracks are evident at both solenoid currents. Reasons for this large increase in crack size are not fully understood. One obvious reason is the increase in gas pressure. This could lead to a larger argon gas percentage trapped within the film microstructure during deposition. Higher concentrations of embedded gas have been shown by Hoffman et al[1] to lead to increases in film stress. This increase in stress could be responsible for the larger, more profound cracks observed on the 1Pa films. The characteristics of these cracks follow deposition temperature and flux levels also, by reducing in size with the solenoid current.

8.2 Limitations

As with most experimental techniques there are limitations to the results obtained. The main causes of error come from two sources, (1) use of a grid analyser and (2) mass spectrometer detector limitations.

(1) Grid Analyser

The sag of potential between the grid wires limits the resolution of a grid analyser. An average particle does not see the voltage that is applied to the grid. The potential it does see is dependent upon the wire spacing. Figure 8.1 shows a cross section of the problem encountered when using a grid analyser.

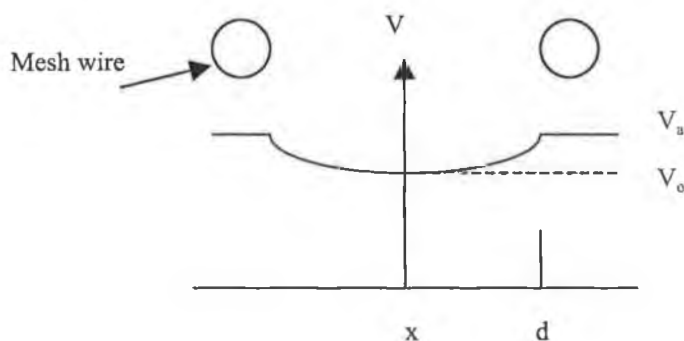

Figure 8.1 Cross sectional view of two grid wires and the voltage distribution between them.

The voltage difference, $\Delta V=V_o-V_a$, at a distance d between the two wires is a function of that distance. It can be expressed[2] as

$$\Delta V = \frac{ned^2}{2\varepsilon_0} \qquad \text{Eqn. 8.1}$$

where n is the space charge density, e the electron charge and d the half distance between the wires.

A second problem of a grid system is that the transmission of species (with $E > V_a$) in the plasma beam is reduced due to collisions with the grid wires. Measuring the current running to ground can approximate for the loss, but it is still valuable information lost.

(2) Mass Spectrometer

The stability and resolution of the quadrupole when operated near its lower detection limit does not allow for highly stable data extraction. Numerous experiments must be carried out in order to find appropriate data averages. Even though the detector is operated near it's lower limit, the flux of particles required for detection is large (app. E13 cm^2/sec) and therefore low-flux, high-energy data is lost. Also lost due to the high flux requirements, are species such as Al^+ that cannot be analysed, as their flux levels are not high enough to be registered at the appropriate atomic mass number.

High-energy species cause an unknown error in the pressure reading displayed, as the instrument is not designed for high-energy ion detection. Ions at higher energy (increased temperature/velocity) will lead to an increase in the pressure reading displayed.

8.3 Future Research

The author believes that the variable balance magnetron sputtering system developed provides an excellent way of measuring substrate effects in-situ, during film growth. Opportunities exist for more experiments to be carried out at (a) different discharge currents, (b) different substrate positions on the anode, (c) increased target-substrate distances, (d) varying pressures and (e) with different sputter gases.

Electron energy distributions can be determined through energy resolved current detection with the author's grid analyser. Minor changes are required in the voltage set up of the analyser and a low secondary electron emission material, such as tantalum, should be used for the collector place.

More complex coatings such as TiN would also be very suitable. As more plasma species are present it would allow for interesting results on substrate bombardment. For this the author believes that a more accurate detector is required with optics that allows for low levels of flux detection at high energies. Such instruments are available but tend to be expensive such as a Balzers PPM421 energy resolved mass spectrometer.

The use of the magnetic field mapping system provides an excellent means for the study of the magnetron plasma with respect to the target characteristics. In effect, software trials can be carried out with solenoid currents prior to running experiments. Magnetrons of Windows and Savvides type 1 may also be investigated by using software simulations.

Chapter Eight References

[1] D.W. Hoffman, J. Park and T. Morley, J. Vac. Sci. Technol., A 12(4) (1994).

[2] M. Sugawara, B. Bergevin, B. Stansfield, and B. Gregory, INRS, Energie Rapport Interne, Number 033 (1970).

Appendices

Appendix A	Cryogenic Pumps
Appendix B	Magnetron Driver
Appendix C	Baratron® Specifications
Appendix D	Excel Coefficient Finder
Appendix E	Vector Plot Software
Appendix F	Field Mapping Software
Appendix G	Neutral Particle Reflection Calculation
Appendix H	Ion and Electron Current & Power Data

Appendix A
Cryogenic Pumps

Cryogenic pumps or cryopumps as they are commonly called are condensation type pumps. Gas atoms and molecules are captured or frozen by cold surfaces whose temperature is lower at the existing pressure than their vapor pressure. Most material can exist in several physical states: solid, liquid, and gas. Under changing conditions of temperature and pressure they will change states. Water and metals go from a solid at low temperature to a liquid and then to a vapour (boiling) as the temperature increases. Some like carbon dioxide have only two states, a solid and a vapour (dry ice and gas).

Cooling to the low temperatures required is carried out by means of a refrigerated compressor using helium. The final cooling occurs in a motor driven cold head. There are three differential pumping areas with the first being the upper array which is at 77° Kelvin ($-196^{o}C$). Water, carbon dioxide and organic material are pumped by this array which is also an optical baffle so that the likelihood of the atoms or molecules of those materials reaching the lower, colder array is very small.

The lower array is at $15\ ^{o}$ Kelvin ($-258^{o}C$) and pumps the remainder of the gases with the exception of very light gases. The bottom of the lower array is coated with an absorber material, having a very large effective surface area, which is usually charcoal. Hydrogen and helium are not condensed at $15\ ^{o}$ K but are absorbed onto the surfaces and buried by other gases condensing on top. These stages are schematically represented in figure A1 below.

Periodically, the condensed gases must be removed by a process called regeneration. The gate valve is closed and an inert purge gas, usually warm nitrogen or argon, is passed through the pump. A pressure relief valve opens when the pressure reached a few pounds above atmosphere. As the frozen gases warm up, they are carried by the purge gas out through the relief valve. After the gases are removed the cryo-pump is roughed down with a mechanical pump and the compressor is restarted. Typical regeneration times are about three hours.

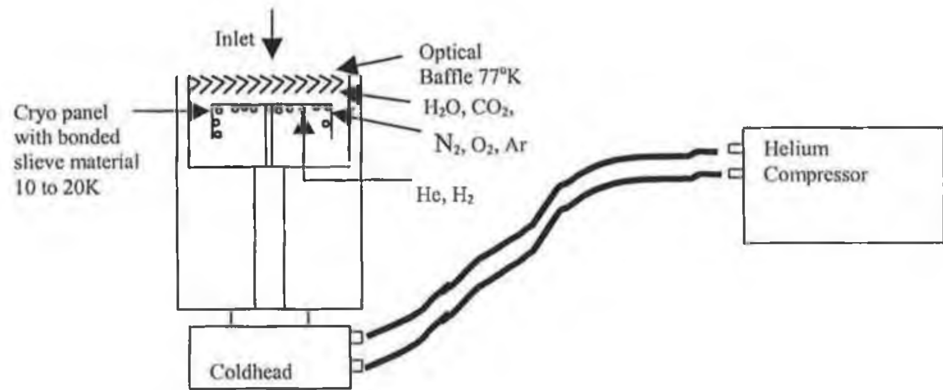

Figure A.1 Cryogenic pump schematic

Appendix B

Advanced Energy 5kW Magnetron Driver

The DC magnetron driver is a convenient and efficient advanced high frequency switch mode power supply. They are

- light and compact
- are highly efficient (low heat emission)
- provide excellent regulation and stability
- have a highly reliable solid state design
- are modular
- store very little energy in the output filter.

These drivers exhibit superior output response time, low output ripple voltage, and are a considerable space saving. The internal microprocessor provides ease of use, and the modular design allows easy maintenance when required.

The MDX can be used as a power, current or a voltage source depending on the method of output regulation selected. Since the setpoints are stored in non-volatile memory, they can be used in recovering from power input interruptions and to ensure repeatability from run to run.

The MDX has two digital displays on the front panel along with LED indicators. Power, voltage, current, ramp time, run time, target selection, target life and interlock status are examples of the parameters that can be displayed. The MDX is also built with complete internal protection for output over voltage, over current and over power conditions.

Special ARC-OUT™ circuitry provides multilevel suppression and quenching of different types of arcs. An added advantage is that ARC-OUT reduces the target burn in time and material loss. This feature also prevents energy from being dumped into hot spots by sensing a drop in impedance and immediately shutting the power off. Start up after an arc is controlled so that the hot spots cool before power is reapplied, thus preventing repeated arcing.

Physical Specifications

Input Voltages	380VAC or 415VAC RMS, 50/60 Hz, three phase. Maximum ground leakage current less than 3.5mA

Output Power 0-5000W

Output voltage range 0-1000V at 6.25A

Output display Accuracy Within 2% of actual output level or 0.2% of maximum rated output level, which ever is greater.

Target Accumulator Target life is displayed a 1-kWh increments, the counter is undated every 4.7ms.

Methods of control Full or restricted, local or remote, programmed or manual operation.

Output connector Molded output connector

Output cable RG-8U coaxial cable and/or discrete cables

Size 7"(H) x 19"(W) x 25"(D)

Weigth 65lb

Operating temperature Min O° C , max 40^0 C.

Magnetron Schematic

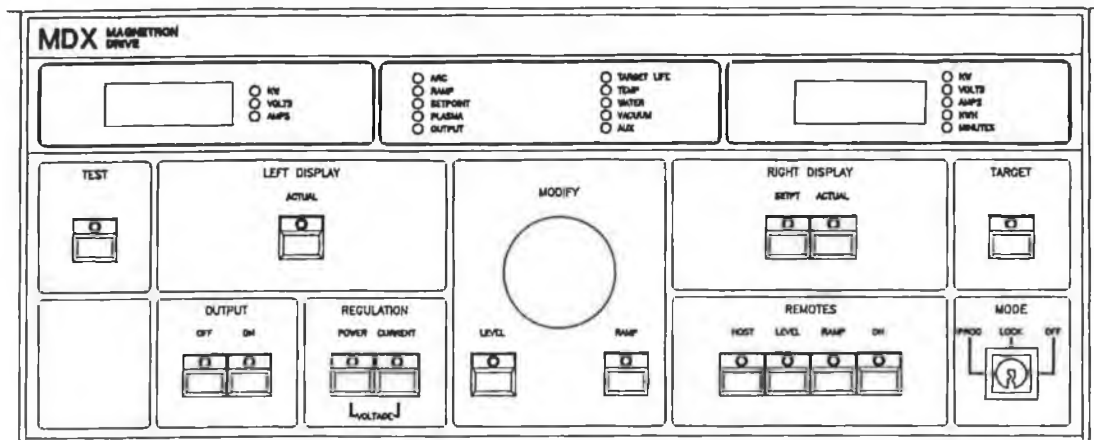

Appendix C

Baratron® Specifications

(Note: Reference to Appendix A in text applies to specification literature of manufacturer)

Dimensions

Note All dimensions are listed in inches with millimeters referenced in parentheses.

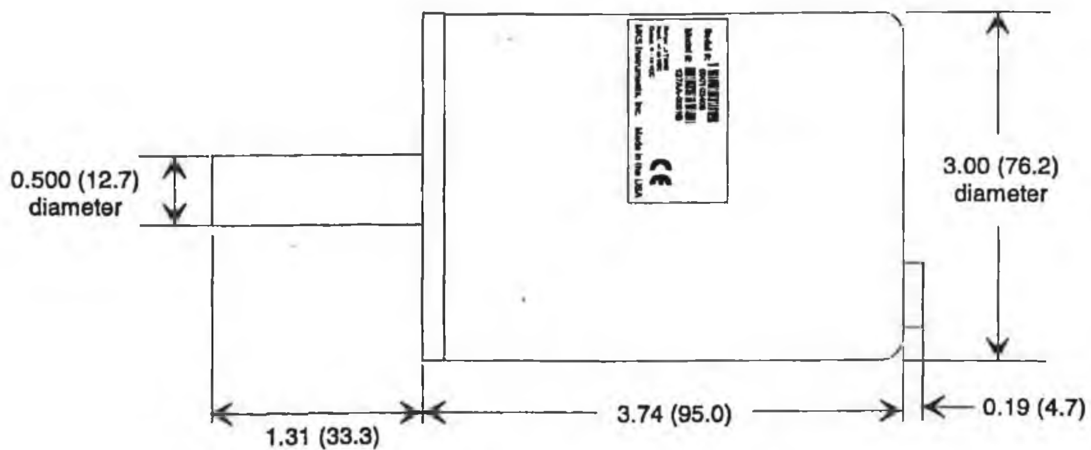

Figure 3: Dimensions of a Low Range Type 127/128 Transducer

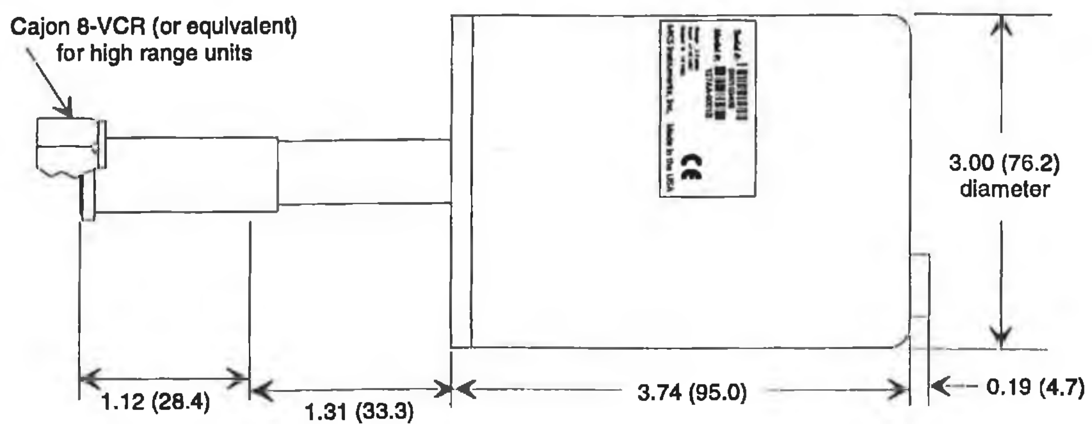

Figure 4: Dimensions of a High Range Type 127/128 Transducer

Appendix A: Product Specifications

Type 127 Performance Specifications

Accuracy	
0.1 Torr	0.25% of Reading ± temperature coefficient
1 to 1000 Torr	0.15% of Reading ± temperature coefficient
>1000 to 25K Torr	0.12% of Reading ± temperature coefficient
CE Compliance	
Electromagnetic Compatibility[1]	EMC Directive 89/336/EEC
Resolution	0.01% of Full Scale
Response Time	<16 milliseconds
Temperature Coefficient	
Zero	
0.1 Torr	0.015% F.S./°C
1 Torr to 25K Torr	0.005% F.S./°C (over 15 to 40 °C)
Span	0.02% Reading/°C (over 15 to 40 °C)

[1] An overall metal braided shielded cable, properly grounded at both ends, is required during use.

Type 127 Physical Specifications

Fittings	½ inch diameter tubulation, Cajon 8-VCR, Cajon 8-VCO, NW-16-KF (not available for 10K through 25K Torr units), Mini-CF, rotatable
Full Scale Pressure Range (in Torr)	0.1, 1, 2, 10, 100, 1000, 5K, 10K, 15K, 20K, 25K
Input Power	
at startup	±15 VDC ±5%, 250 mA
after 1 hour at 30 °C	150 mA
Internal Volume	7.0 cc
Material Exposed to Gas	Inconel (plus pressure fitting materials, if applicable)
Output Signal	0 to 10 VDC into 10K ohm load or greater
Overpressure	
1 Torr to 25K Torr	35 psia
0.1 Torr	20 psia or 120% F.S., whichever is greater
Temperature	
ambient operating	15 to 40 °C
sensor operating	45 °C
Weight	1 kg (2.25 lbs.)

Due to continuing research and development activities, these product specifications are subject to change without notice.

Appendix D

Excel Coefficient Finder

D.1 Introduction

Microsoft Excel was used along with add-ins such as Solver and Ansys Tool-Pak to find the coefficients *a(i)* for a particular field configuration. With the measurements (B_r, B_z) made in discrete points with a Bell gauss meter and the radial and axial co-ordinates of those measurements (r,z) a spreadsheet can be made up like the one in section D.3. Other constants are required for entry such as the first five roots of the Bessel function $J_0(x) = 0$ which are written as l[1-5] and r_0 which is an important constant as it defines the base with of the magnetic field as one unit. This constant r_0 was set to 70.

From this spreadsheet, with the appropriate cells programmed with equations 4A and 4B the solver can be set to calculate the coefficients in the target cells (a[1-5]). A report is then delivered by the solver program giving values for the target cells. These coefficient values can then be used to calculate B_r and B_z flux values at any point (r,z)

The reports are listed in D.2 for the four magnetic field geometry's mapped.

The Excel spreadsheet used by the author is on the diskette attached.

D.2 Solver Reports

Below are the solver reports listed in order of decreasing solenoid current giving the coefficient a(i) values that are then used to plot the field line trajectories.

D.2.1 Is=0.8A

Microsoft Excel 8.0 Sensitivity Report
Worksheet: [IS0.8.xls]MV_2_0
Report Created: 06/05/99 16:47:15
Solenoid Current Is=0.8A

Adjustable Cells

Cell	Name	Final Value	Reduced Gradient
H6	a_0	247.7209007	0
I6	a_1	-1021.815754	0
J6	a_2	-765.0241275	0
K6	a_3	1456.069926	0
L6	a_4	-1045.368953	0

D.2.2 Is=0.4A

Microsoft Excel 8.0 Sensitivity Report
Worksheet: [IS0.4.xls]MV_2_0
Report Created: 05/05/99 20:38:58
Solenoid Current = 0.4A

Adjustable Cells

Cell	Name	Final Value	Reduced Gradient
H6	a_0	260.3940364	0
I6	a_1	-905.1332917	0
J6	a_2	-729.9365552	0
K6	a_3	1317.742773	0
L6	a_4	-858.1871278	0

D.2.3 Is=0A

Microsoft Excel 8.0 Sensitivity Report
Worksheet: [IS0.xls]MV_2_0
Report Created: 29/04/99 18:40:08
Solenoid Current = 0A

Adjustable Cells

Cell	Name	Final Value	Reduced Gradient
H6	a_0	278.5418055	0
I6	a_1	-954.5759136	0
J6	a_2	-636.6234972	0
K6	a_3	1550.704461	0
L6	a_4	-969.0819222	0

D.2.4 Is=-0.4A

Microsoft Excel 8.0 Sensitivity Report
Worksheet: [ISneg0.4.xls]MV_2_0
Report Created: 07/05/99 14:08:34
Solenoid Current = -0.4A

Adjustable Cells

Cell	Name	Final Value	Reduced Gradient
H6	a_0	328.4174922	0
I6	a_1	-853.3175325	0
J6	a_2	-580.6894485	0
K6	a_3	1712.126402	0
L6	a_4	-1079.305308	0

D.3 Refer to diskette

Appendix E

Vector Plot Software

E.1 Introduction

The following code was used to plot the vector arrows, which approximate the magnetic field shape at Is=0.8A. The values of B_r and B_z are equal to 1+log|B| and are calculated before entry to the arrays. Matlab version 1.5 was used to run the software.

For different solenoid currents new values of r, z, B_r, and B_z must be entered in the appropriate arrays.

E.2 Software Code

```
% Vector plot for Is =0.8amps
%
% r: r values
% z: z values
% Br: br
% Bz: bz
% x: x values

%Define constants
alpha=.3;
beta=.3;
sym='b';
clf;

%Define measurement and plotting points

r=[0,3,5,8,10,15,18,20,25,28,30,33,35,40,45,50,60,70,0,0,0,0,0,0,0,0,0,
0,0,10,15,20,25,30,35,40,50,60,70,10,15,20,25,30,35,40,50,60,70,38,38,3
8,38,38,38,38,38,38];

z=[4,4,4,4,4,4,4,4,4,4,4,4,4,4,4,4,4,4,1,3,5,10,15,20,25,30,40,50,60,20
,20,20,20,20,20,20,20,20,20,50,50,50,50,50,50,50,50,50,50,10,15,20,25,3
0,40,50,60,70];

%Relative Bz and Bz values
 Br=[-1.83 ,-2.00 ,-2.25 ,-2.45 ,-2.51 ,-2.54 ,-2.55 ,-2.55 ,-2.57 ,-
2.61 ,-2.70 ,-2.75 ,-2.74 ,-2.06 ,2.64 ,2.67 ,2.33
,1.99,0.00,0,0,0,0,0,0,0,0,0,0,-1.85,-1.92,-2.02,-1.98,-1.87,-
1.61,1.85,1.81,1.92,1.85,-0.74,-0.64,-
0.61,0.38,0.69,0.81,1.02,1.28,1.39,1.37,-2.03,-1.71,-
1.49,1.04,0.70,0.70,0.85,0.95,0.95];

 Bz=[-2.86,-2.84,-2.83,-2.78,-2.64,-2.43,-2.39,-2.25,-
1.85,0.78,1.58,2.42,2.70,2.92,2.86,2.34,-0.78,-1.56,-2.99,-2.88,-2.78,-
2.61,-2.37,-2.13,-1.83,-1.57,0.78,1.26,1.30,-2.00,-
```

```
1.73,1.28,1.38,1.93,2.08,2.16,2.10,1.79,1.40,1.26,1.34,1.41,1.48,1.52,1
.56,1.57,1.56,1.43,1.30,2.51,2.26,2.13,1.98,1.88,1.71,1.57,1.45,1.34];

% Make velocity vectors
r = r(:).'; z = z(:).';
Br= Br(:).'; Bz = Bz(:).';
uu = [r;r+Br;NaN*ones(size(Br))];
vv = [z;z+Bz;NaN*ones(size(Br))];

h = plot(uu(:),vv(:),sym);

% Make arrow heads and plot them
hr = [r+Br-alpha*(Br+beta*(Bz+eps));r+Br; ...
      r+Br-alpha*(Br-beta*(Bz+eps));NaN*ones(size(Br))];
hz = [z+Bz-alpha*(Bz-beta*(Br+eps));z+Bz; ...
      z+Bz-alpha*(Bz+beta*(Br+eps));NaN*ones(size(Bz))];
hold on
h = [h;plot(hr(:),hz(:),sym)];

%Define axes
axis([0,80,0,80]);

zoom on
```

Appendix F

Field Line Plotting Software

F.1 Introduction

The following software program was developed by the author to plot magnetic field lines shown in chapter six. Constants used in the program are a(1-5) calculated from Excel, l(1-5) which are the first five roots of the Bessel function $J_0(x)=0$, r_0 which defines the base width of the magnetic field and the step size 'step' which is best found through trial and error. To enhance the resolution especially at low z values where B_r and B_z values are higher the step size is altered when z(i) reaches 30. The variables in the program are (r,z). The couple (r_1,z_1) are inputted by the user prior to running the program. From these parameters the program calculates the B_r and B_z values at that point and creates a vector in the field direction. A second point (r_2,z_2) is then calculated a distance 'step' along the vector. From here the program repeats and plots each r,z pair up to (r_i,z_i). The field line is then drawn as a tangent to the field vectors in the direction of the magnetic field **B**.

F.2 Program Code

```
%Program for Is=0.8 Amps
%Measurements carried out at
%    r=[36,37,38,39,40,41,42,43,44,39.5,39.25,39.35]
%    x=[62,90,142,325,500,500,500,500,500,700,505,694]

%Set Axes
axis([0,80,-20,70]);

%Set constants ai[1-5] calculated in Excel
a(1) =247.7209007; a(2)= -1021.815754;a(3)=-765.0241275; a(4)=1456.069921; a(5)=-1045.368953;

%Set constants li[1-5]. roots of Bessel function Jo(x)=0
l(1)= 2.404825558; l(2)=5.52007811; l(3)=8.653727913; l(4)=11.79153444; l(5)=14.93091771;


%Define dimensions
ro=70 ;
x=694;

%Initiate Arrays for r and z with zeros
r=zeros(1,x);
z=zeros(1,x);

%Initiate Arrays for vectors components.
Br=ones(1,1000);
Bz=ones(1,1000);
```

```
%Initiate Arrays for vectors trajectories.
traj_r=ones(1,1000);
traj_z=ones(1,1000);
%res_vec=zeros(1,1000);

%Set step size
step=0.007;

%Define (r1,z1) co-ordinates
z(1)=1;
r(1)=39.35;

%Define Array Dimensions
Dz_dt=zeros(1,x);
Dr_dt=zeros(1,x);

Br_sum=zeros(1,x);
Bz_sum=zeros(1,x);

for i=1:x

%Calculate the first five coefficients at (r1,z1), F(r1,z1)
for n=1:5
Br(n)=a(n)*Besselj(1,(l(n)*r(i))/ro)*exp(-(l(n)*z(i))/ro);%Evaluate Br(n)
Dr_dt(i)=Br(n)+ Dr_dt(i);
Bz(n)=a(n)*Besselj(0,(l(n)*r(i))/ro)*exp(-(l(n)*z(i))/ro);%Evaluate Bz(n)
Dz_dt(i)=Bz(n)+ Dz_dt(i);
end


traj_r(i)=Dr_dt(i);
traj_z(i)=Dz_dt(i);

%Plot calculated r and z values only
plot(r(i),z(i),'r-');


res_vect(i)=sqrt(traj_r(i)^2 + traj_z(i)^2);

%Choose step size depending on z(i) value to enhance resolution
if z(i) < 30
   step = 0.0007;
else
  step=0.007;end

     r(i+1)=r(i)+(step*Dr_dt(i));   %step  r  forward or back



%Find z(n+1)
z(i+1)=z(i)+(step*Dz_dt(i));

  hold on;
   axis([0,80,-20,70]);
end
```

```
%Plot points as a continuous line
plot(r,z,'r-');
```

Appendix G

Neutral Particle Reflection

The flux of neutrals reflecting from the target surface upon argon ion neutralisation has been calculated using formulae developed by Hoffman et al[10]. The calculation is carried out as follows.

The atomic mass parameter m is important as it relates the sputter gas atomic mass to the target material atomic mass. It is written[10] as

$$m = \frac{M_{Al} - M_{Ar}}{M_{Al} + M_{Ar}}$$

For argon on aluminium the value of m equates to –0.194.

The formula for the ratio of back-scattered neutrals to bombarding ions from the target is written[10] as

$$\log(N_N / N_O) = (-2.177 + 2.658m - 1.014m^2) + (-0.346 + 0.489m - 0.264m^2)\log E_r$$

where N_o is the number of incident ions, N_N the number of reflected neutrals, and E_r is referred to as the energy reduction coefficient and can be written[10] as

$$Er = \frac{16.25(1+m)}{Z_{Al}Z_{Ar}\left(\sqrt{Z_{Al}} + \sqrt{Z_{Ar}}\right)^{2/3}}(E_o / 1000)$$

where Z is the atomic number of the species, E_o the energy of the incident argon ions.
For the calculation E_o is assumed to be 500eV.

E_r equates to 7E-03.

Equating the reflection ratio,

$$\log(N_N / N_O) = (-2.177 + 2.658(-0.194) - 1.014(-0.194)^2) + \\ (-0.346 + 0.489(-0.194) - 0.264(-0.194)^2)\log 7E - 03$$

$$\log(N_N / N_O) = (-2.177 + 2.658m - 1.014m^2) + (-0.346 + 0.489m - 0.264m^2)\log E_r$$

$$\log(N_N / N_O) = (-2.733) + (-0.4564)(-4.96)$$

$$\log(N_N / N_O) = -0.468$$

There for the ratio of reflected neutrals to incident ions is

$$N_N / N_O = 0.626$$

This gives a reflection of 62% of incident ions from the target surface.

For a 500mA discharge, there are 3.12E18 ions striking the target per sec. This means that 1.9E18 are reflected back towards the substrate as neutral atoms.

Appendix H

Ion and Electron Current & Power Data

Solenoid Current (A)	Ion Current (μA/cm^2)	Electron Current (mA/cm^2)	Substrate Current (μA/cm^2)
2	19	-0.064	-45
1.5	34	-0.175	-84
1	74	-0.495	-124
0.8	101	-1.26	-175
0.4	118	-2.87	-230
0.2	140	-3.79	-282
0.1	153	-4.28	-310
0	168	-5.07	-340
-0.1	190	-6.03	-380
-0.2	252	-8.67	-453
-0.4	338	-10.83	-544

Table 1 Ion and Electron saturation currents at 0.4Pa.

Solenoid Current (A)	Ion Current (μA/cm^2)	Electron Current (mA/cm^2)	Substrate Current (μA/cm^2)
2	16	-0.063	-11
1.5	37	-0.134	-39
1	56	-0.35	-75
0.8	70	-0.48	-124
0.4	77.5	-0.935	-152
0.2	90.2	-1.275	-167
0.1	93.5	-1.61	-187
0	103.5	-2.05	-195
-0.1	116.5	-2.61	-211
-0.2	130	-3.39	-231
-0.4	211	-5.6	-298

Table 2 Ion and Electron saturation currents at 1Pa.